NUMERICAL INVESTIGATION OF DEFORMATIONS OF MATERIALS WITH EMBEDDED SYSTEMS AND HUMAN FOOT STRUCTURE UNDER DIFFERENT LOADING CONDITIONS

SHUDONG LI

A thesis submitted in partial fulfilment of the requirements of Liverpool John Moores University for the degree of Doctor of Philosophy

March 2018

ACKNOWLDGEMENTS

ABSTRACT

In this work, parametric FE (Finite Element) modelling has been developed and used to study the deformation of soft materials with different embedded systems under indentation and more complex conditions. The deformation of a soft material with an embedded stiffer layer under cylindrical flat indenter was investigated through FE modelling. A practical approach in modelling embedded system is evaluated and presented. The FE results are correlated with an analytical solution for homogenous materials and results from a mathematical approach for embedded systems in a half space. The influence of auxeticity on the indentation stiffness ratio and the de-formation of the embedded system under different conditions (indenter size, thickness and embedment depth of the embedded layer) was established and key mechanisms of the Poisson's ratio effect are highlighted. The results show that the auxeticity of the matrix has a direct influence on the indentation stiffness of the system with an embedded layer. The enhancement of indentation resistance due to embedment increases, as the matrix Poisson's ratio is decreased to zero and to negative values. The indentation stiffness could be increased by over 30% with a thin inextensible shell on top of a negative Poisson's ratio matrix. The deformation of the embedded layer is found to be significantly influenced by the auxeticity of the matrix. Selected case studies show that the modelling approach developed is effective in simulating piezoelectrical sensors, and force sensitive resistor, as well as investigating the deformation and embedded auxetic meshes.

A full scale parametric FE foot model is developed to simulate the deformation of the human foot under different conditions including soles with embedded shells and negative Poisson's ratio. The models used a full bone structure and effective embedded structure method to increase the modelling efficiency. A hexahedral dominated meshing scheme was applied on the surface of the foot bones and skin. An explicit solver (Abaqus/Explicit) was used to simulate the transient landing process. Navicular drop tests have been performed and the displacement of the Navicular bone is measured using a 3D image analysing system. The experimental results show a good agreement with the numerical models and published data. The detailed deformation of the Navicular bone and factors affecting the Navicular bone displacement and measurement is discussed. The stress level and rate of stress increase in the Metatarsals and the injury risk in the foot between forefoot strike (FS) and rearfoot (RS) is evaluated and discussed. A detailed full parametric FE foot model is developed and validated. The deformation and internal energy of the foot and stresses in the metatarsals are comparatively investigated. The results for forefoot strike tests showed an overall higher

average stress level in the metatarsals during the entire landing cycle than that for rearfoot strike. The increased rate of the metatarsal stress from the 0.5 body weight (BW) to 2 BW load point is 30.76% for forefoot strike and 21.39% for rearfoot strike. The maximum rate of stress increase among the five metatarsals is observed on the 1st metatarsal in both landing modes. The results indicate that high stress level during forefoot landing phase may increase potential of metatarsal injuries. The FE was used to evaluate the effect of embedded shell and auxetic materials on the foot-shoe sole interaction influencing both the contact area and the pressure. The work suggests that application of the auxetic matrix with embedded shell can reinforce the indentation resistance without changing the elastic modulus of the material which can optimise the wearing experience as well as providing enough support for wearers. . Potential approaches of using auxetic structures and randomly distributed 2D inclusion embedded in a soft matrix for footwear application is discussed. The design and modelling of foot prosthetic, which resembles the human foot structure with a rigid structure embedded in soft matrix is also presented and discussed.

Contents

List of Figures

Chapter 4

Chapter 5

List of Symbols

Δ: Displacement of indenter

$\overline{I}_1$, $\overline{I}_2$ and D_l The first and second deviatoric strain invariants

$\bar{\lambda}_i$: are the deviatoric principle stretches

A_0: Original specimen cross-sectional area

L_0: Original specimen Length

ε_e: Engineering strain

σ_e: Engineering stress

σ_y: Yield stress

C_{10}, C_{01}: Temperature-dependent material parameters in Mooney Rivlin model

J^{el}: the elastic volume ratio

α_i: temperature-dependent material parameters

α_n: Constants in Ogden model

λ_i: the principal stretches

μ_i : temperature-dependent material parameters

μ_n: Constants in Ogden model

β_i: degree of compressibility

b: Radius of indenter

D_i: temperature-dependent material parameters

E: Young's Modulus

E_m: Young's modulus of Matrix

E_s: Young's modulus of embedded shell

h: depth of the embedment from the top surface

J: Total volume ratio

K: Strength coefficient

K_0: initial bulk modulus

n: Strain hardening exponent

N: the order of the polynomial

P: indentation force for a material with embedment

P_0: Indentation Load of material without shell

U: strain energy per unit of reference volume

v: Poisson's ratio

v_m: Poisson's ratio of matrix

v_s: Poisson's ratio of shell

W: Strain energy

δ: Material deformation

ε_x: longitudinal strain

ε_y: lateral strain

μ: Shear modulus

μ_0: initial shear modulus

σ: Stress

σ_x: longitudinal stress

List of Abbreviations

BW: Body weight
CAD: Computer aided design
CAE: Computer aided engineering
CT: Computed Tomography
EPOT: Electrical potential
EVA: Ethylene Vinyl Acetate
FE: Finite Element
FEA: Finite element analysis
FEM: Finite Element Method
FP: Frontal plane
FS: Forefoot Strike
FSR: Force sensitive resistor
GRF: Ground reaction force
GUI: Graphic user interface
MRI: Magnetic resonance imaging
NDT: Navicular drop test
PZT: Lead Zirconate Titanate
RS: Rearfoot Strike
SP: Sagittal plane
SPM: Statistical parametric mapping
TP: Transverse plane
VTK: Visualization toolkit

CHAPTER ONE

INTRODUCTION

1.1 Introduction

Elastic soft materials, such as rubber, with embedded thin stiffer layers (i.e. the in-plane dimension is much larger than the thickness) (as illustrated in Figure 1.1(a)), are increasingly being used in many products particularly within medical and sports engineering fields, such as embedded sensors, heating elements and various other applications (Harmeyer et al, 2009; Cannata et al 2016). The materials are also directly relevant to development in smart or multifunctional elastomeric materials for sensors, stretchable electronics, etc. (Shit and Shah, 2013). In many cases, the embedded/inserted structure has a much larger in-plane dimension than its thickness, and the material system may consist of embedment of different thickness and depth from the surface of embedment in different matrix materials (e.g. rubber, soft plastics, foams). Based on the relative material properties between the embedment and the matrix, one type can be termed rigid/inextensible inserts with the embedment having a much higher stiffness than the matrix. Typical cases included embedded electrical sensors (e.g. thin piezoelectric sensor of a thin copper sheet with ceramic coating and thin film thermocouples (Shit and Shah, 2013)), where the stiffness of these metals/ceramics coating is much higher than the matrix (typically silicone rubber/gel). Another type, which can be termed as deformable inserts, have a relatively softer insert embedded in silicone rubber. Typical examples include plastic inserts in silicone rubber for insoles or orthotics.

A detailed fundamental understanding of the mechanical behaviour of these material systems, under different loading conditions is crucial to the structural integrity of the system, functional performance of the embedment, as well as the reliability of these products. For example, a rubber based matrix is required to provide protection as well as flexibility under different loading conditions. One critical loading condition is indentation, which could cause damage to the matrix and the inserts resulting in malfunction (as illustrated in Figure 1.1(b)). Therefore, it is important to understand the effects of the matrix properties and the key design parameters, such as depth of the embedment from the sample surface, on the indentation resistance, compliance and deformation of the system.
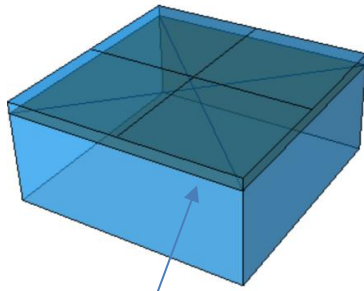
(a) Material system with an embedded stiffer layer in a homogenous matrix (elastic half space). Typical application wearable sensors, heating elements.
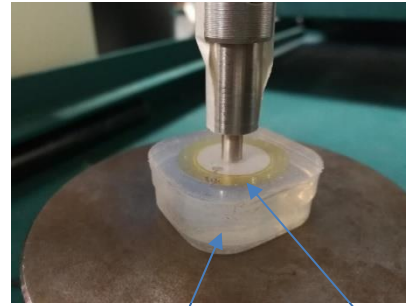
(b) A typical thin piezoelectrical sensor embedded in a silicone rubber matrix under indentation load.
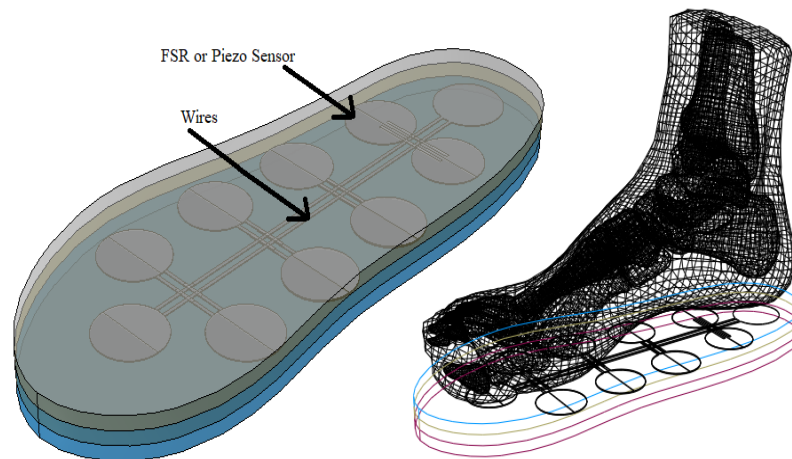
(c) Schematic to show the shoe sole with embedded system (thin Force sensitive resistor (FSR)or piezoelectrical sensor)

Figure 1.1 Schematic to show the material systems with an embedded layer with larger or finite size samples.

The development of footwear is strongly influenced by the application of new materials. Materials with negative Poisson's ratio have been the topic of research and development for several decades (Lake, 1987; Almgren, 1985; Wojciechowski, 1987; Jopek et al, 2016; Milton, 1992; Elipe and Lantada, 2012). Auxetic structure is able to expand in tension rather than shrinking. It is well documented that negative Poisson's ratio influences the material deformation under localised deformation such as indentation (Chan and Evan, 1998; Lim 2014; Photiou et al, 2016) Most of the earlier work has been focused on foam structures, while recent investigation/predictions on the isotropic auxetic materials have increased with the development of new auxetic material systems at different scales (Liu et al, 2009; Narojczyk et al, 2016; Zhu et al, 2015; Argatov et al, 2012; Aw et al, 2015). A recent study performed by Argatov et al (2012) investigated indentation and impact compliance of isotropic auxetic materials from the continuum mechanics viewpoint, the effect of Poisson's ratio and auxeticity is found to be dependent

on the shape of the indenter, a stronger effect of Poisson's ratio for a flat ended indenter than that for a spherical indenter is predicted. Furthermore, Photiou et al (2016) illustrated via theory and numerical modelling, that the negative Poisson's ratio has much stronger influence on the normalised hardness than the positive Poisson's ratio. The work also shows that evolution of different material constants (E, G, K) as a function of Poisson's ratio follows a different trend over the positive to negative domains. Previous work of the group on thin membranes with fixed boundary conditions (Aw et al, 2015), which is a situation also relevant to the embedded thin membranes, it is highlighted that negative Poisson's ratios have direct influence on the deformation, the force–displacement curve, the deflection profile and the contact area. It should be noted that when a thin membrane/shell is embedded in a matrix, the deformation of the system (matrix and embedment) under localised/pointed deformation (indentation) is much more complex due to the combined interaction from the matrix, the shell properties and the depth of the shell under the indenter. Hence, a systematic investigation is required to investigate the deformation of the material system and factors affecting the indentation resistance/stiffness, which are critical factors for the design and application of such systems as well as developing new material systems. It is of great interest to systematically investigate the effect of the Poisson's ratio in particular auxeticity (Wojciechowski, 2003; Gasper et al, 2005; Grima et al, 2013; Sanamia et al, 2014; Ha et al, 2016; Bilski et al, 2016) on systems with embedment in an elastic soft matrix through numerical and experimental methods. Given the many variables involved compared to conventional homogenous materials, a more advanced parametric system based on python program is required, in which the key parameters can be controlled and modified through a user interface. The work is particularly relevant to the analysis of foot mechanics and footwear related products such as embedded sensors for pressure measurement, energy harvesting, etc, shoe sole design, as well as prosthetics in which a rigid structure is embedded in a soft silicone rubber matrix.

Python program is increasingly used in materials and engineering as well as biomechanics. It can offer a much more effective way for data input (such as indenter size, materials properties, mesh density, etc). It has been used in work such as gear design, fatigue. It is suitable for systems with multiple dimensional or material parameters. A Python based plug-in allows a tool for the study of embedded thin sheet in a matrix with high efficiency given the multiple parameters involved. Another area where Python programming is also of great interest is the biomechanics of the foot. The foot has relative

fixed shapes and structures, but the loading condition can be complex such as landing angles, position, as well as change of material's property. Development of a parametric FE modelling system will provide a useful tool for the investigation of some key issues such as forefoot and rearfoot landing, comparisons between the standard standing and inversion landing (i.e. landing at an high angle between the foot and the ground). Many sensors in sport are in thin sheet, such as piezoelectrical sensors, force sensitive resistor, insert used in insoles and midsoles. Work is required to develop a proper research approach to model and predict the performance of such systems. It is also of interest to assess how such a system may affect the response of the foot or the measurements. For example, if wire sensors alter the foot plantar pressure, then it is not accurate. A proper program can be used as a tool to evaluate the potential effect of these system as well as materials with special properties, such as Negative Poisson's ratio. This will help to apply the material in sport related areas through the use of advanced computational modelling.

1.2 Aims and Objectives

This work aims to develop a Python based numerical approach for modelling a materials system with an embedded stiffer layer in a softer matrix under localised loading and the foot biomechanics with different loading and materials systems.

Main objectives are:

• To develop Python based FE models of thin embedment in a matrix under indentation load in elastic half space and finite sized samples

• To investigate the effect of Poisson's ratio and Auxeticity on the behaviour of embedded system under indentation.

• To apply parametric modelling of foot under different loading conditions, landing orientation and materials and assess the potential effects of embedment in the sole and auxeticity on the foot-sole interaction

• To model and analyse typical sensors used in footwear (including piezoelectrical sensor and force sensitive resistor) covering both mechanical and electrical output

1.3 Outline of the thesis

In Chapter 2, the main background and literature related to some key technology and research area is reviewed. The design requirements of shoes and the recent technological development of footwear and biomechanics involving the use of embedded system is presented. The functions and structure of the human foot and different deformation and movements in different orientation and axis is presented. Some key research methods are explored in biomechanics and Plantar pressure measurements with embedded force sensitive sensors and typical distributions under different conditions from experimental and numerical modelling highlighting the challenges and importance of future program development (user interface with Python) for model development and data analysis. FE modelling and its applications in sport materials and foot mechanics are presented based on recent works (foot and footwear modelling). Deformation of materials and strain energy for nonlinear materials behaviours are reviewed and summarised, which is important for the development of user plug-in for modelling materials testing and foot and shoe mechanics with or without embedded system. The theory background on viscosity is also presented. Auxeticity of materials and recent research on the material behaviour and applications are presented. The theoretical frame and current research on using Python in engineering modelling and materials have been critically reviewed and potential improvement is discussed. The challenges related to the key focus of the research work are highlighted with some background and future applications.

In Chapter 3, the research set-up and details of some key experimental facilities and materials are presented. The facilities for shore hardness, compression and tension tests for different types of samples are presented. The facilities used to make silicon rubbers and samples with a thin shell embedded in silicone rubber are also presented. The main materials samples, including piezoelectrical sensor and force sensitive resistor embedded in silicone rubber made in laboratory are also presented.

Chapter 4 focused on the modelling and analysis of indentation of soft materials with an embedded stiffer layer focusing on developing the modelling approach and analysing the effect of the properties of the matrix and the embedment. The deformation of an isotropic soft matrix with a buried stiffer thin layer under a circular flat indenter was investigated through finite element (FE) modelling. A practical approach in simulating the indentation resistance of such a system (soft matrix with a buried thin stiffer layer) is evaluated. The numerical result is correlated with the data based on analytical approaches for both homogenous materials and elastic half space with an embedded stiffer layer. The

influence of Poisson's ratio and auxeticity of the matrix on the deformation and indentation stiffness of the material system under different conditions (indenter size, sheet thickness and embedment depth) were established and main influences of the Poisson's ratio on the material deformation and stresses are discussed. Research work and analysis of two case studies related to embedded system is briefly presented and discussed. The first case shows some typical results on samples in which a piezoelectrical sensor and force sensitive resistor are embedded in a silicone rubber matrix. The FE model covered both mechanical modelling and electrical outputs simulation. The comparison between the testing data and numerical results further validate the modelling approach. The second case study presented some typical results in modelling auxetic structure and potential influence of using auxetic mesh as an embedment on the indentation resistance.

Chapter 5 focused on the use of a new developed Python based Abaqus plug-in investigating the deformation of the human foot in different landing conditions. In the first section, an FE foot model is developed to simulate the deformation of the human foot under a standing position to simulate a Navicular Drop Test. The models used a full bone structure and effective embedded structure method to increase the modelling efficiency. The detailed deformation of the Navicular bone and factors affecting the Navicular bone displacement and measurement is discussed. The second part is focused on the comparative study of the stresses and energy in the foot during forefoot strike (FS) and rearfoot strike (RS). A hexahedral dominated meshing scheme was applied on the surface of the foot bones and skin. An explicit solver (Abaqus/Explicit) was used to simulate the transient landing process. The deformation and internal energy of the foot and stresses in the metatarsals are comparatively investigated. In the third part, the effect of some key parameters of a shoe sole such as stiffness, thickness, an embedded shell and negative Poisson's ratio is evaluated using the FE models developed. Potential approaches of using auxetic structures and randomly distributed 2D inclusion embedded in a soft matrix for footwear application are discussed. The design and modelling of foot prosthetic, which resembles the human foot structure with a rigid structure embedded in soft matrix is also presented.

In Chapter 7, overall conclusions are given and future works is recommended.

CHAPTER TWO LITERATURE

REVIEW

2.1 Introduction

In this chapter, the main background and literature related to some key technologies and the research area are reviewed. The design requirements of shoes and the recent technological development of footwear and biomechanics involving the use of an embedded system are presented. The functions and structure of the human foot and different deformation and movements in different orientation and axis are presented. Research methods in foot biomechanics and Plantar pressure measurements with embedded force sensitive sensors and typical pressure distributions under different loading conditions from experimental and numerical modelling are introduced. The challenges and importance of future program development (including user interface with Python for modelling and data analysis) are highlighted. Finite element modelling and its applications in sport materials and foot mechanics is presented based on recent works. Deformation of materials and strain energy for nonlinear materials behaviours is reviewed and summarised, which is important for the development of a user plug-in for modelling material testing, foot and shoe mechanics with or without embedded systems. Auxeticity of materials and its influence on the material behaviour and applications are presented. One main focus of this thesis is to study the effect of negative Poisson's ratio on the indentation resistance of a material system with/without embedment under simple point loading condition (i.e. indentation with a flat and spherical indenter) and complex conditions in foot-ground interactions. The theoretical frame and current research on using Python in engineering modelling and materials have been critically reviewed and potential improvement is discussed. The challenges related to the key focus of the research work are highlighted with some background and future applications.

2.2 The design requirements of shoes and recent developments involving embedded systems.

Figure 2.1 shows the structure of the shoe. Shoes can be broken down into 4 main areas: upper shoe, inserts, mid-soles and the outsole. The upper shoe functions are mainly to hold the sports shoe together, it also helps to stabilize the foot during running and one of the main non-biomechanical factors is to make sure the sports shoe is aesthetically pleasing. The sole system consists of inserts, mid-soles and the outsole. The functions of the inserts are to help arch support and to dissipate heat and moisture away from the foot. Traction, wear resistance and shock absorption are the main functions of the outsole. The mid-soles function, which is the most important part of a sports shoe, is to control excessive foot motion (mainly pronation), provide cushioning and shock absorption, help prevent injury and fatigue and help limit the peak impact forces in heel strike whilst running. Material properties no doubt contribute to altering pressures. The function of the outsole is to provide the foot support, wear resistance and the traction. It is normally made of rubber or a plastic such as nylon.
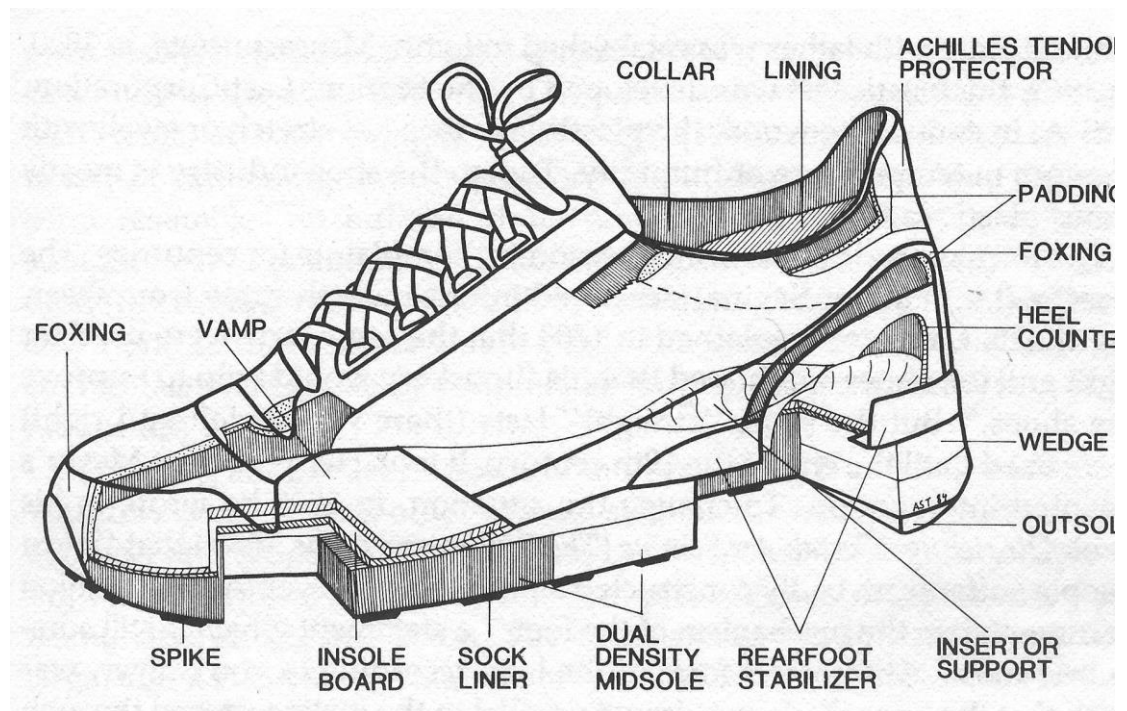
(a) Typical Structures of a sport shoe (Nigg, 1988).
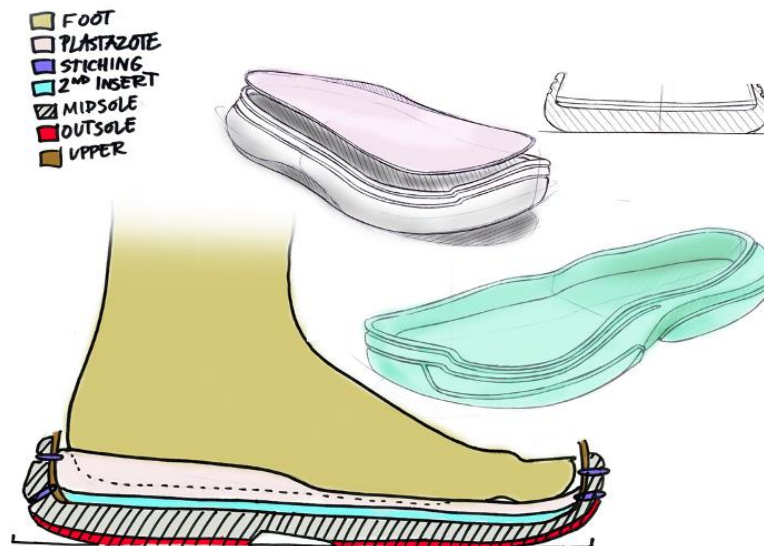
(b) Schematic to show the layout of the foot, insole, midsole and the outsole.

Figure 2.1 Schematics to show the layered structures of the shoe sole and interface between the sole and the foot.

The mid-sole of a sports shoe aims to help spread the impact forces so the peak ground reaction force is not placed directly to the foot, leg and knee, which is how most injuries occur. A good mid-sole design is one that will provide some type of energy back to the body when compressed (Shorten, 2000). Durability is an important property in sports shoe design. Verdejo and Mills (2004) have stated that mid-sole durability is very important, it relates directly to the cushioning and the fatigue from impact attenuation. Ethylene Vinyl Acetate (EVA) foams are usually used for the mid-sole cushioning. EVA foam is made up of tiny gas bubbles; the molecular structure and number of bubbles can affect the material's strength and hardness. During a long-distance run, for example a marathon, Verdejo and Mills (2004) found that EVA foam doesn't fully recover, decreasing the cushioning and the energy returned to the athlete and therefore increasing the probability of injury.

Comfort and functionality are features increasingly demanded by the consumers. Footwear comfort is the result of a complex interaction of several factors that affect the foot function during human activity. The main factor is to study the human feet, biomechanics and the human body in motion. Trying to understand the design and construction of good shoes would be difficult without the knowledge of what goes inside or above them. So shoe design requires the efforts of several academic fields including biomechanics, materials development, modelling, etc.
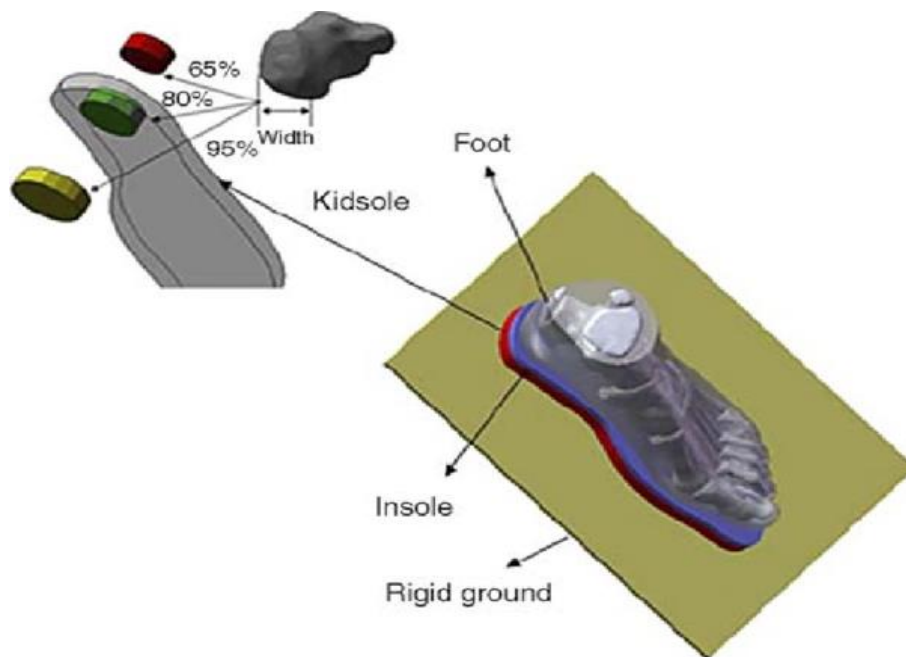
(a) Midsole Plug design with different materials to manage the pressure. (Gu et al 2011)
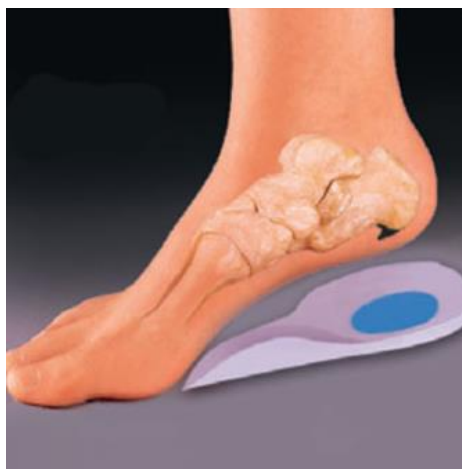
(b) Silicone insole with different insert/embedment for pressure managements.
Figure 2.2 (a) Midsole Plug design with different materials to manage the pressure. (Gu et al 2011); (b) Different types of insoles with different partition regions.

One approach to improve the footwear function is using different materials over different anatomical zones of the foot. For example, plugs or inserts made from different materials are used to control the pressure under the heels and stresses in the metatarsals (Gu, et al, 2011; Mei et al, 2015). As shown in Figure 2.2 (a), foams of different hardness are used in the midsole to control the pressure over the heel regions. Figure 2.2 (b) shows another case, in which a different layer of material is used in a soft insole to control the

deformation. In many cases, the insert/embedment is much thinner than the matrix. The insert is much larger in the in-plane direction than the thickness directions. Most of these designs with hybrid or multiple components materials in footwear design were for enhancing the footwear functions, such as protection, performance enhancement, appearance, etc. Increasingly new technological developments have been integrated in the footwear systems (Figure 2.3) (such as energy harvest, sensors for position (GPS), pressure and force monitoring). This requires new research into foot shoe interaction and testing of materials. In energy harvest, the energy is normally harvested by a piezo plate, which is thin with a copper base and PZT (or lead zirconate titanate) ceramics. It is normally embedded in the insole or the midsole. The bending of the ceramics generates electricity when being deformed (Jaffe, 2012). As shown in Figure 2.3(c), normally multiple piezo sensors are used in different regions. The electricity generated is related to the frequency and the magnitude of the sensor, A good understanding of the deformation of the piezo in different materials (rubber) or foams is important to the energy harvester efficiency. There are other situations in which piezo-sensors are used in energy harvesting, such as car tyres (Eshghi1 et al, 2017; Jung et al 2017).
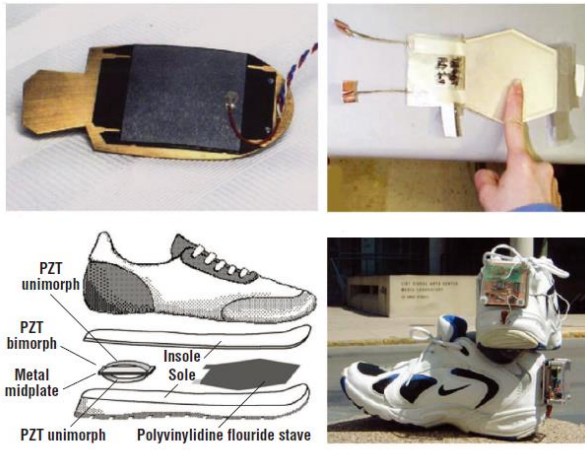
(a) Energy Harvest system with thin Piezo. (Paradiso and Stamer, 2005).

(b) A typical piezoelectric sensor.

(c) A low-cost Insole used in Kinetic Gait Analysis (Howell et al 2013).

(d) A typical force sensitive resistor (FSR).
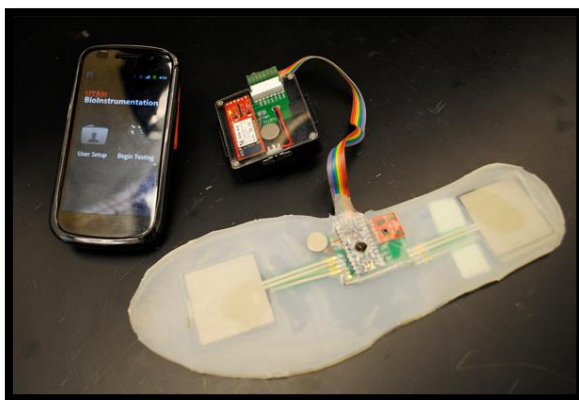
(e) Silicone gel insole embedded with electric sensor for rehabilitation (Bamberg *et al*, 2008).

Figure 2.3 Use of different thin structures in advanced footwear and wearable technologies.

Force-sensitive resister (FSR) is another form of thin sensors based on the resistance change. When pressure is applied the sensor measures the resistance of conductive foam between two electrodes. The current through the resistive sensor increases as the conductive layer changes (i.e., resistance decreases) under pressure (Razak et al 2012; Howell et al, 2013). FSRs are made of a conductive polymer that changes resistance with

force. Applying force causes conductive particles to touch increasing the current through the sensors. The load over different foot region is monitored (Figure 2.3 (d)&(c)). For example, for diabetics, Morley *et al* (2001) developed an insole-based system to quantify the conditions inside the shoe, to predict the progression of skin breakdown and ulceration in diabetic patients with peripheral neuropathy. Pappas *et al* (2002) used a pattern recognition algorithm to define the transitions during the gait cycle using their device consisting of three Force Sensitive Resistors located on an insole (one under the heel, and two at the first and fourth metatarsal heads), and a gyroscope. The system was tested on two subjects with incomplete spinal injury and was used to trigger functional electrical stimulation, with demonstrated benefit for both subjects (Bamberg *et al, 2008)*. For cycling shoes, ultra-stiff carbon fibre composites are now being placed in the midsole and/or outsole of both road and mountain bike racing shoes. Currently, stiffer cycling shoes made from composite materials are designed to transfer energy more efficiently from the legs and feet to the pedals, although this is not well documented. In addition, the development of breathable shoes normally is composed of a porous material. Material with micropores which are smaller than water drop but bigger than molecule of vaporized water can be breathable but waterproof. Water cannot enter the shoes from exterior and feet stay dry. New concepts need to be developed in designing new insoles specifically for embedded electronic systems.

Recently, there has been considerable work in instrumented shoes and wearable technology shoes for both research purposes and technological development, in which a thin electronic device or chip is embedded in the sole system. this poses a new challenge in material and design of shoes (Crea *et al* 2014). There has been considerable previous work in both research and commercial spheres focused on the development of more mobile methods of analysing gait. The advantage of directly measuring the pressure distribution beneath the foot which has encouraged the design and application of many different systems, as shown in Figure 2.3(e) (Bamberg *et al,* 2008). For example, the shoes sole/insole with embedded flex-circuit can profitably be used for gaming, biometric monitoring, and activity tracking and wireless sensitized insole (Crea *et al,* 2014). The system consists of a flexible insole with 64 pressure-sensitive elements and an integrated electronic board for high-frequency data acquisition, pre-filtering, and wireless transmission to a remote data computing/storing unit. Wearable systems have to be attached to an external apparatus, or are limited by their battery capacity, data storage and other device specific factors. A new tool (OpenGo, Moticon GmbH) has recently

introduced a system to continuously measure kinetic and temporo-spatial gait parameters independently through an insole over up to 4 weeks (Braun *et al*, 2015). This insole weighs less than 80 grams and is similar to regular insoles worn by runners. However, it is equipped with 13 capacitive pressure sensors, a 3D accelerometer, and a temperature sensor. It measures peak pressures, pressure distribution, acceleration, motion sequences, gait patterns and temperature (from Transfer report).

The new technologies in shoe design both for mechanical functions and the new control or monitoring function require further work to investigate the mechanics of different systems. This could be applied in normal locomotion or in sports like running and cycling. Thus, the strategies to study and modelling with the embedded system are essential. It can potentially provide new ways to predict the material response. On the other hand, properly embedding the measurement device becomes necessary to protect the electronic circuit, making sure they work properly, are durable and are reliable in high-performance motion tracking applications without sacrificing the shoe sole support to the human foot.

2.3 The structure, movement, deformation and plantar pressure of the foot

The understanding of the structure and movement of the foot is important for the study and effective modelling of deformation under different loading conditions. The design, service condition and the mechanical, and functional behaviour of the sensors or other embedment system in footwear (Kong et al, 2009; Nilsson et al, 2012; Maculewicz et al, 2016; Eshghi et al 2017) are also associated with the foot structure, system and loading conditions. In fact, the foot itself has a rigid bony structure encapsulated/embedded in soft tissue. In addition, some foot related products such as foot prosthetics resemble the foot structure with a strong structure embedded in silicone rubbers.

2.3.1 Foot structure

The human foot (Figure 2.4) is a very important part of the human body, which provides the direct source of contact with the supporting surface, and plays an important role in all weight bearing tasks. During gait, the foot contributes to shock absorption, adapts to irregular surfaces and contributes to generating momentum for forward propulsion (Scott et al, 2007). The feet need to be stable and supportive, flexible, and energy efficient to be able to support the body weight, withstand the forces generated by contact with the ground, propel the body forward, and cope with uneven surfaces and various types of footwear (Briggs, 2005). These functions are supported by a complex structure and materials system. The whole foot is made up of bones, cartilages, muscles, tendons and ligaments. There are thirty three joints in the foot and more than one hundred muscles, tendons and ligaments. In addition, there is a network of blood vessels, nerves, skin, and soft tissue (Rohen and Yokochi, 1988). Normally, the foot is considered as having three main parts: the forefoot, midfoot and rear foot (Figure 2.4). The rearfoot (hindfoot) articulates with the midfoot through the talonavicular and calcaneocuboid (midtarsal) joints, and the forefoot is connected with the midfoot through the tarsometatarsal joints. These parts work together to provide the body with support, balance, and mobility. The supportive function of the foot is mainly provided by the bones, joints and ligaments of the midfoot, the central tarsometatarsal joints, and the midtarsal joint. Subtalar, talonavicular, and medial and lateral tarsometatarsal flexibility allows the foot to adjust to uneven ground and for the changing shape of the foot during heel elevation and propulsion. The plantar aponeurosis and deep transverse intermetatarsal

ligaments support the foot and also have dynamic functions in stabilisation and movements (Kitaoka, et al., 1997).

(a) Bone structure of the human foot (MMG 2001)

(b) Main soft tissues of the foot.
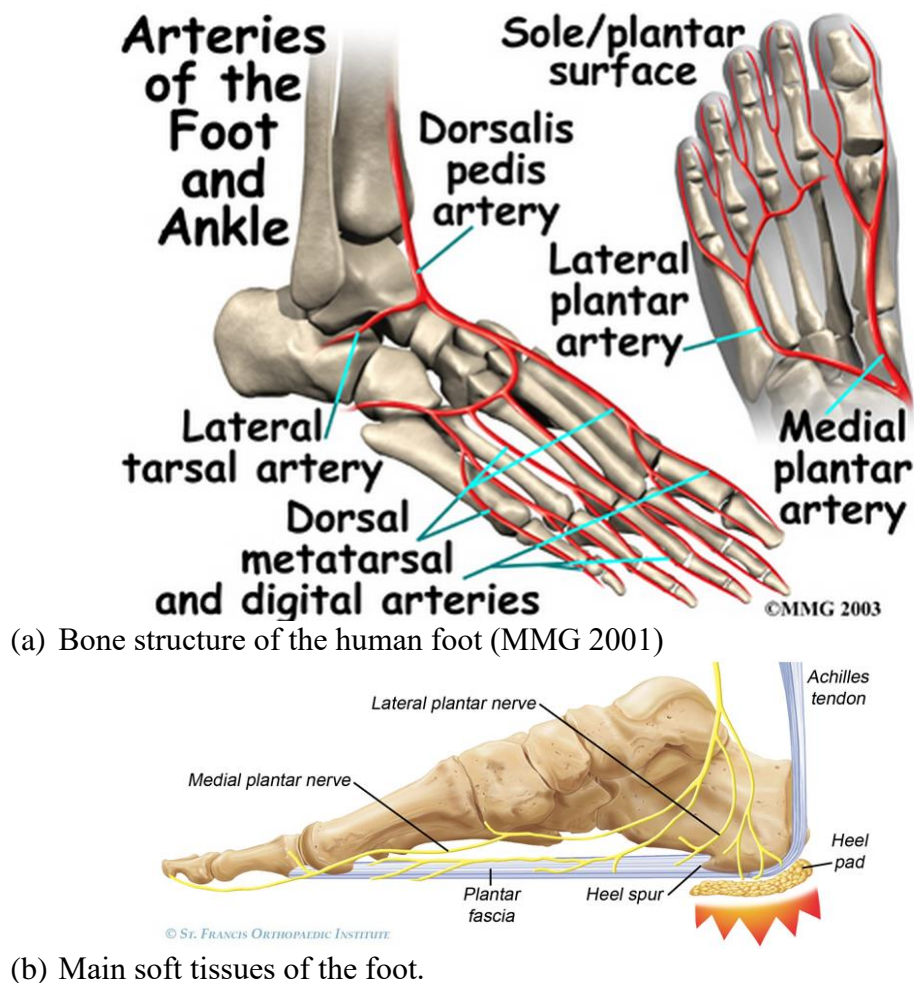
Figure 2.4 Structure of the human foot.

The underlying structure of the foot allows it to undergo complex deformation and movement for different functions. In order for the foot to propel us forward efficiently, it must be able to change between being a strong rigid structure and a softer more flexible one. The combination of the stable and sturdy 3-arched bone structure and the more mobile and elastic soft tissues means that the function of the foot can alternate between the following states: (i) the foot is a mobile adapter - the soft tissues expand which allows the arches to lower. This action is the body's defence mechanism, designed to prevent damage and jarring to the weight-bearing joints throughout the body; (ii) the foot is also a rigid lever - the soft tissues contract which causes the arches to heighten. This rigidity provides the strength and power that propels us forward. The sequence and timing of the foot motion as it switches between a mobile adapter and a rigid lever is termed the Gait Cycle (Winter, 1979).

2.3.2 Movement and deformation of the foot

Joints of the foot are controlled by extrinsic and intrinsic muscles of the lower limb and provide for major motion function, angulation and support of the foot (Kura et al., 1997). Motion occurs by rotation about an axis in a plane of motion for all the joints. The foot may undergo different types of movement in locomotion. In general it can be classified into three main types in accordance with different planes and axes (Figure 2.5). The three planes of motion in the foot are defined as: sagittal plane (SP), frontal plane (FP) and transverse plane (TP). The foot, or any part of the foot, is defined as adduction when its distal aspect is angulated towards the midline of the body in the transverse plane and deviated from the sagittal plane passing through the proximal aspect of the foot, or other specified anatomical reference point. Abduction occurs when the distal aspect is angulated away from the midline. The foot is defined as being plantar flexed when the distal aspect is angulated downwards in the sagittal plane away from the tibia, and dorsi-flexed when the distal aspect is angulated towards the tibia in the sagittal plane. The foot is described as being inverted when it is tilted in the frontal plane, such that its plantar surface faces toward the midline of the body and away from the transverse plane, and everted when its plantar surface faces away from the midline of the body and away from the transverse plane (Wright, et al., 2000).

(a) Abduction	(b) Adduction
(c) Plantarflexion	(d) Dorsiflextion

| (e) Eversion | (f) Inversion |
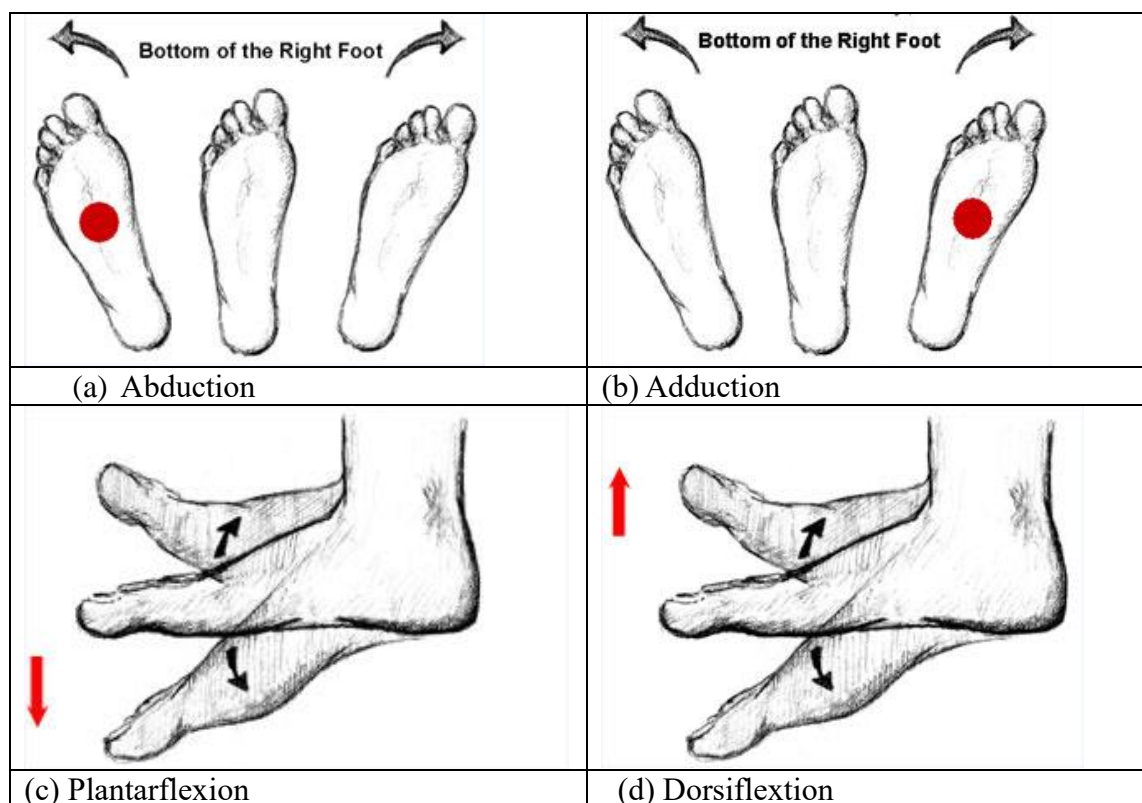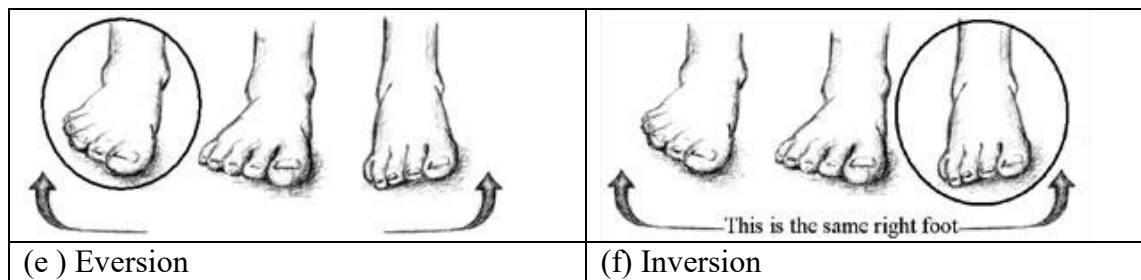
Figure 2.5 Typical movements of the foot in different planes and axis (Mann R.A 1985).

The deformation of the foot during different movement and contact with external objects is a complex problem and excessive deformation may cause injury to the bone or the soft tissues (Burns et al., 2005). Accurate positioning of the foot at touchdown is very important in gait and sports. It has been assumed that biomechanical abnormalities (such as inversion angles) in sports are one of the causes of injuries. For example, it has been frequently hypothesized that contacting the ground at an increased inversion position could result in an ankle sprain and metatarsal fracture (Wright et al., 2000; Logan et al., 2007). The tilting platforms used by some researchers to study these abnormal conditions allowed participants to drop primarily into inversion with range to 30 degree (Benesch *et al.* 2000; Sefton *et al.* 2007), replicating the frontal-plane motion that commonly causes lateral ligament sprains. In addition, some research work has suggested that the inversion position is an important factor related to the fifth metatarsal injury (Ekrol and Court-Brown, 2004).

2.3.3 Plantar pressure measurements and distributions under different conditions.

Gait analysis is the systematic study of human locomotion, by collecting kinematic and kinetic data during walking. The pattern of walking is usually quantitatively measured by force platforms, pressure measurement plate and insole. One major method in materials and biomechanics for foot prosthetics is pressure measurement. In these technologies, a fine grain matrix array of sensors measures the force when the foot contacts the sensor. Systems of this type are bulky, expensive and not practical for a consumer outside of a laboratory setting. Figure 2.6(a) shows a specific plantar pressure measurement insole with 99 force sensors with a linear response to applied loads ranging from 0 to 50 N/cm^2. The system uses capacitive pressure sensors separated by a dielectric elastic layer. Once a pressure is applied, the dielectric elastic layer bends, which shortens the distance between the two plates resulting in a voltage change proportional to the applied pressure. Sensors were arranged in a way reflecting different anatomical regions as shown in (b).
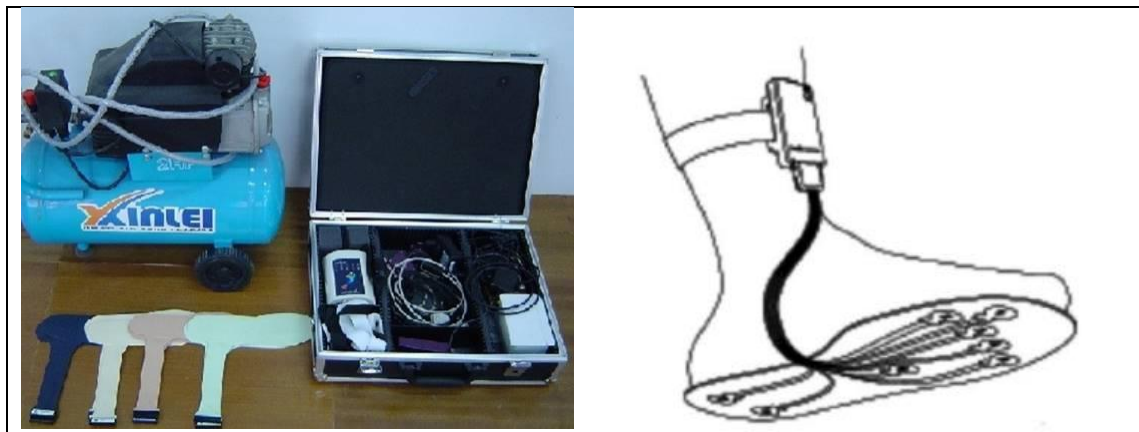
(a) Insole plantar pressure measurement system (Novel, Munich, Germany).

LT: Lateral Toe
BT: Big Toe
LMF: Lateral Mid-Foot
MMF: Medial Mid-Foot
M_1: 1st Metatarsal
M_{2-3}: 2nd and 3rd Metatarsal
M_{4-5}: 4th and 5th Metatarsal
H: Heel
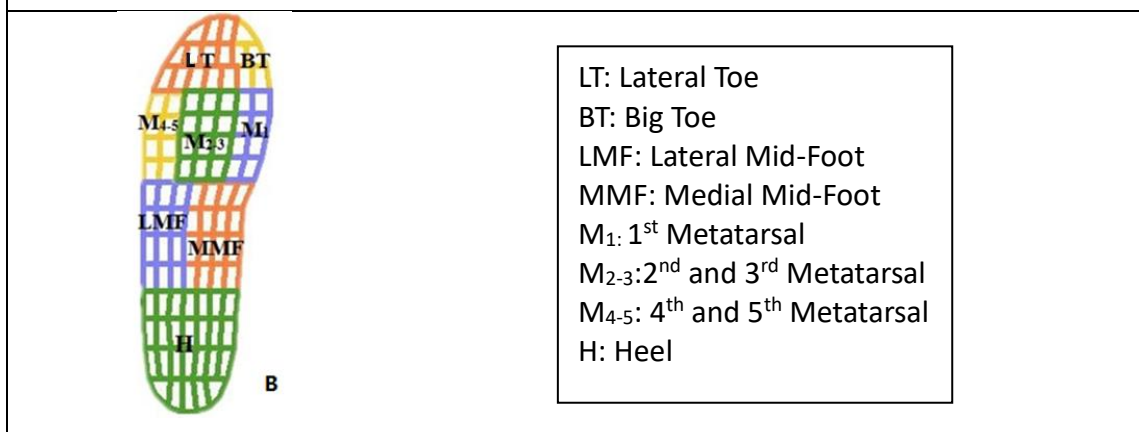
(b) Main regions of the sole.

Figure 2.6 Main functional regions of the sole during pressure measurement and the principle of plantar pressure measurement system (Gu *et al*, 2013).

Gait analysis is mainly applied in the fields of clinical environment or for sports analysis, such as assessment of gait pathologies, and the prevention of pressure ulcers in diabetes (Smith *et al,* 2000) or the assessment of the causes of an orthopaedic disease in the clinical environment. Besides, gait analysis carried out for sport purposes is aimed at helping athletes to gain a high level of performance (Queen *et al*, 2007), while minimising the risk of painful injuries to shins and joints. Finally, scientific research laboratories use gait analysis to study mechanisms of human musculoskeletal system and cerebral apparatus. Each of these application fields uses different gait analysis techniques to pursue specific aims (Crea *et al,* 2014). However, due to the expensive and highly specialized equipment required, gait studies are mostly limited to academic research centres and small sample sizes, no large-scale, randomized controlled trials have been performed (Braun *et al*, 2015). Figure. 2.7 (a-c) shows an example of in-shoe plantar distribution under inversion landing (Gu *et al*, 2010). Footwear optimization needs to consider complex abnormal landing conditions. This study compared plantar pressure

distribution in inversion foot landing (a) simulated by FE modelling and measured by Novel insole (b). Figure 2.7(b) highlights the pressure distribution during the forefoot touching down. The FE and experimental measurements showed a reasonable agreement in the plantar pressure distribution and peak pressure value. The work revealed that, during inversion landing, peak stress point was found to be near the proximal part of the fifth metatarsal, as seen in Figure. 2.7(c).
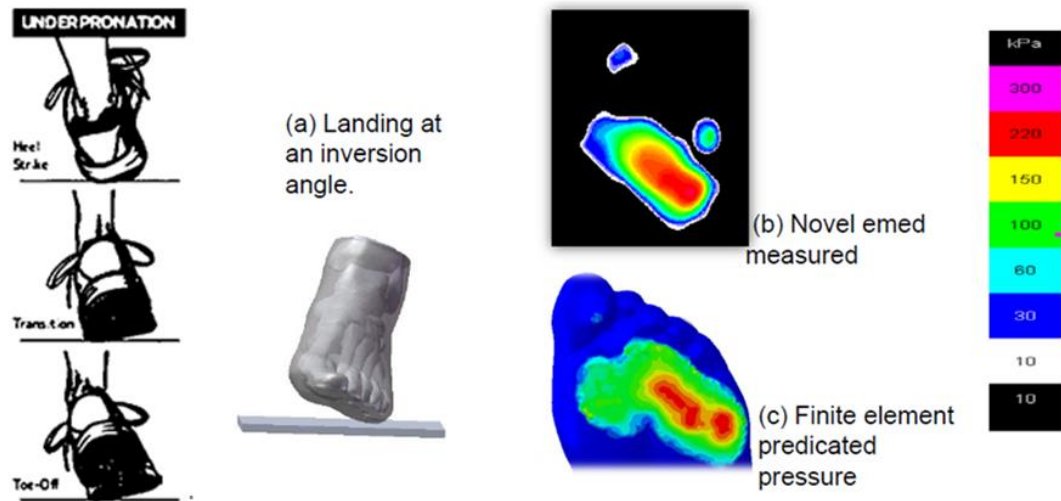
Figure 2.7(a-c) Plantar pressure distribution during landing at an inversion angle (Gu *et al,* 2010).

(d) Typical clipless pedal and shoe interface in cycling.
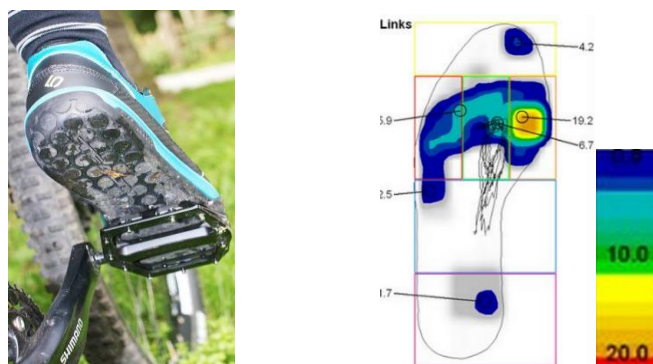
(e) Plantar pressure distributions in cycling.

Figure 2.7(d-e) Foot, shoe and pedal interaction.

(*http://www.speedplay.com/index.cfm?fuseaction=home.fit*)

Similar techniques have been used for studying the pressure distribution in cycling. The mechanics of bicycle pedalling involves the transfer of force from the muscles of the leg through the foot and onto the pedal surface. A typical setup and pressure distribution are shown in Figure 2.7(d-e). Henning *et al* (2010) studied 39 subjects riding on a stationary bicycle with a cadence of 80 rpm at 100, 200, 300, and 400 W. The result indicated that the plantar pressure distribution of cycling is different from running and walking. The first metatarsal head and the hallux were identified as the major force-contributing structures of the foot. The generation of pedal forces resulted in high pressures under the toes, midfoot, and under the heel; this showed that all foot areas contribute substantially to the power increasing; higher peak pressures and relative loads under the medial forefoot were identified. These may cause pressure-related forefoot complaints and accompany increased foot pronation. As compared to running shoes, the stiff cycling shoe demonstrated a more evenly distributed load across the whole foot and showed a significantly increased index of effectiveness. Metatarsalgia is a common problem among cyclists; Ou-Yang *et al (2015)* reported higher local pressure during cycling was specifically linked to metararsalgia and is also likely to cause other foot problems. Mean peak pressure recorded in the experiment shoe of plastic sole (type M152) was 103.0 kPa and the mean for the carbon sole (M220) shoe was 121.2 kPa. Besides, Andrea *et al* (2011) stated that clipless pedals produce higher pressures which are spread across the foot more broadly than toe-clipped pedals. This indicates implications in the prevention of overuse injuries in the knee and foot.

2.4 FE modelling and its applications in sport materials and shoe design

FE modelling is an effective way of studying complex sport materials and biomechanics. For example, Shariatmadari *et al* (2010) used an FE model to look into the temperature dependence properties of elastomeric foams and their effects on the forces transmitted to the foot. In the work, an FE model are developed to simulate non-linear large deformation problem of foot – footwear interaction. The interface pressure between the heel pad and the shoe for each model was obtained. These data are useful in developing design guidelines for orthotic intervention for reducing stresses in the foot. The finite element method is also used in the medical field to study the effect of various soles such as orthopaedic or high heel soles on foot plantar pressures (Yu *et al*, 2008). In another study, Kim *et al* (2012) developed an FE model to study the effects of sports ground materials on landing impact forces using a coupled foot-shoe-ground finite element model. Recently, Sissler *et al* (2013) developed an experimentally driven dynamic 3-D finite element model of the foot-shoe assembly predicting the effect of the interactions between the foot and the shoe on the sole behaviour during a walking cycle. As a result, they found the comparison between the experimental and simulated impact test results showed good agreement for the force deformation curves, including the hysteresis or energy loss. FE model can be used in computer aided design as well to link biomechanics and design. A typical system is shown in Figure. 2.8 (Cheung *et al*, 2009) The design process involved three stages. The first task of this CAE approach was acquiring geometrical data of foot and footwear structures. The MRI scanned foot images were used for 3D reconstruction of foot soft tissues and bones. The reconstructed model in STL file then underwent surface reconstruction and smoothing for the creation of solid CAD models. The next step of the pre-processing procedure was acquiring material, loading and boundary properties for establishing FE simulation. The soft tissue and shoe sole of the current model were defined as hyperplastic while the foot bones, ligaments and ground support were assumed as linearly elastic.
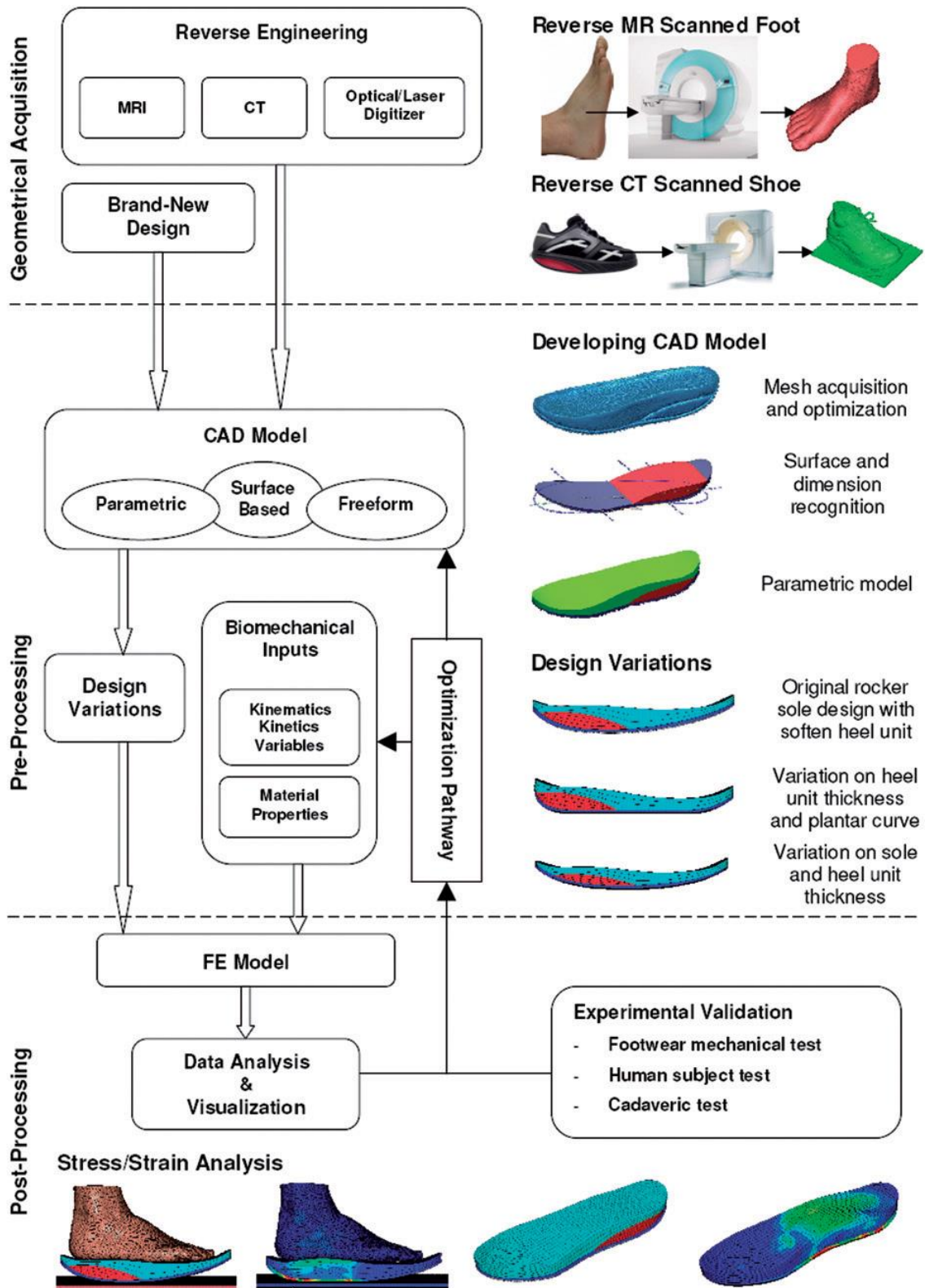
Figure 2.8 CAD process of insole or midsole design (Cheung *et al*, 2009).

2.5 Foot mechanics of different landing styles

Foot biomechanics is relevant to the understanding of the foot deformation and shoe design. A lot of work has been done to characterize the foot mechanics in different loading conditions (such as forefoot and rearfoot, inversion and aversion landing, static standing, running, jogging, one leg hopping) (Gu et al, 2010, 2011; Cheung et al, 2014; Daoud et al, 2012, Fontanella et al 2012, 2016). In some cases it involves different footwear such as trainers, high heel shoes, dancing shoes, minimalist shoes. One particular area of interest is the difference between forefoot and rearfoot strikes. Foot strike pattern is a major issue influencing the lower extremity biomechanics during running. Forefoot strike and rearfoot strike are two common landing styles of running (Lieberman, 2012; Shih et al 2013).

In forefoot strike, the ball of the foot impacts with ground first, during which, the foot initially lands with a plantarflexion posture followed by a dorsiflexion movement. Compared to rearfoot strike, forefoot strike cuts down the impact and reduces the shock passing to the brain as the impact is absorbed by the compression of the foot arch, eccentric contraction of the triceps surae, calf muscles and Achilles tendon stretch (Lieberman et al 2010). The pressure excursion during forefoot strike that moves backward was once considered an energy waste but was later proven to provide cushioning for runners (Divert et al 2005). Recent researches showed that the vertical loading rate of a habitual barefoot runner can be significantly reduced by changing their landing pattern from rearfoot strike to non-rearfoot strike (Squadrone and Gallozzi 2009). In the work by Lieberman (2010), no obvious impact transients were found in the typical force-time data of forefoot strike. Conversely, the force-time curve of classic rearfoot strike always shows an impact transient before the vertical ground reaction approaches its peak. During the impact period of a rearfoot landing, the vertical Ground Reaction Force (GRF) can be 3 times higher than the forefoot landing of habitual barefoot runners (Lieberman 2010).

In rearfoot strike running, impact absorption is limited to the rearfoot pad and shoe, leading to a higher peak impact and generating the shock wave. This could lead to high stress and strain directly contributing to certain injuries (Daoud et al 2012). This is one of the reasons that running in minimalist footwear has been considered as a means of reducing or eliminating running injuries by returning to a more natural gait. Forefoot

landing puts metatarsals at the first place of impact, in which the metatarsal bones would bear more load compared to the stress in rearfoot strike or mid foot landing styles. This has been proved to be the case by insole pressure loading measurement (Kernozak et al 2014). In addition, it was also reported that the GRF and plantar pressure under the metatarsals were greater in the forefoot and phalanx during non-rear foot strike (Kernozak et al 2014). Forefoot landing pattern may also increase the potential of metatarsal injuries such as fractures. Recent case studies revealed that the use of minimalist footwear by novices, which may encourage rearfoot strike, caused a higher occurrence of metatarsal stress fractures (Giuliani et al 2011).

In order to understand the biomechanical mechanism of metatarsal injuries, internal stress should be studied. FE modelling provides the prediction of internal stress distribution of the foot under different loading conditions. FEM is commonly used in many biomechanical investigations with great success due to its ability to model complex material properties and irregular geometry, as well as simulating the internal stress in bones and tissue. Many studies have focused on the foot stress under static standing load (Gu et al 2011, Cheung et al 2005, Cheung and Zhang 2006). Stress in the bony foot structure was simulated during balance standing by Cheung noting a clear effect from the soft tissue stiffening and use of different types of foot support design Cheung et al 2005, Cheung and Zhang 2006), including the modelling of foot with medical conditions such as diabetic foot (Guiotto et al 2014). Edwards et al (2010) have successfully used a probabilistic model with the FE method to estimate the probability of stress fracture in a training scheme in which subjects ran at 3.5 and 4.5m/s over a period of 100 days.

In both cases, forefoot or rearfoot strikes, the high intensity impact induced when landing is a major factor for potential injury of foot bones or soft tissues. A comparative study of the foot deformations in these two landing phases will provide important data and impact characteristics within the relatively short time between foot-ground interaction. The improved understanding of the impact process simulated by FEM can also provide the information for enhancing the protection of the foot, designing devices embedded in shoe sole for smart shoes or implanted sensors. Wearable technology has been popular in the field of public health science, with more and more footwear setting a space aside for embedding a sensor to record plantar pressure and even foot movement in gait. The impact during landing is the most vulnerable phase for the sensors among the

whole gait cycle. Consideration of different landing styles (i.e. forefoot and rearfoot strike) in design of embedded or implanted sensors is necessary to balance the function of the sensors such as shoe sole stiffness, sensor reliability and wearing experience for different wearers of different strike patterns.

2.6 Deformation of materials and strain energy for nonlinear materials behaviours

A range of materials has been involved in this work, such as copper, ceramics, silicone rubber, particle-rubber mixtures and EVA foams. The related material models are reviewed in the following section.

Eq.2.1 describe a linear elastic relationship between compressive or tensile stress and strain, where the constant E is the Young's modulus.

$$\sigma_x = E\varepsilon_x \qquad (2.1)$$

$$v = -\frac{\varepsilon_y}{\varepsilon_x} \qquad (2.2)$$

Where,

The Poisson's ratio refers to the ratio of the lateral strain (ε_x) to the longitudinal strain (ε_y) as in Eq.2.2. Most materials have a positive Poisson's ratio due to shrinking in the lateral direction when being pulled. For example, metals (e.g. steel, copper, aluminium) have a Poisson's ratio between 0.2-0.3; Ceramics have a Poisons' ratio range 0.1-0.2, while the Poisson's ratio for polymers varies from 0.3 (for engineering plastics) to 0.5 for rubber (representing in-compressible, i.e. no volume change when deformed). The Poisson's ratio is close to zero when the material is fully compressible. For an isotropic material, the shear modulus μ can be calculated using:

$$\mu = \frac{E}{2(1+v)} \qquad (2.3)$$

2.6.1 Elastic–plastic behaviour of materials

A typical stress-strain curve of elastic–plastic materials (such as steel and plastics) is shown in figure 2.9(a). The engineering stress and strain, denoted as σ_e and ε_e respectively, are determined from the measured load and material deformation against the original specimen cross-sectional area A_0 and length L_0 :

$$\sigma_e = \frac{P}{A_0} \quad ; \quad \varepsilon_e = \frac{\delta}{L_0} \qquad (2.5)$$

Where, P is the applied force and δ is the deformation.

In the elastic portion of the curve, many materials obey Hooke's law; stress is proportional to strain with the constant of proportionality being the modulus of elasticity or Young's

modulus, denoted E, is defined as the ratio of the stress with the strain.

$$\sigma_e = E \ \varepsilon_e \qquad (2.6)$$

The three parameter power-hardening rule is commonly used as:

$$\sigma = \ \sigma_y + K \ \varepsilon^n \qquad (2.7)$$

which can describe the plastic behaviour, where σ_y represents the yield stress, ε represents the plastic strain, K represents the strength coefficient and n represents the strain hardening exponent. The Ludwig power equation is a simpler form which is used to describe isotropic elasto-plastic behaviour with isotropic work-hardening (Swift, 1952).

$$\sigma = \ K \ (\varepsilon_0 + \ \varepsilon)^n \qquad (2.8)$$

2.6.2 Hyperelastic material behaviour

As shown in Figure 2.9 (b), rubber is a highly non-linear material, which exhibits different material behaviours at different strain levels/loading modes, which could not be fully represented by Young's modulus, E. Hyperelastic material models are developed/defined as a relation between the total stress and the total strain. Stresses are determined by derivatives of the strain energy function, giving the second Piola-Kirchhoff stresses (Weiss et al., 2001). Many strain energy function models have been developed to characterise various material systems which undergo large deformations, typically Mooney-Rivlin model, Neo-Hookean form and Ogden model (Ogden, 1972; Petre et al., 2007). They are generally used to describe incompressible materials (such as rubber and gel structures). These material models have been integrated into several computational software packages including ABAQUS, which are briefly described below.
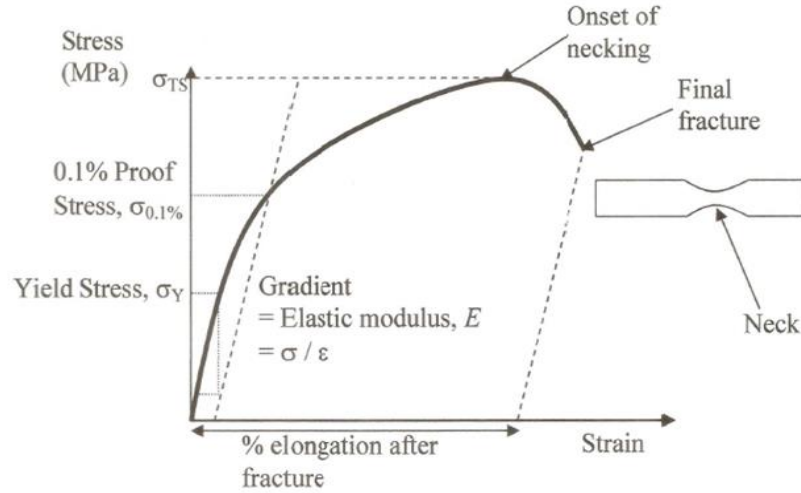
(a) Typical elastic and plastic stress-strain curve (*Wang, 2013*)
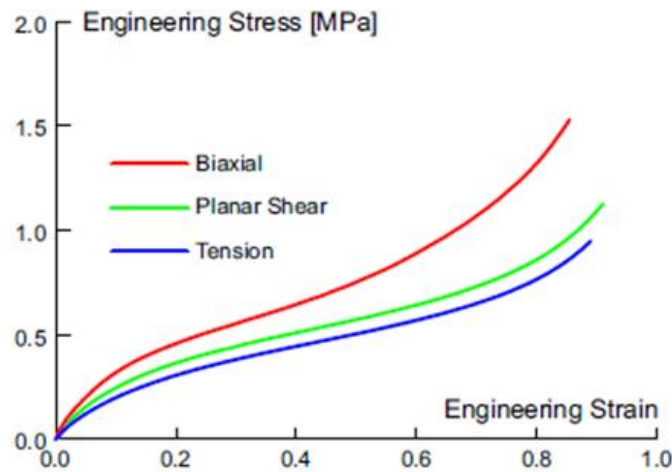
(b) Typical one-dimensional stress strain curves of rubber materials (*"White paper – Nonlinear finite element analysis of elastomers", MSC Software Corporation.*)

Figure 2.9 Different stress strain curves for elastic-plastic materials (metal and plastics) and hyperelastic materials behaviours.

2.6.3 Mooney-Rivlin model

Mooney derived an expression for the strain energy function for rubber as shown in Equation 2.9.

The linear form of strain energy function Mooney initially proposed is:

$$W = C_{10}(\bar{I}_1 - 3) + C_{01}(\bar{I}_2 - 3) \tag{2.9}$$

where C_{10} and C_{01} are constants and $\bar{I}_1, \bar{I}_2$ are the first and second deviatoric strain invariants. It is the most general form admitting a linear relationship between stress and strain in simple shear, and has since been referred to as the Mooney-Rivlin model. When particular parameters are used, this equation gives a marginally better fit to some of the experimental data of rubber than pure elastic models (*Atkin and Fox, 1980*).

The strain energy W (Equation 2.9) can be split into two parts, the deviatoric and volumetric terms. Then the form of the Mooney-Rivlin strain energy density becomes (*ABAQUS Manual 6.14*)

$$U = C_{10}(\bar{I}_1 - 3) + C_{01}(\bar{I}_2 - 3) + \frac{1}{D_1}(J^{el} - 1)^2 \tag{2.10}$$

where U is the strain energy per unit of reference volume; C_{10}, C_{01}, and D_1 are temperature-dependent material parameters, $\bar{I}_1, \bar{I}_2$ are defined as Equation 2.9.

$$\bar{I}_1 = \bar{\lambda}_1^2 + \bar{\lambda}_2^2 + \bar{\lambda}_3^2 \quad and \quad \bar{I}_2 = \bar{\lambda}_1^{(-2)} + \bar{\lambda}_2^{(-2)} + \bar{\lambda}_3^{(-2)}$$

(2.11)

$$\bar{\lambda}_i = J^{-\frac{1}{3}}\lambda_i$$

where the deviator stretches $\bar{\lambda}_i = J^{-\frac{1}{3}}\lambda_i$; *J is total volume ratio*; J^{el} is the elastic volume ratio. λ_i is the principal stretches. The initial shear modulus (μ_0) and bulk modulus (K_0) are given by λ_i.

$$\mu_0 = 2(C_{10} + C_{01}) \tag{2.12}$$

$$K_0 = \frac{2}{D_1} \tag{2.13}$$

2.6.4 Neo-Hookean form model

The form of the neo-Hookean strain energy potential is given by

$$U = C_{10}(\bar{I}_1 - 3) + \frac{1}{D_1}(J^{el} - 1)^2$$

(2.14)

where C_{10} and D_1 are temperature-dependent material parameters, $\bar{I}_1$ is the first deviatoric strain invariants; J^{el} is the elastic volume ratio.

2.6.5 Ogden form models

Another commonly used model is the Ogden model (*Ogden, 1972*). Unlike the Mooney-Rivlin model *U is not defined* as a function of I_1 and I_2, but instead the model is based on an assumption that U is a function of the principal values b_1, b_2, b_3 of B.

$$U = \Sigma_n \binom{\mu_n}{\alpha_n}\left(b_1^{\alpha_n} + b_2^{\alpha_n} + b_3^{\alpha_n} - 3\right) \tag{2.15}$$

where μ_n and α_n are constants, and the α_n is not necessarily an integer and may be positive or negative. B is left Cauchy-Green strain tensor. b_1, b_2, b_3 are principal values of B. The general form of the Ogden strain energy potential is

$$U = \sum_{i=1}^{N} \frac{2\mu i}{\alpha_i^2} (\bar{\lambda}_1^{a_i} + \bar{\lambda}_2^{a_i} + \bar{\lambda}_3^{a_i} - 3) + \sum_{i=1}^{N} \frac{1}{D_I} (J^{el} - 1)^{2i} \tag{2.16}$$

where $\bar{\lambda}_i$ are the deviatoric principle stretches; λ_i are the principal stretches; N is the order of the polynomial; μ_i, α_i and D_i are temperature-dependent material parameters (*ABAQUS Manual 6.14*).

$$\mu_0 = \sum_{i=1}^{N} \mu_i \ , \qquad\qquad K_0 = \frac{2}{D_1} \tag{2.17}$$

Following this form, the Mooney-Rivlin form can also be obtained from the general Ogden strain energy potential for special choices μ_i, α_i.

2.6.6 Models for compressible material

In practice, all rubbers are compressible to a certain extent, however some rubbers such as vulcanized rubber undergo only very small volume changes when subjected to very high hydrostatic pressures, so that for practical purposes it can be regarded as incompressible. For foams this is no longer the case and, motivated by the above considerations, studies have been made on the appropriate forms of W for compressible rubberlike materials *(Ogden, 1972)*.

Equation 2.18 is a typical strain energy function density used for compressible materials

$$U = \frac{1}{2}\mu f \left\{ J_1 - 1 - \frac{1}{v} + \frac{1-2v}{v} J_3^{-2v/(1-2v)} \right\} + \frac{1}{2}\mu(1-f) \left\{ J_2 - 1 - \frac{1}{v} + \frac{1-2v}{v} J_3^{2v/(1-2v)} \right\} \tag{2.18}$$

where μ, f, v are constants, and

$$J_1 = I_1, \qquad J_2 = I_2/I_3, \qquad J_3 = I_3^{1/2} \tag{2.19}$$

When v=0.5 and the material is incompressible so that $I_3 = 1$, the strain energy function reduces to the Mooney-Rivlin form

$$U = \frac{1}{2}\mu f \left\{ I_1 - 3 \right\} + \frac{1}{2}\mu(1-f)\left\{ I_2 - 3 \right\}$$

$$U = C_1(I_1 - 3) + C_2(I_2 - 3) \tag{2.20}$$

In the case of 47% foamed polyurethane rubber, the results of Blatz and Ko (Li 2009) indicate that $f = 0$, $\mu = \dfrac{1}{4}$, in which case

$$U = \frac{1}{2}\mu\{J_2 + 2J_3 - 5\} \tag{2.21}$$

and clearly U is independent of I_1.

By generalising the Ogden model for incompressible materials, a new form of compressible materials was proposed *(Ogden, 1972)*.

$$U = \sum_n (\mu_n/\alpha_n)(b_1^{\alpha_n} + b_2^{\alpha_n} + b_3^{\alpha_n} - 3) + F((b_1 b_2 b_3)) \tag{2.22}$$

in which the compressibility is accounted for by the additive function F of $b_1 b_2 b_3$. In finite element modelling, an improved equation is suggested known as the elastomeric foam material model (*ABAQUS Theory Manual 2017*).

$$U = \sum_{i=1}^{N} \frac{2\mu_i}{\alpha_i^2}\left[\hat{\lambda}_1^{\alpha_i} + \hat{\lambda}_2^{\alpha_i} + \hat{\lambda}_3^{\alpha_i} - 3 + \frac{1}{\beta_i}((J^{el})^{-\alpha_i\beta_i} - 1)\right] \tag{2.23}$$

where N is a material parameter; μ_i, α_i, and β_i are temperature-dependent material parameters;

$$\hat{\lambda}_i = (J^{th})^{-\frac{1}{3}}\lambda_i$$

so, $\quad \hat{\lambda}_1\hat{\lambda}_2\hat{\lambda}_3 = J^{th}\lambda_1\lambda_2\lambda_3 = J^{th}J = J^{el} \tag{2.24}$

and λ_i are the principal stretches. The elastic and thermal volume ratios are , J^{el} and J^{th} respectively.

The coefficients μ_i are related to the initial shear modulus, μ_0, by

$$\mu_0 = \sum_{i=1}^{N} \mu_i \tag{2.25}$$

while the initial bulk modulus, K_0, follows the form

$$K_0 = \sum_{i=1}^{N} 2\mu_i\left(\frac{1}{3} + \beta_i\right) \tag{2.26}$$

For each term in the energy function, the coefficient β_i determines the degree of compressibility, which is related to the Poisson's ratio, ν_i, by the expressions

$$\beta_i = \frac{v_i}{1 - 2v_i} \tag{2.27}$$

Thus, if β_i is the same for all terms, a single effective Poisson's ratio, v_i can be derived. This effective Poisson's ratio is valid for finite values of the logarithmic principal strains (ε_1, ε_2, ε_3) in uniaxial tension ($\varepsilon_2 = \varepsilon_3 = -v\varepsilon_1$). Then the stress-strain relations are defined in terms of the nominal stress (the force divided by the original undeformed area) and the nominal, or engineering, strains, ε_i. The principal stretches, λ_i, are related to the principal nominal strains, ε_i, by

$$\lambda_i = 1 + \varepsilon_i \tag{2.28}$$

The choice of material models often depends on the materials, the loading condition, modelling efficiency and accuracy requirements of the particular application or problem. Figure 2.10 shows some typical testing method of materials. For metal materials, prediction of the key properties such as E values and yield stress, work hardening coefficients is relatively straightforward, through standard (e.g. tensile or compression), in some case through nonstandard tests (e.g. Vickers hardness). In FE modelling, the full stress strain curve can be used as the input. In a situation where fracture is required (such as machining), some fracture parameters are also required. For hyperelastic or hyperfoam parameters, a combination of testing data may be required to model the material under complex loading conditions, in which the FE program uses a set of parameters which give a good overall fit to all the input material data derived through curve fitting.
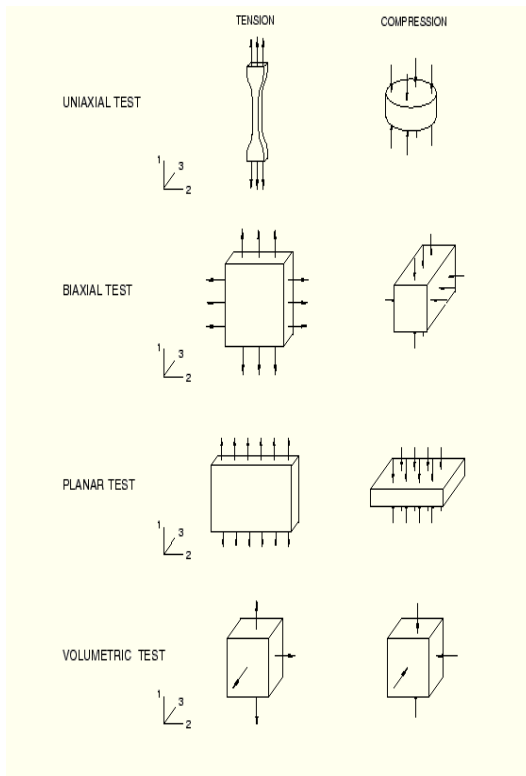
(a) Deformation modes of various experimental tests for defining material parameters (*ABAQUS User Manual 6.14*).

UNIAXIAL TENSION   POSITIVE PRESSURE   EQUIBIAXIAL COMPRESSION

(a)

UNIAXIAL COMPRESSION   NEGATIVE PRESSURE   EQUIBIAXIAL TENSION
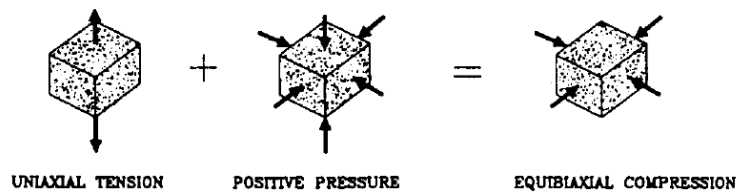
(b)

(b) Equivalence of stress states shown by superposition of hydrostatic pressure (*Charlton, 1993*).

Figure 2.10 Different stress strain conditions and equivalent stress state by combining different testing modes.

2.7 Application and development of Python scripts.

Python is a modern, interpreted, object-oriented, open-source language used in all kinds of software engineering. Among its salient features, Python has a concise but natural syntax for both arrays and non-arrays, making programs exceedingly clear and easy to read; as the saying goes, "Python is executable pseudocode." Also, because the language is interpreted, development is much easier; there is no need to spend extra time manipulating a compiler and linker. In addition, Python code is more robust and less brittle supported by modern data structures and the object-oriented nature of the language. Python's open-source pedigree is a major advantage over other programs, it is becoming increasingly popular and is aided by a large user and developer base in industry as well as the sciences. The open source nature means that developer can take advantage of the tens of thousands of Python packages that exist. These include visualization, numerical libraries, interconnection with compiled and other languages, memory caching, Web services, mobile and desktop graphical user interface programming, and others. There are some disadvantages of Python. For example, pure Python code runs much more slowly than compiled code, and the number of scientific libraries is relatively limited compared to Fortran. There have been concerns that the documentation and support for new science users is relatively sparse, but the situation has changed greatly as the collection of scientific libraries is growing, and science support resources are becoming more robust through sharing. There are tools to overcome the speed penalty in particular in engineering applications (Norbury, 2016).
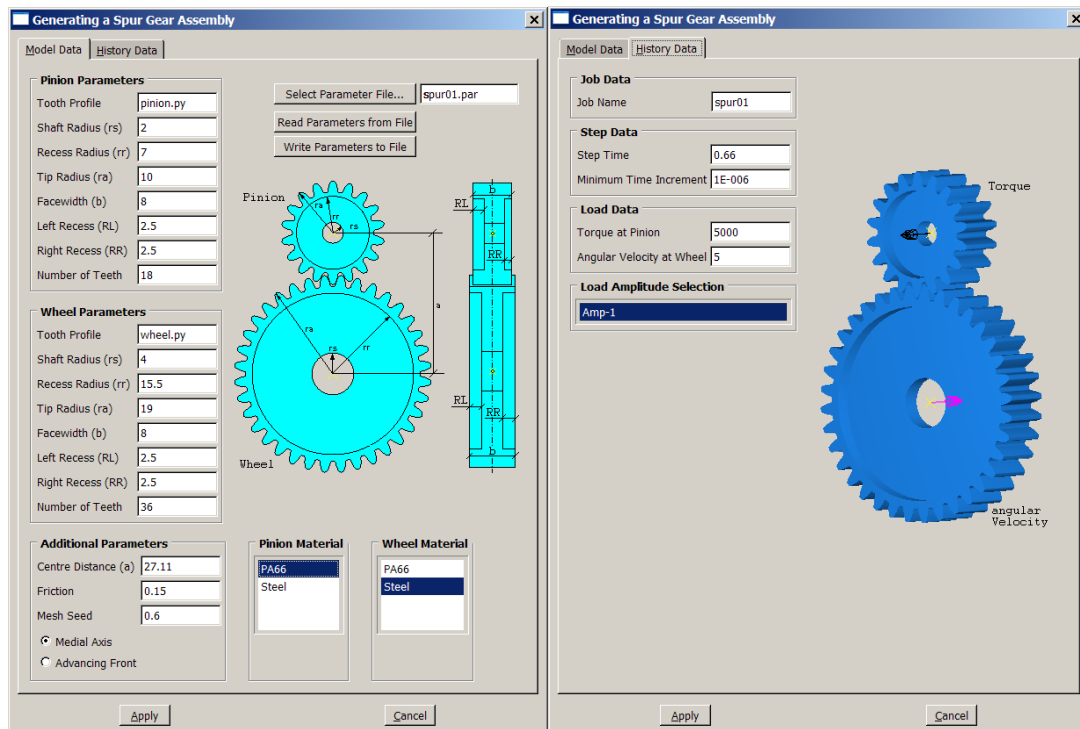
Figure 2.11 ABAQUS CAE Plug-in toolkit, used by Winker, et al (2005) to generate gear models.

For engineering applications, Python is used in conjunction with other engineering software to create a Graphical User Interface (GUI). Creating a GUI via a plug-in will allow the user to input all analysis information in an intuitive way within the familiar simulation software environment. The information from the user which will be obtained by the plug in will automatically configure both the subroutines and the model itself so that an analysis can be performed. Using a single procedure, allowing much of the required data to be input using a simple text file rather than changes to the code itself. This automation removes many of the sources of error possible in previous incarnations of the method, whilst at the same time providing a more convenient and faster way. Finite Element package ABAQUS/CAE has an application called GUI Toolkit. This widget toolkit has been widely used in parametric research studies. Winkler et al (2005) created plug-ins to generate spur and worm gear models as shown in Figure 2.11. This paper reported a method of parametrically modelling spur and worm gears with spur or helical toothing, which took into account assembly deviations such as centre distance error or shaft angle error, and defining standard load cases to be analysed and evaluated using the finite element package ABAQUS. In a recent work (Nesládek and Španiel, 2017), a Python based plug-in (Figure 2.12) which was used to model fatigue of materials has been designed as a plug-in for the Abaqus commercial FE code allowing for fatigue predictions

based on the results of Abaqus FE analyses. It also contains an interface for data transfer between Abaqus and PragTic, a standalone fatigue post-processor. The program contains a simple and intuitive graphical interface, which makes preparation of a fatigue analysis much more straightforward. All these have greatly enhanced the data management between design, material and application related modelling assessment. Python programming is also used in material structure prediction and modelling (Cojocaru and Karlsson 2010, Barrett et al 2018). In the work by Barrett et al (2018) as seen in Figure 2.13, Python is used to develop a procedure consisting of the generation of a synthetic voxel-based microstructure of cuboidal shapes using the software called digital representation environment for the analysis of microstructure in 3D (DREAM.3D) and cutting of the model into a final shape by Boolean operations in Abaqus software, and afterwards generating volume FE mesh for the shaped polycrystalline aggregate using a custom-built toolset. The generation of randomly distributed features can also be done in Matlab and Python following the Voronoi, then import the coordinates into Abaqus to control the embedment/inclusion such as spheres, plate, fibre etc.
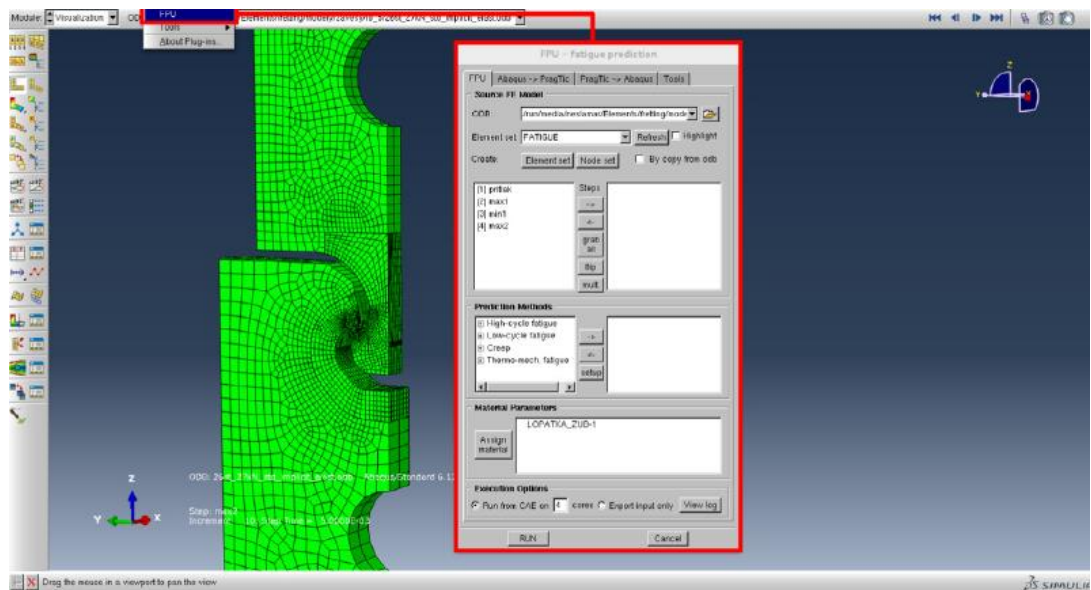
Figure 2.12 An Abaqus plugin for fatigue predictions (Nesládek and Španiel, 2017).
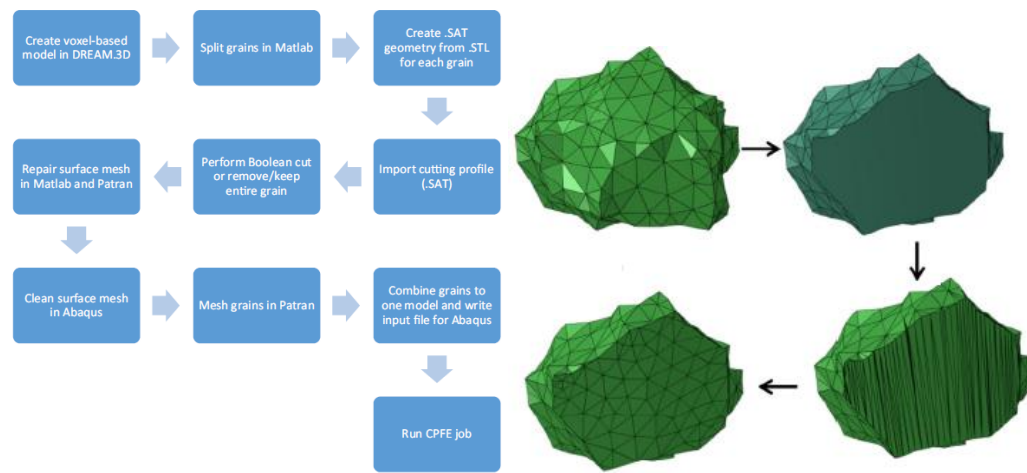
(a)

(b)

Figure 2.13 An automated procedure for geometry creation and finite element mesh generation based on python (a) and typical microstructure generated (b) (Barrett et al 2018).

Python is also increasingly being used in biomechanics (Moore et al, 2014). Python is widely used in further development of biomechanical analysis or software including imaging segmentation, parametric biomechanical model construction and post processing of kinematic and kinetic data. A widely used biomechanical program, Vicon (https://www.vicon.com/downloads/models-and-scripts/python-gait-kinematics) is a typical example, in which a Lower Body Plug-in is used to process kinematic and kinetic data (such as hip movements, knee movements, ankle movements, total hip power, total knee power, total ankle power, pelvic angles, hip angles, knee angles, and ankle angles). Another example of biomechanical data processing is conducting statistical parametric mapping (SPM) analyses on a set of registered 1D curves 'SPM1D' (Pataky 2011), in which Python package is used for conducting SPM analyses on a set of registered 1D curves. Typical applications include kinematics, ground reaction forces and contact

pressure distribution in probabilistic finite element modelling. It also offers a high-level interface to a variety of common statistical tests like 't' tests, regression and ANOVA.

Imaging analysis and model building is important for biomechanics as well as engineering, such building models from 2D scan or developing microstructure based models. Python is also widely used in imaging segmentation (Monari et al, 2014; Cenni et al, 2016, Boppana et al, 2015). Figure 2.14 and Figure 2.15 show a typical example of combining Python based image processing, FE model and user interface. In this work, the risk of bone fracture of astronauts pre-flight and post-flight was analysed using Python based open source imaging segmentation technology. In this study, an open-source computational bone strength model for acceptable performance in the assessment of pre-flight and post-flight astronaut bone strength studies was developed and studied. The Image Segmentation is performed by a Python script which imports CT scans with visualization toolkit (VTK); the library allows for import of many popular medical image formats; then Script translates pixel values to Hounsfield values using metadata in original CT scans and Script isolates bone from medical images with thresholding based on Hounsfield values. The final image is a binary representation of bone regions. The 3D Model Construction operation from 2D images (illustrated in Figure 2.14(c) included • Python's VTK toolkit includes a Marching Cubes algorithm • Creates a 2D surface mesh from binary segmented regions3 • Also smooths mesh and removes unnecessary triangles • Blender4 used to repair mesh and isolate any areas of interest • 2D surface mesh was recreated into a 3D volume mesh with Gmsh5). Also Python script writes material properties to an FEBio XML file for easy import. Figure 2.14 (d) is a Opcat figure illustrating the input and output of Python script. In many human motion analysis software packages, Python interface is always seen in their GUI to do batch process. For example, the software used (OpenSim) also allows the Python program to build a complex human model which is not able to achieve in its GUI. Firstly, to pre-process the data files with points and connectivity into text files formatted so that the AML web-surface-class can use it as input. Secondly, to print the list of subjects that initiates the different bodies and joints. The initiated object needs to consist of property constants that define the objects as position, orientation and reference to local or global reference system. In AML it is practical to have more than two levels in the body hierarchy. Mostly, because of the number of bodies especially in the spine where there are 17 bodies. For this reason the pre-processing of the osim file bodies needed to be printed to the AML file in a way that ensures a tree structure. With this intention the Python dictionary was practical when

storing the structure of the bodies, see Python script below. Figure 2.15 shows the overall structure of the user interface, which combines the imaging and the FE modelling. In the system a GUI combines process of image segmentation and 2D mesh creation into a centralized tool. Then user can select stack of medical images to import and can view stack in three dimensions and can perform image segmentation using their inputted threshold value. Finally, the image can be exported as 2D mesh for next processing step in other software. Such a system based on Python and other programs combining the imaging and FE model could effectively improve the consistency and productivity. It also makes it possible for people who are not experts in finite element modelling to use the system effectively with reduced costs associated with training.

(a) Over structure showing the combined use of python and FE modelling.
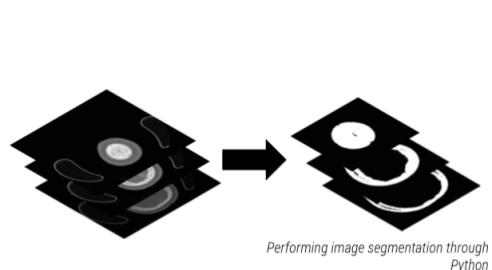
(b)Image showing the image segmentation through python.
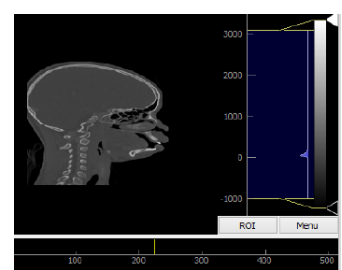
(c) Typical images (Boppana et al, 2015)
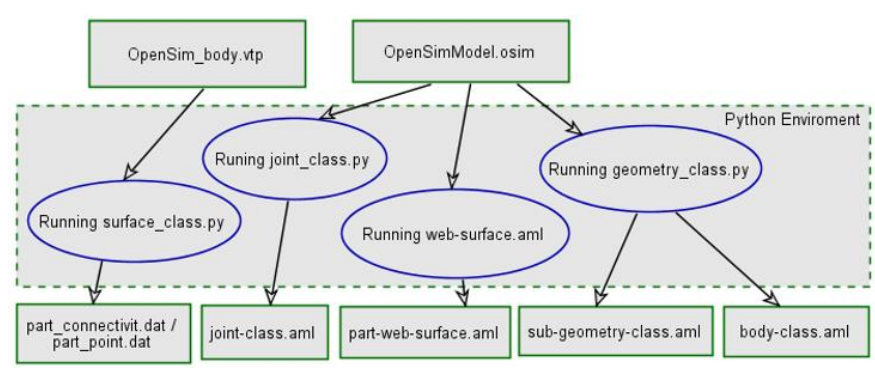
(d) input and output to Python scripts in OpenSim.

Figure 2.14 Use of Python in building FE models.

43
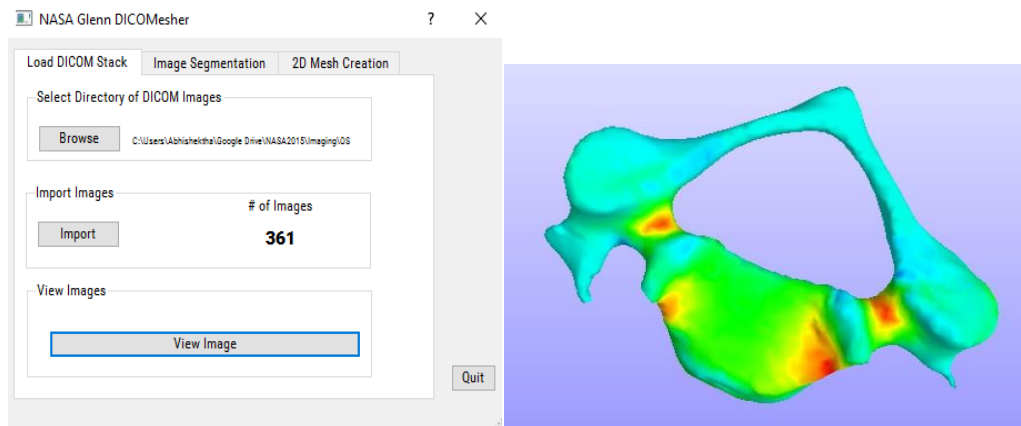
Figure 2.15 In-house interface combining image process and modelling (Boppana et al, 2015)

2.8 Mechanics of embedded system and the effect of Poisson's ratio

Based on the review, the FE modelling and Python program is well suited for processing materials with complex material variation and repeatable structures. As outlined in Chapter one this work focuses on two aspects. One is the indentation of the material systems with embedded layer under indentation tests and potential effects of Poisson's ratios. This greatly improves the efficiency of the process. This potentially can be used to study the deformation of a soft matrix with an embedment and the effect of materials properties (such as Poisson's ratios).

Most of relevant early work on indentation of material systems reinforced with a single stiffer layer has been focused on theoretical work for the understanding of mechanics related to geomechanics and foundation engineering due to the large relative in-plane dimension and thickness ratio of the layers in these material systems (Selvadurai 2009; Rahman et al 2011, Fabrikant 2011; Eskandari et al 2013; Shodja et al 2014; Kalantari et al 2015). Selvadurai (2009) studied the problem of the axisymmetric Boussinesq–Sneddon–Harding indentation problem for an isotropic elastic half space reinforced with an inextensible membrane that is placed at a finite depth from the surface. The work showed the influence of the embedded depth of the embedment and the effect of the Poisson's ratio on indentation resistance of the system. Eskandari et al (2013) studied the lateral translation of an inextensible circular membrane embedded in a transversely isotropic half-space. The study demonstrated that the lateral stiffness of an embedded inextensible circular membrane is highly dependent on the embedment depth and the Poisson's ratio of the matrix. Recently, Shodja *et al* (2014) investigated the indentation process of a transversely isotropic half-space, which is reinforced by a buried

inextensible membrane. The investigation established the effects of anisotropy, embedment depth of the membrane, and material incompressibility on both the contact stress and the normal stiffness factor. All of these studies highlighted the importance of the Poisson' ratio effect and depth of the shell in the mechanical behaviour of a material system with embedded thin stiffer layer under localised loading.

Poisson's ratio is an important material property, which is represented by the negative value of the ratio between the lateral strain and axial strain when the material is being stretched. Most materials have a positive Poisson's ratio due to shrinking in the lateral direction when being pulled for example, metals (e.g. steel, copper, aluminium) have a Poisson's ratio between 0.2-0.3; Ceramics have a Poisson's ratio range 0.1-0.2, while the Poisson's ratio for polymers varies from 0.3 (for engineering plastics) to 0.5 for rubber (representing incompressible, i.e. no volume change when deformed). Poisson's ratio is one of the most important material parameters, which influences the mechanics of materials and many other functional properties (Grima, 2013). A recent development is materials with negative Poisson's ratio, also termed as auxetic materials (Sanmia et al, 2014). Auxetic (negative Poisson's ratio) materials are a new group of materials, with structures that allow lateral expansion when being stretched rather than shrinking as in conventional materials (Gaspar et al., 2005; Sanmia te al 2014). It is well documented that, negative Poisson's ratio influences the material deformation under localised deformation such as indentation (Lakes,1987; Almgren,1985; Wojciechowski,1987). A recent study performed by Argatov et al (2012) investigated indentation and impact compliance of isotropic auxetic materials from the continuum mechanics viewpoint, and the effect of Poisson's ratio and auxeticity was investigated. As shown in Figure 2.16, the Poisson's ratio has a direct effect on the indentation compliance and the stresses during indentation with a flat indenter. In another study on indentation with conical indenters, Photiou et al (2016) illustrated via theory and numerical modelling, that the negative Poisson's ratio has a much stronger influence on the normalised hardness than the positive Poisson's ratio. A typical result is shown in Figure 2.17. The work shows that the Von Mises decreased with Poisson's ratio and the contact pressure is increased with lower Poisson's ratio. In a study on thin membranes with fixed boundary conditions as seen in Figure 2.18 (Aw et al, 2017), which is a situation also relevant to the embedded thin membranes, it is highlighted that negative Poisson's ratios have direct influence on the deformation, the force–displacement curve, the deflection profile and the contact area.
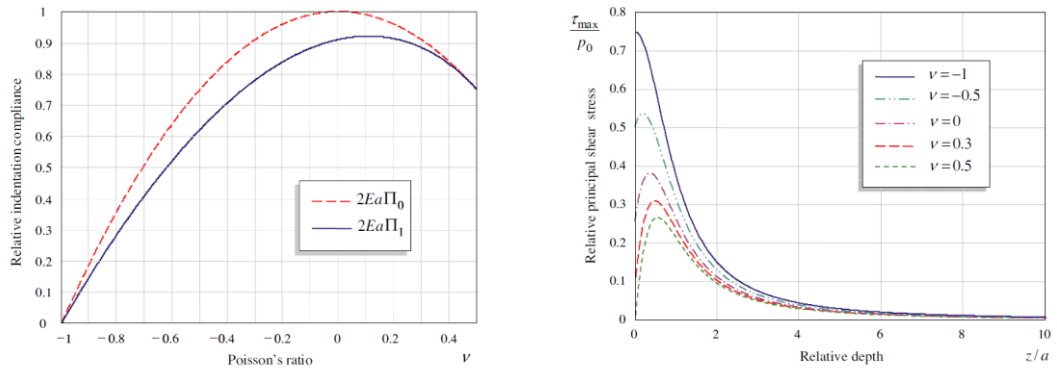
(a) Effect of Poisson's ratio on the relative indentation compliance

(b) Effect of Poisson's ratio on the shear stress

Figure 2.16 Effect of Poisson's ratio on indentation of homogenous materials with flat indenters (Argatov et al, 2012).
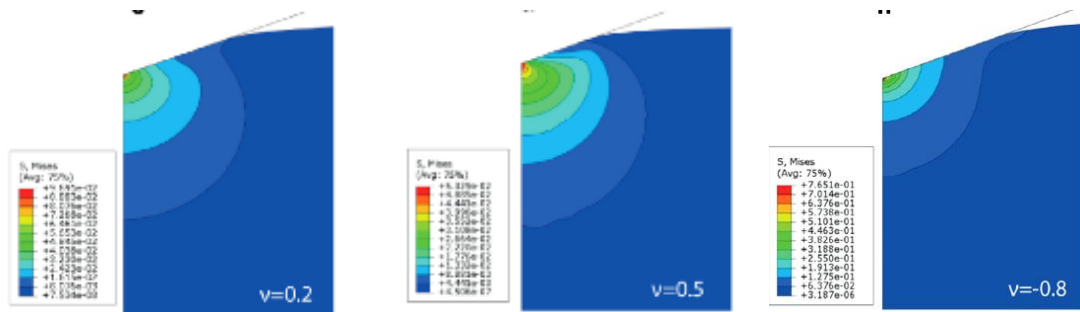
(a) Distribution of von Mises Stress in conical indentation with different Poisson's ratio
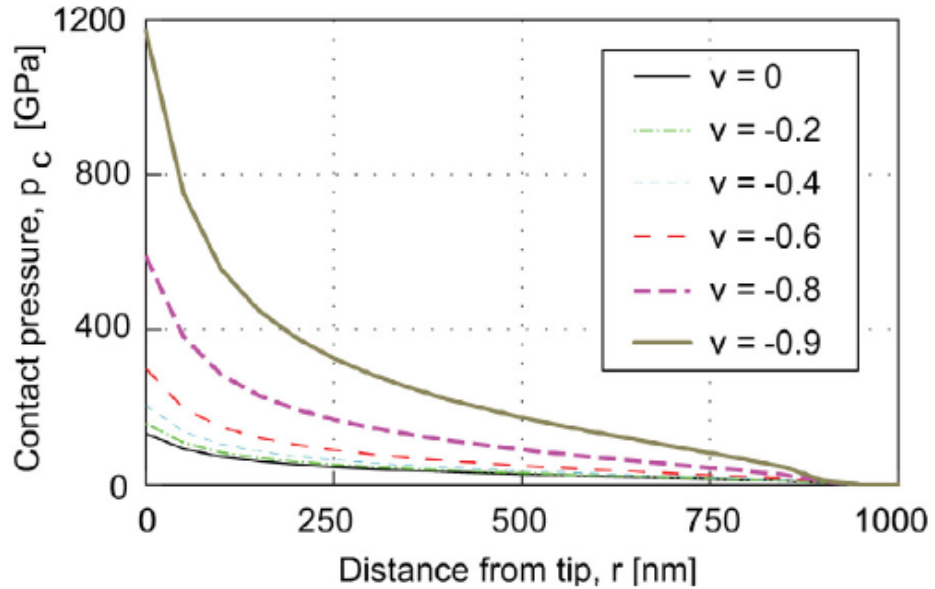
(b) Effect of the Poisson's ratio on the contact pressure

Figure 2.17 Typical results showing the effect Poisson's ratio on the Von-Mises stress-profiles and Contact pressure (Photiou et al, 2016).

(a)
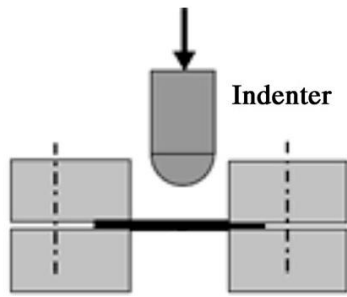
| (a) | Indentation bending of a thin sheet/membrane. | (b) | Typical deformation field. |
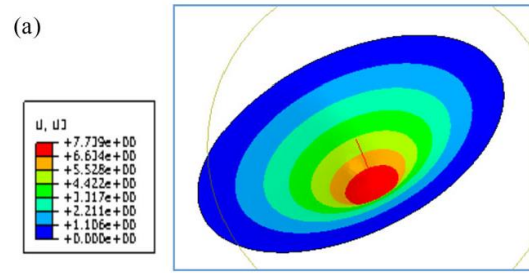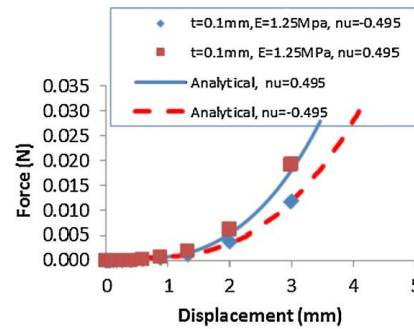
(c)   Comparison between FE and experimental data

Figure 2.18 Effect of auxeticity on the indentation of a thin membrane (Aw et al, 2017).

It should be noted that when a thin membrane/shell is embedded in a matrix, the deformation of the system (matrix and embedment) under localised/pointed deformation (indentation) is much more complex due to the combined interaction from the matrix, the shell properties and the depth of the shell under the indenter. Hence, a systematic investigation is required to investigate the deformation of the material system and factors affecting the indentation resistance/stiffness, which are critical factors for the design and application of such systems as well as developing new material systems.

CHAPTER THREE

EXPERIMENTS AND FE

MODELLING PROGRAMS

3.1 Introduction

This chapter presents the set-up and details of some key experimental facilities and materials. The facilities include testing machines used and the set for compression, tension and indentation tests for different types of samples. The procedure and facilities used to make silicone rubber samples and specimens with a thin shell embedded in silicone rubber are also presented and the procedure explained. The main embedment included piezoelectrical sensor and force sensitive resistors. The set-up for some associated works such as testing on foot prosthetics on rigid supporting surface and EVA foams is also described. The FE modelling package and other programs used in developing the parametric user interface and in evaluating the results are presented.

3.2 Testing facilities

Figure 3.1(a) shows the uniaxial tensile and compression test machine. The uniaxial tensile, compression tests and planar tests were performed on this test machine (model: Tinius Olsen, H50KS). Different load cells (ranged from 20kN to 250N) are available to be selected when performing different tests on different materials. The displacements and the reaction forces were recorded. A laser extensometer and environmental chamber are also available. Specific rigs are available in different types of compression, planar or indentation tests. The machine has been used in tensile tests, compression tests and sheet tests of rubber specimens. It was also used for the indentation tests of silicone rubber specimens with embedded sensor (such as piezoelectrical sensors and force sensitive resistors). In relaxation foam testing, a double load cell set-up (Figure 3.1(b)) is employed to record the change of load with displacement and time. Figure 3.1(c) is a manual hydraulic compression machine used in preliminary works of compression and indentation testing of silicone rubber specimen with embedded sensors with self-made data logging system for resistance measurement for piezo sensors and force sensitive sensor. It is also used to assess the resistance change of conductive rubber and plastic in another project (Kaid, 2018). Figure 3.1(d) shows the Durometer Shore hardness test machine (Hampden Test Equipment Ltd.) and the indenter used for Shore A and Shore OO indenter. In the hardness tests, each sample of the rubber/foam materials was tested at least six times, the final result was calculated by the average values of the tests.

(a) Main test machine for tensile and planar tests.

(b) A double load-cell system for compression relaxation tests and indentation tests.

(c) A manual hydraulic compression testing machine.

(d) Shore hardness tester with Shore A and Shore OO indenters used for checking the properties of rubber and foams.

Figure 3.1 Tensile, compression and hardness tests machines.

3.3 Materials and samples for embedded system.

Figure 3.2 shows the equipment used to cast silicone rubber samples including a vacuum casting machine (a) and an oven (b) used for curing and the mould (c). The vacuum casting machine (Figure 3.2(a)) was used for de-gassing to remove the air from the mixture of the silicone resin and the curing agent. The oven (Figure 3.2(b)) was for the curing process at a temperature of 40°C. Both pieces of equipment were manufactured by MCP Group Ltd. (UK). A wood mould is used to cast silicone rubber samples of different thicknesses after mixing and degassing with or without embedded sensors. The sample shown in Figure 3.2(c) is a sample with a Force Sensitive Resistor (FSR) embedded in a silicone rubber specimen, made by a vertical casting process to control the location of the embedment. The facility was also used to mould some structures with auxetic behaviours, colouring agents and foams with foaming agents.

(a) Vacuum casting machine.

(b) Heating/curing oven.
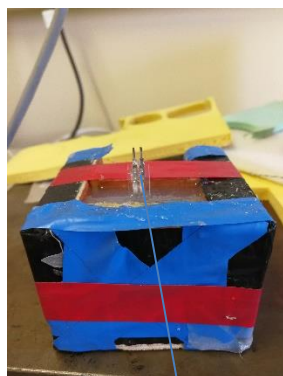
(c) Wooden mould for casting silicone rubber samples with embedded sensors.

Figure 3.2 Equipment and tools used in silicone rubber casting and curing.

Figure 3.3(a) shows the different piezo sensors of different size and thicknesses. The electrical charge of a piezoelectric sensor can be used to detect/measure the changes in pressure, acceleration, temperature, strain, or force by converting them to an electrical charge. The sample has thin copper plate coated with a piezo electrical ceramics coating. Figure 3.3 (b) shows the different types of force sensitive resistors used in different forms and sizes. The sensor has thin plastic material with a mixed structure of plastics and conductive particles. The electrical resistance changes when the material is being pressed due to the change in the contacting path of the particles. The thin copper strip coated on the surface works as the electrode to record the electrical resistance. The circular one shown Figure 3.3 (b) has a closed circuit, the long strip can be cut and maintains a closed circuit, i.e. the resistance can be measured.

Figure 3.4 shows some typical specimens with sensors embedded in silicone rubber. These samples could produce a sample for validating the modelling approaches for simulating material with embedded thin shells. It can also potentially be used for plugs used in shoe soles, in which the silicone rubber will provide protection to the sensor from the external load (compression, bending, or indentation) from the natural movement and external subjects such as curbs, stones, etc. Figure 3.4 (a) are specimens with the piezo sensor embedded at different positions. Figure 3.4(b) are silicone rubber samples with embedded force sensitive sensors. Different shaped samples have been made including flat ended and sphere shaped, which potentially can be used as touching sensors. Figure 3.5 shows the samples with multiple piezo sensors (a) and FSR sensors(b). These are used to assess the pressure and electrical signal change when being loaded. A data logging system can be used to record the signals flexibly depending on the number of sensors used.
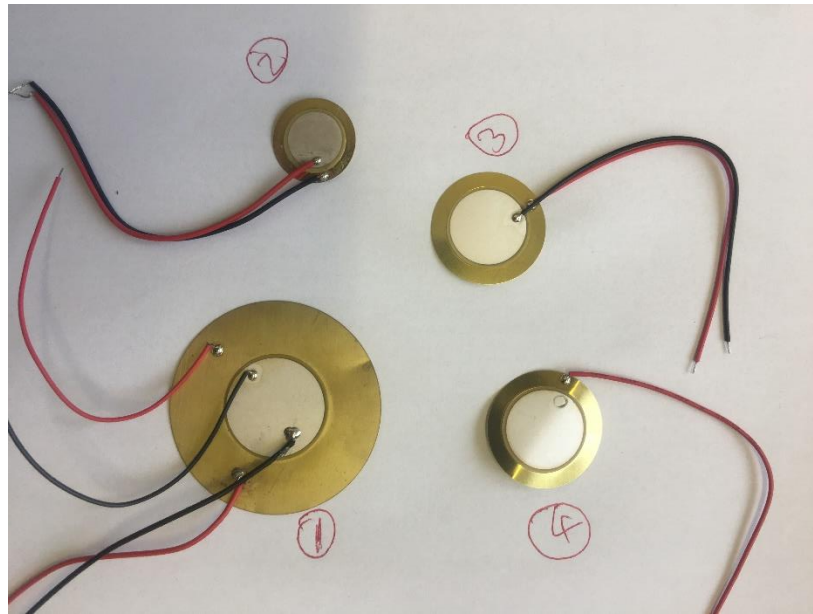
(a) Typical piezoelectrical sensors of different sizes. (Sample#4 is a deformed one)
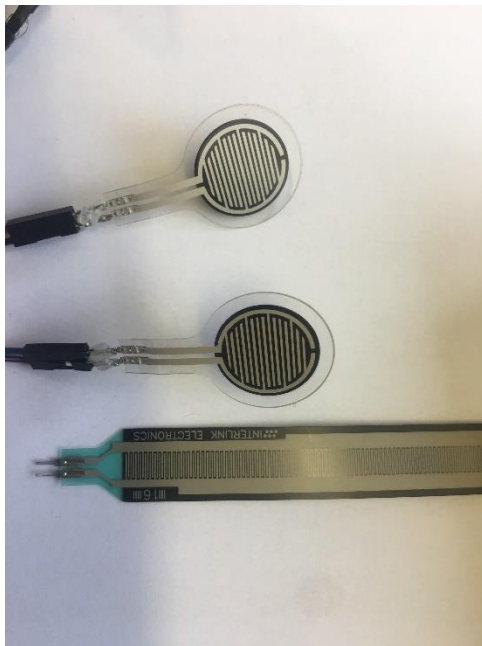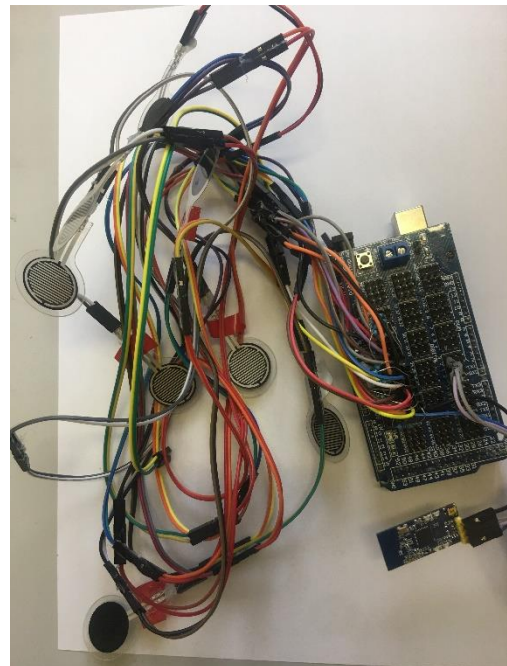
(b) Typical force sensitive resistors. (c) Flexible data logging system

Figure 3.3 Typical sensors (a) Piezoelectrical sensor (b) Force sensitive resistor (FSR), (c) Flexible data logging system.
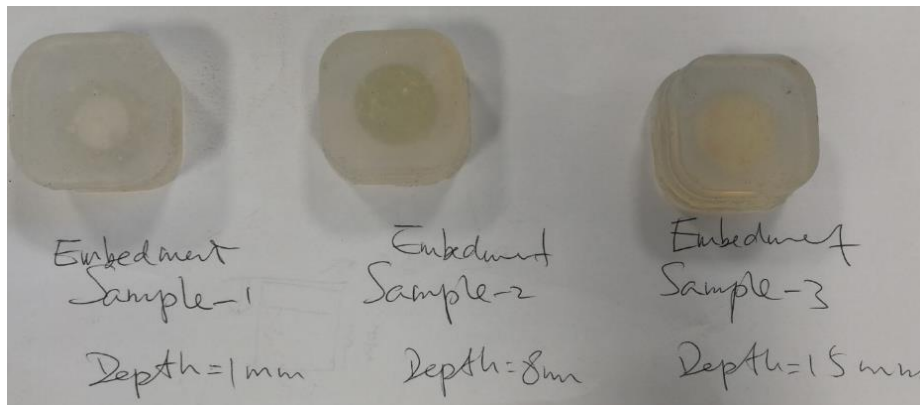
(a)   Sample with a thin pizeosensor embedded in a silicone rubber block at different depths.
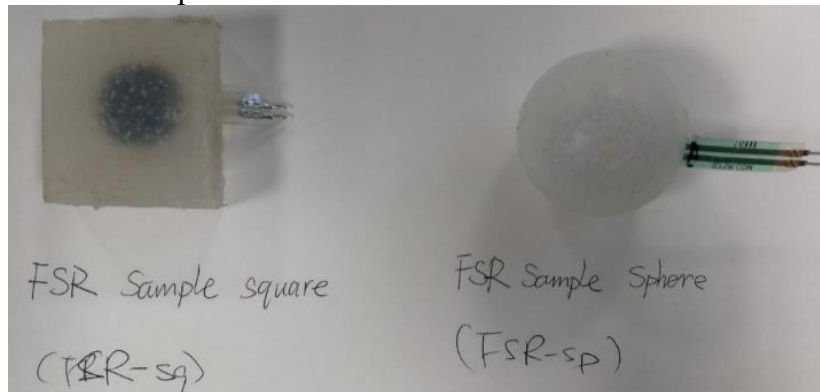
(b)   Typical samples with a force sensitive resistor (FSR) embedded in silicone rubber samples of different shapes (Square and Spherical).

Figure 3.4 Different types of silicone rubber samples with embedded sensors used in the work.
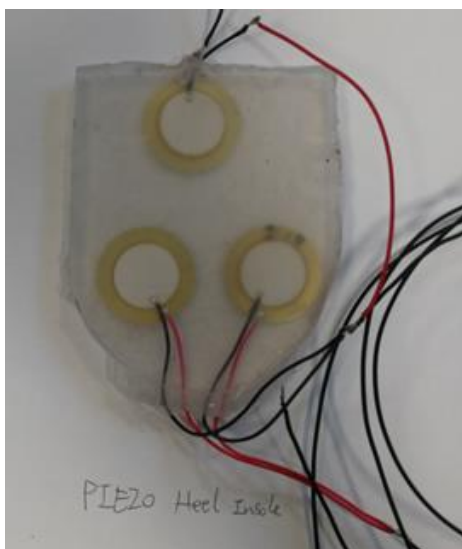
(a) Sample piezo-sensor heel insole   (b) Setup for testing of multiple Force Sensitive Resistor (FSR).

Figure 3.5 Samples with multiple sensors.

3.4 Set-up for different tests

Figure 3.6 shows the set-up of different tests performed in the project and associated works for developing effective FE modelling of different materials and tests. Tensile tests are performed to evaluate the properties of the rubber specimen (Figure 3.6(a)). Some thin sheet has been manufactured and tested using a planar test rig (Figure 3.6(b)). The compression test is used to test silicone rubber with embedded sensors. Figure 3.6(c) is a sample with a piezo sensor embedded in silicone rubber. Figure 3.6(d) is a typical test of force sensitive resistor embedded in a silicone rubber. An in-house designed simple data logging system can be used to record the force detected by the sensor, the channel of which can be flexibly modified depending on the number of sensors. Figure 3.6 (e) shows the set-up of an indentation test of silicone rubber specimen with an embedded piezo sensor. In the test, the indenter is attached to the tensile test machine with an adaptor. Indenters of different shapes (circular flat ended and spherical indenter) and sizes are available to test samples under different boundary conditions. Manual shore hardness is also performed on some rubber as a routine check.

(a)　Typical setup for tensile test of silicone rubber specimen.

(b)　Typical planar test of a thin silicone rubber sheet.
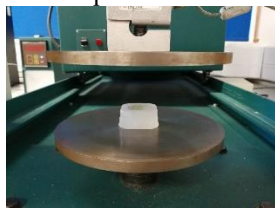
(c)　Compression tests of silicone rubber specimen with an embedded Piezoelectric sensor.
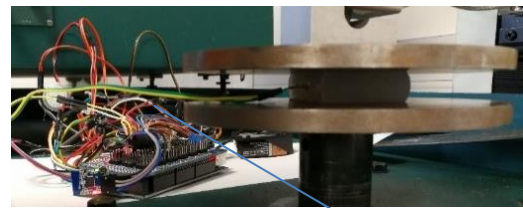
(d)　Compression tests of a force sensitive resistor (FSR) embedded in silicone rubber. A self-designed data logger is used to record the change in electrical resistance.
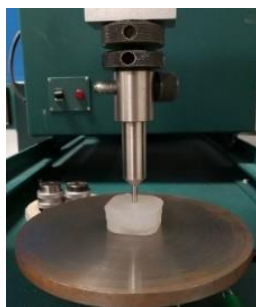
(e)　Indentation tests with flat indenter on a silicone rubber sample with an embedded sensor.

(f)　Shore hardness tests of a rubber sample.

Figure 3.6 Different types of tests.

Figure 3.7 shows some foam samples tested during the course work of the project as part of an industrial project in developing database materials used for foot prosthetics. Typical tests conducted included compression tests and relaxation tests. In the relaxation tests, a simple double load cell arrangement (Figure 3.1 (b)) is used to record the force change with time. Some limited tests were also performed on foot prosthetics, two typical examples are shown in Figure 3.7(b&c). Figure 3.7(b) is a carbon fibre prosthetic, while Figure 3.7(c) is a silicone rubber based foot prosthetic with an embedded internal structure made of wood and steel. Some tests were performed on a rigid (steel) plate, some tests have been performed on EVA foams (Figure 3.7(b&c)) to assess the situation when the prosthetics are inserted in a shoe. These tests are used to provide data for FE model development of the prosthetics, which can help the future development of the FE modelling interface for assessing different prosthetic design under different loading conditions and landing angles.

(a) Typical Foam Materials used.

(b) Compression test of a carbon fibre foot prosthetic on an EVA foam material.

(c) Compression test of a silicone rubber based foot prosthetic with an embedded internal structure.

Figure 3.7 Typical foam materials (a) and testing of foot prosthetics on different foams (b&c).

3.5 FE modelling and other programs

FE modelling and associate programming is the key part of the work, which has been used in studying embedded systems, human foot (bony structure embedded in soft tissues system), sensors embedded in silicone rubber as well foot prosthetics. The FE modelling is performed using ABAQUS (version 6.14). Main numerical works include simulating a thin shell embedded in an elastic matrix to improve the fundamental understanding of the mechanical behaviour and the influence of an embedded system on the indentation resistance of the material system. Python based Abaqus plug-in was developed to process the multiple variables in an embedded system including indenter shape and sizes, depth of the embedment, the properties of the matrix, the properties and the dimensions of the embedded shell. In the FE foot modelling, an Abaqus plug-in is developed with Python to change the orientation of the foot-sole contact and extract the deformation, stress and energy of internal components concerned (e.g. the Metatarsals). The approaches developed were also used in modelling piezo sensors embedded in silicone rubber and foot prosthetics. For development or comparison purposes, several other key features in Abaqus such as Unit cell approach, remeshing has been evaluated. Another CAE software Hyperwork (Altair) is used to increase the proportion of Hexagonal shaped element in the mesh of a human foot model to enhance the modelling efficiency. Other multiscale modelling packages are also evaluated such as DIGIMAT, which is a software specialised in linking structures to larger scale FE modelling. The use of Matlab and Python in generating coordinates for randomly distributed particles or 2-D structures is also evaluated.

CHAPTER FOUR

PARAMETRIC MODELLING OF INDENTATION BEHAVIOUR OF MATERIALS WITH EMBEDDED SHELL IN AN ELASTIC MATRIX

4.1 Introduction

This work presented in this chapter focuses on the modelling and analysis of indentation of soft materials with an embedded stiffer layer focusing on developing a modelling approach and analysing the effect of the properties of the matrix and the embedment. This is of fundamental importance to the understanding of embedded systems. Table 4.1 lists the main work related to modelling and analysis of structures with a thin sheet embedded in a matrix. The first part is the development of FE models with an embedded structure. This is a challenging task as when a thin shell is used, it is difficult to mesh. The model is compared with an analytical solution for homogenous material and an FE model with an embedded sheet with the same stiffness as the matrix ($E_s=E_m$). The second part is to develop an Abaqus user input plug-in and investigate the effect of the depth of the embedment on the indentation resistance. The modelling data is compared to the data from an analytical approach for an inextensible layer in an elastic half space. The effect of the Poisson's ratio of the matrix over positive and negative domains is systematically established. The potential enhancement of the indentation resistance associated with an embedded thin layer and negative Poisson's ratio is quantified and the trend and limit are predicted. The parametric FE model is used to study the effect of materials properties, shell thickness and the deformation of the embedded sheet in the matrix with normal Poisson's ratio and negative Poisson's ratio.

Table 4.1 Main Research Work.

FE modelling of system with embedded shell and validation against analytical solution
• Development of procedure to simulate a layered material system with the embedded shell in ABAQUS • Validation of the FE model by comparing the numerical data with analytical solution for a flat indenter indenting a homogenous material and shell with the same property as the matrix
Development and Evaluation of a Python based Abaqus Plug-in
• Develop an Abaqus User-Input Plug-in to study the effect of embedment depth, etc. (function design, coding and analysis) • Comparison of the numerical prediction against analytical solution for embedded rigid shell in a soft matrix and establish the effects of depth of the embedment • Modelling the effect of shell depth, indenter size, material properties of the matrix including the auxeticity of the matrix

Typical results and discussion
- Comparison between FE modelling data with embedded inextensible shell and analytical solution
- Effect of the matrix Poisson's ratio on the deformation and indentation
- stiffness of embedded systems with different shell depths
- Effect of the properties and dimensions of the embedded layer
- Deformed model and limitation of the analytical equation

Selected case study related to embedded systems and Auxetic structure
- Parametric FE modelling of piezoelectrical sensors and force sensitive resistor embedded in silicone rubber
- Experimental and numerical studies of 2-D auxetic structure and embedded system

Discussion: The effect of material properties and negative Poisson's ratio on the indentation resistance and the deformation mechanism of the system.

4.2 FE model and comparisons with analytical solution

Figure 4.1(a&b) shows the typical procedure of constructing an FE model with a thin shell embedded within a homogenous block. As shown in the Figure 4.1, a thin shell is built, and then embedded in a square block sample. The radius of the indenter is 1 or 2 mm. The sample is at least 10 times the indenter radius to avoid sample size effect. A procedure using constraint type of "Embedded Region" in interaction has been developed to model the thin shell within the "whole model". The indenter is modelled as a rigid body as it is much stiffer than the sample. The embedded layer is modelled by a finite-strain shell element S4R with 5 integration points. The matrix is modelled by C3D8 elements. The procedure used constraint type of "Embedded Region" to model the interaction between the thin layer within the "whole model" (ABAQUS 6.14 Theory Manual). This approach allows the user to insert a structure within a "host" region of the model or within the whole model. The matrix is the host element while the shell elements of the embedment were treated as the embedded elements. A standard Weight factor round off tolerance (1E-06) is used. The thickness of the shell can be modified by assigning different thicknesses in the section module in ABAQUS. During the FE model development stage, a thickness of 0.1mm is used in the results reported in this work. With this procedure, the position and thickness of the shell can be modified within the system without the need for changing the meshing of the matrix. Using such an approach, the model can be modified flexibly to simulate indentation tests of different conditions/situations, such as shell thickness and position of the shell from the surface. The orientation or angle to the sample surface can also be assessed.

| (a) Thin shell | (b)Material system with an embedded stiffer layer in a homogenous matrix. |

| (c) Typical FE model/mesh. | (d) Deformation field. |
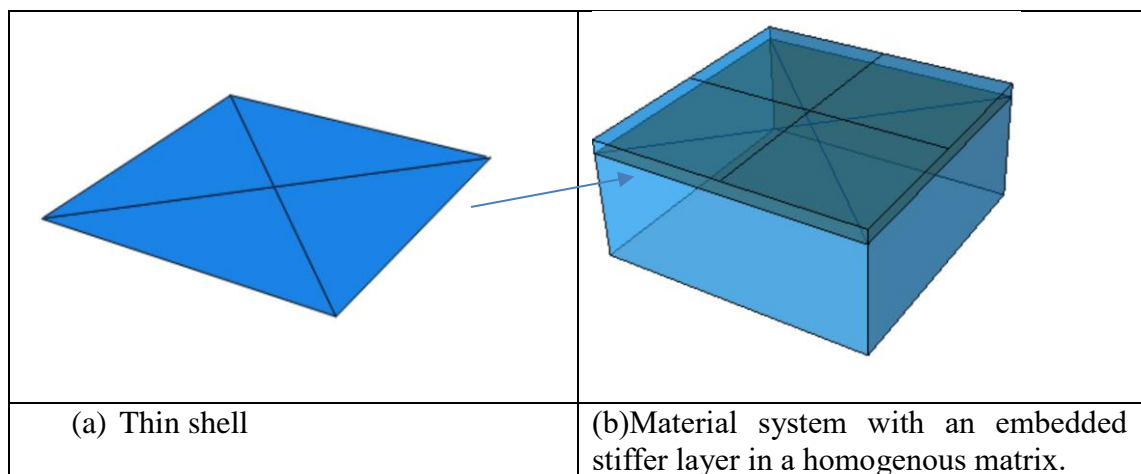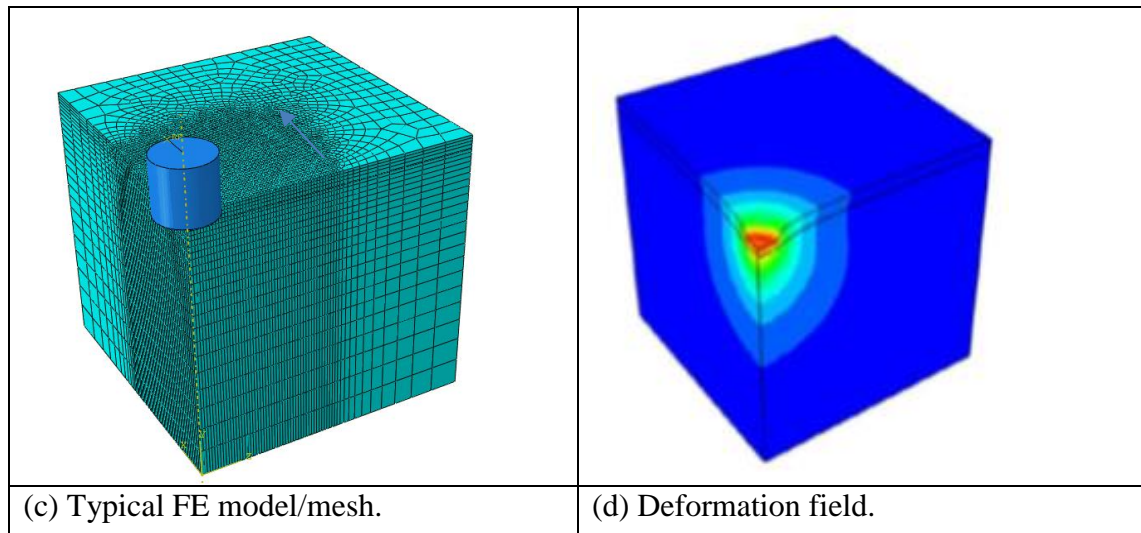
Figure 4.1 FE model of a soft material system with an embedded shell.

The boundary conditions and loading conditions: The flat-ended cylindrical indenter is modelled as a rigid material with a radius of 1mm. The bottom surface of the sample is fixed in all degrees of freedom (DOFs). A fixed displacement is applied on the indenter to move it onto the sample. As shown in the model, the top surface of the sample and the shell is partitioned into four regions to facilitate the assigning of the element and ensure that there is no lateral movement of the indenter from the central points. Mesh sensitive tests have been performed by changing the element size in the model until there is no significant change of the modelling results (force within 5%) with mesh sizes. In the model presented, the matrix is modelled with 32500 (element type: C3D8R) elements and the embedded shell is modelled with 1845 shell elements.

In this work two numerical conditions have been studied to establish the validity of the model. The first model (designated as homogenous model) is a model with no thin shell embedded, this allows a direct comparison between the numerical results and a known analytical solution for indentation of an elastic half space with a circular flat indenter. The second model (designated as inextensible shell model) consists of a sample with an embedded shell, which is much stiffer than the matrix (in this case, $E_s=10E_m$).

Figure 4.2 shows a typical data comparing the results from two modelling conditions against the analytical data based on the equation for a homogeneous sample (eq. 1). One FE data is for the model without an embedded shell, and the other FE data is for the sample with an embedded shell, in which the shell has the same material properties as the matrix. In both cases, the two FE data (one is with shell and one is without embedded shell) are in good agreement with the analytical solution (eq. 4.1) for flat-ended

cylindrical indentation on a homogeneous material (Sneddon, 1965):

$$P_0 = \frac{2bE\Delta}{(1-v^2)} \qquad\qquad (4.1)$$

Where P_0 is the load on the indenter, b is the radius of the cylindrical indenter; E is the Young's Modulus of the matrix. v is the Poisson's ratio of the matrix. Δ is the displacement of the indenter. For the data presented in Figure 4.2, the Young's Modulus used is 3MPa, and the Poisson's ratio is 0.3. A similar level of agreement could be found in other material properties or shell depth combinations. The close agreement between the homogenous model and the FE model with embedded shell of the same material property, shows that the modelling approach using an "Embedded Region" in the interaction module is sufficiently accurate. In the preliminary investigation, a full solid model has been developed in which the shell is modelled by solid elements, and the results are similar (within 5%) but a very fine mesh is required due to the large ratio of the in-plane and out-of-plane dimension of the embedded layers, which causes a much higher demand on the computational resource and time than the "embedded region" approach. In all cases, the force and displacement follow a linear relationship. The force-displacement ratio (P/Δ) will be used to represent the indentation stiffness.
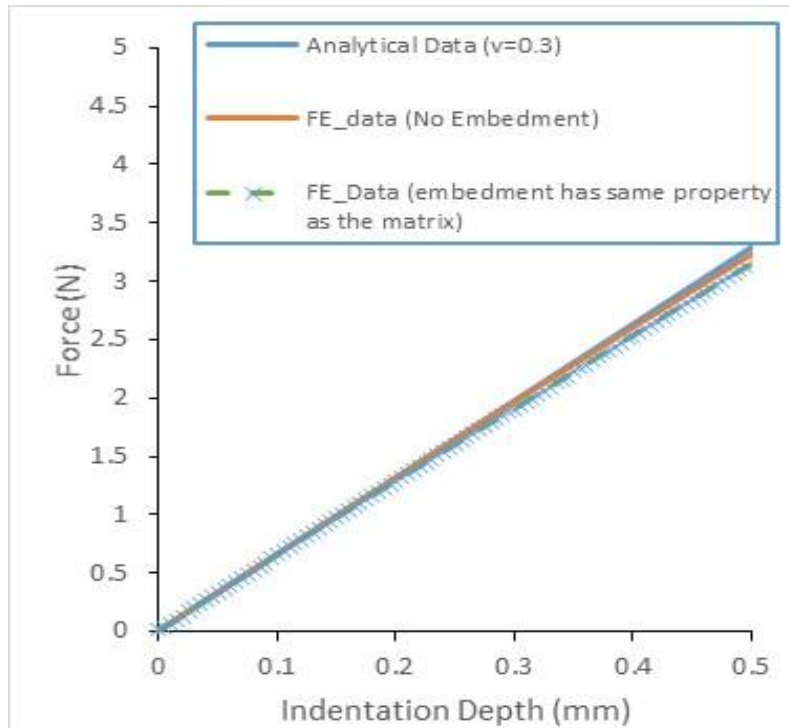
Figure 4.2 Comparison between FE indentation force-displacement data for a homogeneous matrix (i.e. no embedment) and an FE model with an embedded layer having the same properties as the matrix against analytical data for indentation of a homogenous sample with a cylindrical indenter.

4.3 Development of Python based Abaqus plug-in to systematically study the effect of shell depth and Poisson's ratio of the matrix on the indentation resistance

Figure 4.3 shows the main factors considered when designing the user interface for modelling indentation of an embedded shell within an elastic matrix. The structure/main functions of the plug-in I are shown in Figure 4.4. One feature of the user interface is the selection of indenter shape (this work is focused on flat ended indenter); the Python code for selecting the indenter shape is illustrated in Table 4.2. This is achieved by judgement statement (if else) via parameters of 'yesnoSph' coupling with the choose list from RSG window. If the specific indenter shape was selected from the list of indenter shapes, the corresponding program will be running to build the model. Another key issue is the partition of the embedment and interaction between the matrix and embedment. Partition is needed in thin embedment modelling so that the high quality hex mesh can be applied to achieve a more efficient model.

Table 4.2 Python code for selcting the indneter shapes

```
File  Edit  Format  Run  Options  Window  Help
    height=118.375923156738)
session.viewports['Viewport: 1'].makeCurrent()
session.viewports['Viewport: 1'].maximize()
from caeModules import *
from driverUtils import executeOnCaeStartup
executeOnCaeStartup()
session.viewports['Viewport: 1'].partDisplay.geometryOptions.setValues(
    referenceRepresentation=ON)

def CreatSphericalIndentationEMB(yesnoSph,MatrixL,MatrixH,MatrixD,R,IndenterH,Sp

    if yesnoSph=='Spherical Indenter':
        Mdb()
        s = mdb.models['Model-1'].ConstrainedSketch(name='__profile__',
            sheetSize=200.0)
        g, v, d, c = s.geometry, s.vertices, s.dimensions, s.constraints
        s.setPrimaryObject(option=STANDALONE)
        s.rectangle(point1=(MatrixL, MatrixH), point2=(0.0, 0.0))
        p = mdb.models['Model-1'].Part(name='Part-1', dimensionality=THREE_D,
            type=DEFORMABLE_BODY)
        ...
        ...
        ...

    else:

        Mdb()

        #: A new model database has been created.
        #: The model "Model-1" has been created.
        session.viewports['Viewport: 1'].setValues(displayedObject=None)
        s = mdb.models['Model-1'].ConstrainedSketch(name='__profile__',
            sheetSize=200.0)
        g, v, d, c = s.geometry, s.vertices, s.dimensions, s.constraints
        s.setPrimaryObject(option=STANDALONE)
        s.rectangle(point1=(MatrixL, MatrixH), point2=(0.0, 0.0))
        p = mdb.models['Model-1'].Part(name='Part-1', dimensionality=THREE_D,
            type=DEFORMABLE_BODY)
        p = mdb.models['Model-1'].parts['Part-1']
        p.BaseSolidExtrude(sketch=s, depth=MatrixD )
                                                          Ln: 20  Col: 37
```

One key technical factor is the position and meshing of the embedment. The Python code for this operation is shown in Table 4.3. In this process, the embedded shell is partitioned first, then the element type and size are selected. When the size of the embedment changes, the program will automatically change the size of the elements to maintain the efficiency and accuracy.

Table 4.3 Typical Python code developed to partition the embedment.

```python
a = mdb.models['Model-1'].rootAssembly                ###############BooleanCut
a.InstanceFromBooleanCut(name='Part-Matrix_Cut',
    instanceToBeCut=mdb.models['Model-1'].rootAssembly.instances['Part-Matrix-1'],
    cuttingInstances=(a.instances['Part-CopperPlate-1'], a.instances['Part-PiezoPlate-1']
    originalInstances=SUPPRESS)
#horizontal partition
p = mdb.models['Model-1'].parts['Part-Matrix_Cut']
f = p.faces
faces = f[4:5]
p = mdb.models['Model-1'].parts['Part-Matrix_Cut']
c = p.cells
pickedCells = c[0:1]
f1 = p.faces
p.PartitionCellByExtendFace(extendFace=f1[6], cells=pickedCells)
p = mdb.models['Model-1'].parts['Part-Matrix_Cut']
c = p.cells
pickedCells = c[0:2]
f = p.faces
p.PartitionCellByExtendFace(extendFace=f[15], cells=pickedCells)
p = mdb.models['Model-1'].parts['Part-Matrix_Cut']
c = p.cells
pickedCells = c[1:2]
f1 = p.faces
p.PartitionCellByExtendFace(extendFace=f1[19], cells=pickedCells)
#vertical partition
c = p.cells
pickedCells = c[0:4]
f = p.faces
p.PartitionCellByExtendFace(extendFace=f[22], cells=pickedCells)
p = mdb.models['Model-1'].parts['Part-Matrix_Cut']
c = p.cells
pickedCells = c[0:6]
f1 = p.faces
p.PartitionCellByExtendFace(extendFace=f1[28], cells=pickedCells)
p.generateMesh()
p = mdb.models['Model-1'].parts['Part-Matrix_Cut']
c = p.cells
#pickedCells = c[0:2]+c[4:5]+c[6:7]+c[8:9]
pickedCells = c[7:8] #c[0:2]+c[4:5]
v1, e1, d1 = p.vertices, p.edges, p.datums
p.PartitionCellByPlaneThreePoints(cells=pickedCells, point1=p.InterestingPoint(
    edge=e1[41], rule=MIDDLE), point2=p.InterestingPoint(edge=e1[4],
    rule=CENTER), point3=p.InterestingPoint(edge=e1[22], rule=MIDDLE))
```
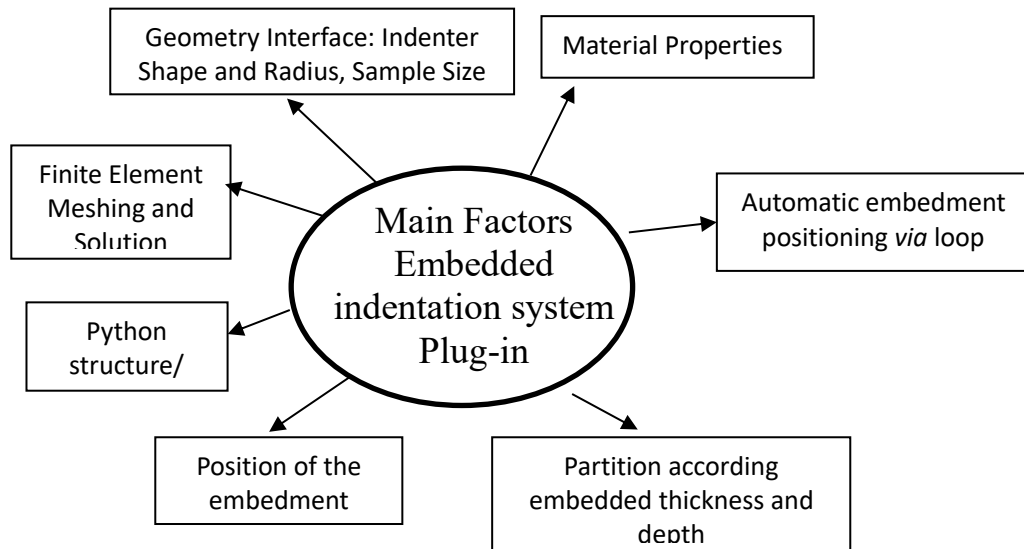

Figure 4.3 Key feature of user interface plug-in for modelling indentation of materials with an embedded layer.
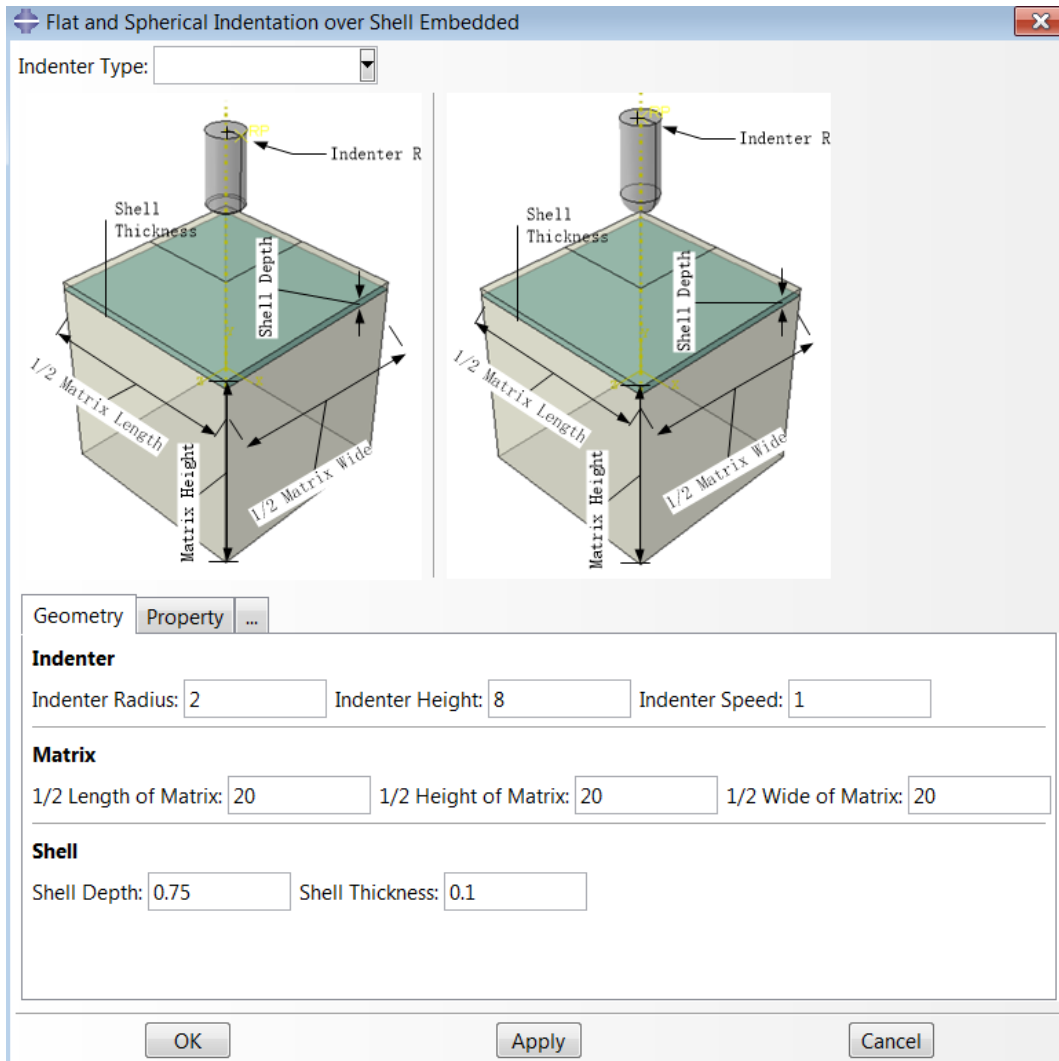
Figure 4.4 Typical Abaqus Plug-in showing the main functions and parameter.

4.4 Typical results and discussion

4.4.1 Comparison between FE modelling data with embedded inextensible shell and analytical solution

Figure 4.5 is a typical set of data from the mathematical approach and the FE modelling (thickness of the embedded layer is 0.1mm, E_m=3MPa; E_s=300 MPa, v_s is 0.3). The indentation stiffness ratio is represented by the ratio between the indentation force for a material with embedment (P) over a material without embedment (P_0, eq. 4.1) (i.e. $\frac{P}{p_0} = \frac{P(1-v)}{4\mu\Delta b}$). Where, Δ is the displacement of the indenter. The shear modulus (μ) is related to the Young's Modulus following $\mu = \frac{E}{2(1+v)}$.

As shown in the Figure 4.5, the value $\frac{P(1-v)}{4\mu\Delta b}$ varies with the depth of the embedment as represented by the ratio of the depth (h) and the indenter radius (both of the analytical results and the FE data show that, when the embedment is closer to the surface (i.e. lower h/b), the indentation stiffness ratio is higher than 1. h is the distance between the midpoint of the shell and top surface of the matrix. When the shell is deeper (i.e. higher h/b), the indentation stiffness ratio is closer to 1, in other words, the embedment has less effect on the indentation resistance. As shown in the figure 4.5, the FE data is in a good agreement with the mathematically determined data (Selvadurai, 2009). The data for v=0.49 is close to full incompressibility (v=0.5) but with a much better computational efficiency. These validation data, together with results for other different properties, indicate that the FE modelling approach is sufficiently accurate for addressing the problem.
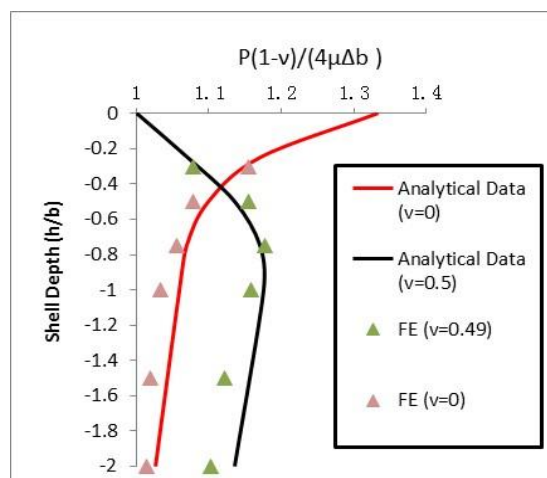
Figure 4.5 Comparison between numerical and analytical data for the Indentation stiffness ratio (Sample with embedment vs. Sample without embedment) with different Poisson's ratios of the matrix.

4.4.2 Effect of the matrix Poisson's ratio on the deformation and indentation stiffness of embedded systems with different shell depths

Figures 4.6&4.7 illustrate the predicted FE indentation stiffness ratio for materials with different layer embedment depth (h) and matrix Poisson's ratios. The data in Figure 4.6 is for an indenter radius of 1mm, while the data in Figure 4.7 is for an indenter radius of 2mm. The change of the indenter size naturally generates different relative depths (h/b). The thickness of the shell for the data presented is 0.1mm.
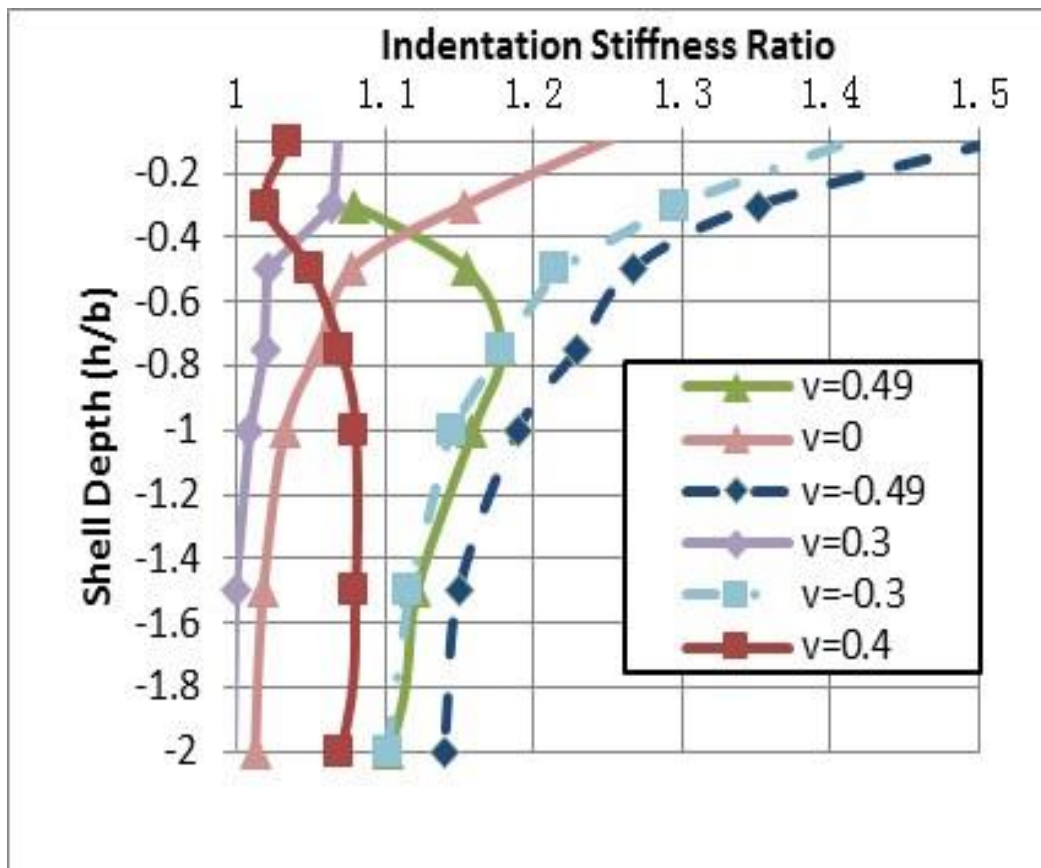
Figure 4.6 Numerical data showing the indentation stiffness ratio over different shell depth (represented by h/b) for different matrix Poisson's ratio. (shell thickness=0.1mm, E_s=300MPa, E_m=3MPa.

As shown by the data in Figure 4.6, the change of indentation stiffness ratio with the embedment depth follows a similar trend for Poisson's ratio of 0 and 0.3 (representing conditions where the material is compressible). When the shell is close to the top sample surface (h=0), the indentation stiffness ratio shows the maximum value, representing more significant effects of the stiffer layer on the indentation resistance, which is reasonable. By increasing the shell depth, the indentation stiffness ratio reduces and

eventually becomes less significant. In the cases with the Poisson's ratio being 0.4 or 0.5 (representing conditions where the material is less compressible or close to incompressible), the relationship between indentation stiffness with the layer depth exhibits a different trend. For Poisson ratio of 0.4, the indentation stiffness ratio reaches a value close to 1, at the surface (h/b close to 0), with a slight increase observed when the shell is immediately underneath the surface. When the material is incompressible (v_m=0.5), the indentation stiffness ratio becomes close to 1, then increases with the layer depth and reaches a peak value when h/b is about 0.75. As shown in the curves for v_m=-0.3 and v_m =-0.49, the indentation stiffness ratio increased further from the data for Poisson's ratio of 0. As shown by the dotted lines in the figure, when the Poisson's ratio is negative, the indentation stiffness ratio continues to increase as the Poisson's ratio changes from 0 to a progressively more negative value. The increase of the indentation stiffness could be over 30% when the layer is very close to the surface. The presented data clearly reveals that the auxeticity of the matrix has a direct influence on the indentation resistance change associated with an embedded layer.
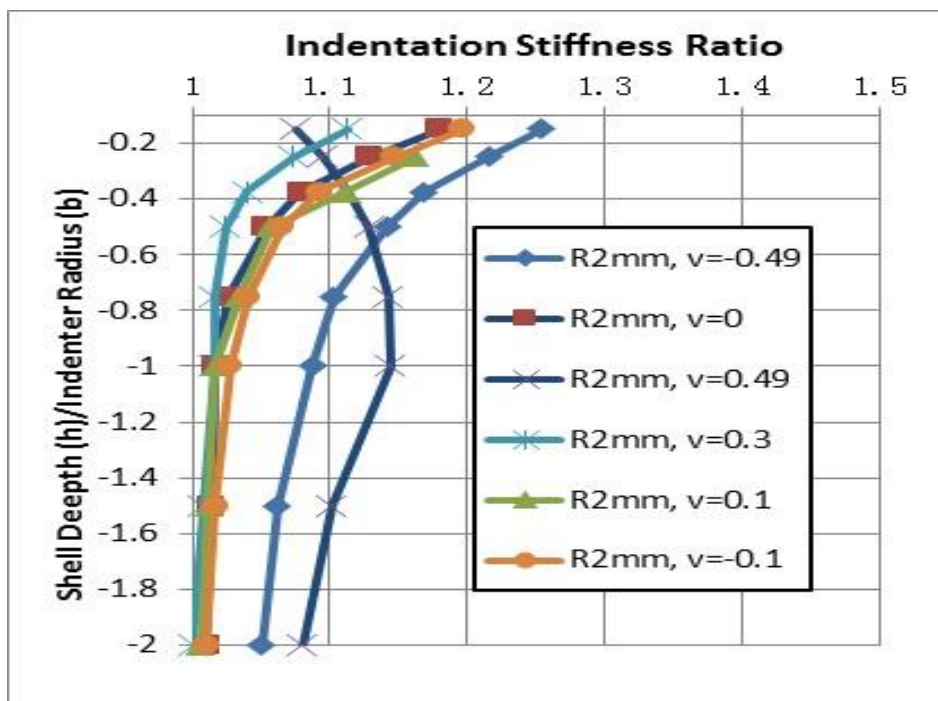
Figure 4.7 Indentation stiffness ratio for a larger indenter size.

Similar data have been obtained for situations with larger indenter sizes. Figure 4.7 shows typical data for an indenter radius of 2mm. The effect of Poisson's ratio of the matrix(v_m) on the relationship between indentation stiffness ratio and layer depth is similar to that for indenter radius of 1mm, but the indentation stiffness ratio is slightly lower. This confirms that the negative Poisson's ratio of the matrix could effectively enhance the

contribution of the embedded layer to the indentation resistance of the matrix and embedded layer system, and the magnitude of the effects is strongly influenced by the depth of the buried layer.

4.4.3 Effect of the properties and dimensions of the embedded layer

To investigate the effect of changing the properties of the embedment on the indentation stiffness, the Poisson's ratio, the stiffness and thickness of the embedded layer were varied systematically. It is essential to assess the effect of the Poisson's ratio of the layer, as potentially the effect of the auxeticity may be associated with the mismatch of the Poisson's ratio, which has been observed in other systems, such as semi-auxetic laminates or composites using a combination of materials with positive and negative Poisson's ratio (Jopek and Strek, 2016; Strek et al, 2016). As shown in Figure 4.8, when the Poisson's ratio of the embedment changes, the indentation stiffness ratios of the materials show very limited change for a sample with a thin shell (0.1mm thickness). A similar trend is observed with other settings of different layer depths. This suggests that the enhanced indentation stiffness ratio with a matrix of a negative Poisson's ratio is unlikely to be due to mismatch of the Poisson's ratio between the embedded layer and the matrix.
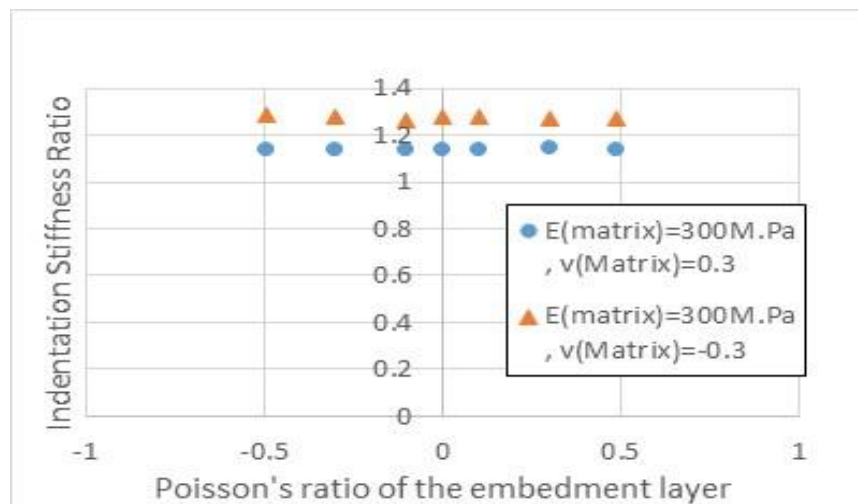
Figure 4.8 Effect of the Poisson's ratio of the embedment (v_m).

Figure 4.9 illustrates typical data regarding the effect of the stiffness of the embedment on the indentation stiffness ratio when the layer (0.1mm in thick) is positioned at a depth of 0.5mm. The stiffness of the embedment is varied from 3MPa to 3000MPa, representing a normalised stiffness against the matrix (E=3MPa) of 1 to 1000. As shown in the figure, when the layer has the same stiffness as the matrix, the indentation stiffness ratio for positive and negative matrix Poisson's ratio is very close to 1, i.e.

resembling a situation for indenting the matrix only. When the stiffness of the layer increases, the data for the negative Poisson's ratio matrix increases, particularly in the region where E_s/E_m is below 100. Beyond this point, the increase of indentation stiffness roughly follows a linear trend but with a much lower rate in both the positive and negative matrix Poisson's ratio domains. Similar work has been conducted on layers with different Poisson's ratios for both stiff shells (E_s/E_m over 1000) and softer shells (E_s/E_m less than 10). The results show no significant difference in the trend of the effect of layer stiffness on the indentation stiffness ratio.
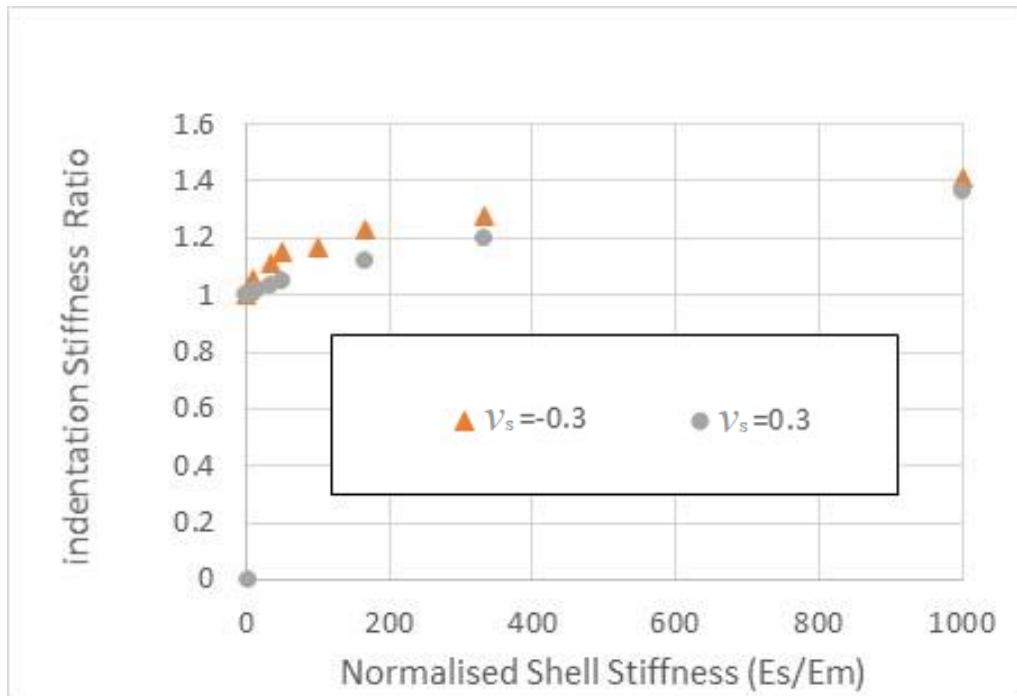
Figure 4.9 Indentation stiffness data showing the effect of the shell stiffness.

Figure 4.10 is a typical set of data (h/b=0.5) showing the effect of the thickness of the embedment on the indentation stiffness ratio. This is another important factor. In real applications, the thickness of the shell could be as thin as 0.01mm to 1mm for different embedded systems (Harmeyer et al 2007; Cannata, M. Maggiali, 2016, Shit and Shah, 2013). This was investigated by systematically varying the thickness of the embedment in the model. For both positive and negative matrix Poisson's ratio, the indentation stiffness of the system increased with the shell thickness. It was noted that there is no major difference in the trend of the indentation stiffness against the layer thickness between situations when the matrix is with a positive or a negative Poisson's ratio.

Figure 4.10 Effect of shell thickness on the indentation stiffness ratio.

4.4.4 Deformed model and limitation of the analytical equation

Soft elastic materials with embedded stiffer layers are becoming increasingly popular in medical and sports engineering fields. The validation and investigated results show that the modelling technique, with the embedded region function, is reliable in investigating the effect of the embedded system with the freedom of changing key dimensional parameters (such as thickness) without altering the meshing elements, etc. The validated results for the homogenous sample and sample with an embedment of the same properties, show a good agreement with data from the analytical solution. The comparison between the indentation stiffness ratios (enhancement parameters) also shows a good agreement with the results based on an analytical approach for situations with different embedment depths. Figure 4.11 shows the indentation stiffness ratio from the analytical solution (Selvadurai, 2009) and the FE data of this work when the stiffer layer is on top of the sample. In general, these two sets of data show a similar trend. When the material is close to incompressible ($v=0.5$), the embedment has limited influence on the indentation resistance. Over the positive Poisson's ratio range, the numerical data match the analytical solution very closely, which further confirms that the FE modelling approach is reasonably accurate. However, over the negative Poisson's ratio range, the FE data is slightly lower than the analytical solution. The exact reason is subject to further studies.

One particular reason might be due to the interaction between the shell and the matrix. The analytical solution assumes full inextensible behaviour for the embedment, this assumption may become not fully valid any more for some conditions. The data presented, from this work, clearly confirm that the matrix auxeticity has a profound effect on the mechanical behaviour of the material system, especially when the shell is on the surface or close to the surface.
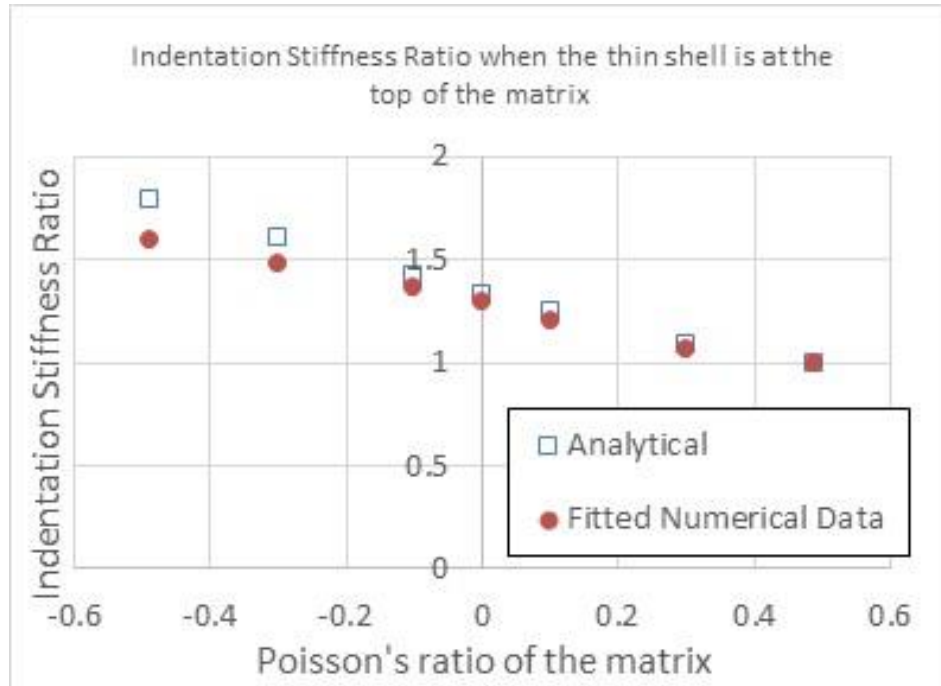
Figure 4.11 Comparison between the indentation stiffness ratio predicted by FE and mathematical approach.

For an embedded shell system, both the embedment and the auxeticity of the matrix influence the indentation resistance. For a flat-ended indenter over small displacement, the effect of negative or positive Poisson's ratio, for a homogenous material, is not very significant. As shown in Equation 4.1, a material with a Poisson's ratio of the same absolute value but opposite sign (negative or positive) would have a similar indentation stiffness. The results in this work clearly suggest that, with the embedment of a thin layer close to the surface, the influence of the auxeticity in the matrix becomes significant as shown in Figures 4.7, 4.8, and 4.9. The reason for this enhanced effect of auxeticity with embedded layer is subject to further study. One potential reason might be the mismatch of the Poisson's ratio, which has been found in auxetic composite (Wojciechowski, 2016; Saxena, 2016). For a composite material, according to Saxena (2016), when positive and negative Poisson's ratio materials are used in a semi-auxetic laminate, both the in-plane and the out of plane stiffness can be increased. However, for the case of indentation on a sample with an embedment layer, the Poisson's ratio of the embedment showed no major influence as illustrated in Figure 4.8. Similar trends have been observed in a range of

different combinations of embedment depth and layer properties. This limited effect of the Poisson's ratio of the embedment on the indentation stiffness ratio is probably due to the fact that under indentation, the lateral deformation of the embedded layer is rather limited due to its high stiffness and possible restraints from the matrix. This suggest that the Poisson's ratio mismatch is not the main reason for the effect of auxeticity on the indentation stiffness increase.

As shown in Figure 4.9, the effect of the stiffness of the embedment on the indentation stiffness ratio follows a different trend over different stiffness ranges. When the embedded layer has a relatively low stiffness value, the indentation resistance increases with layer stiffness more significantly. With higher stiffness values for the embedment layer, a linear relationship is observed between the stiffness of the layer and the indentation stiffness ratio. Similarly, a linear relationship is found between the thickness of embedded layer and the indentation stiffness ratio (Figure 4.10), which is similar to the case for a free standing membrane with fixed boundary conditions (Aw et al, 2015).

Apart from the influence of auxeticity on the indentation resistance ratio, the deformation and stresses of the embedment are also important, as they may influence the function of the embedment. Figure 4.12 compares the displacement fields (a-c) and maximum principal in-plane stresses of the embedded layer (d) between matrix with positive and negative Poisson's ratios. As shown in the Figure, the overall deformation of the embedment (a-c) is similar but there is a difference in the distribution of the maximum in-plane principal stress (d). Figure 4.12(c) plots a detailed profile of the vertical displacement along the radial direction. As shown in the curves, with a negative Poisson's ratio for the matrix, the maximum displacement is slightly less than the displacement with a positive Poisson's ratio, but the region outside the sample-indenter contact area exhibits a higher displacement. This suggests a larger volume of material potentially has been involved in the deformation for the region under the embedment. Figure 4.12(d) plots the profile of in-plane maximum principal stresses along the radial direction for matrix Poisson's ratio of 0.49, -0.49, 0.3 and -0.3. As shown in the curves, for a positive matrix Poisson's ratio, the stress in the section underneath the indenter is predominantly positive, which signifies that the principal direction is outward from the indenter. On the other hand, the maximum in-plane stress in the layer underneath the indenter for the negative Poisson's ratio matrix is negative, implying a strong inward force and the material is being dragged in. This result is consistent with the difference between the auxetic and non-auxetic materials under indentation. For a non-auxetic material, the material tends to be

pushed away, this causes tension radially in the thin layer. For the auxetic material, it tends to draw in towards the indenter causing compression mode of loading on the thin embedded layer. The involvement of the embedment in such a process is likely to increase the effective indentation resistance. Further studies are required to investigate these issues.
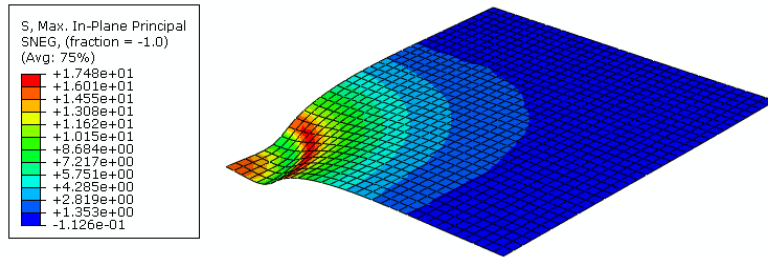
(a) Deformed shape and distribution of the maximum in-plane stress.
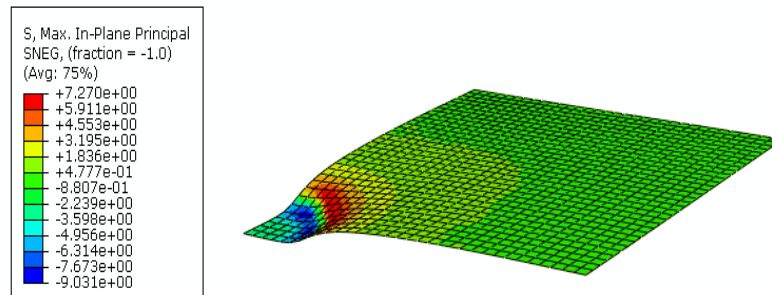
(b) Deformed shape and distribution of the maximum in-plane principal stress.
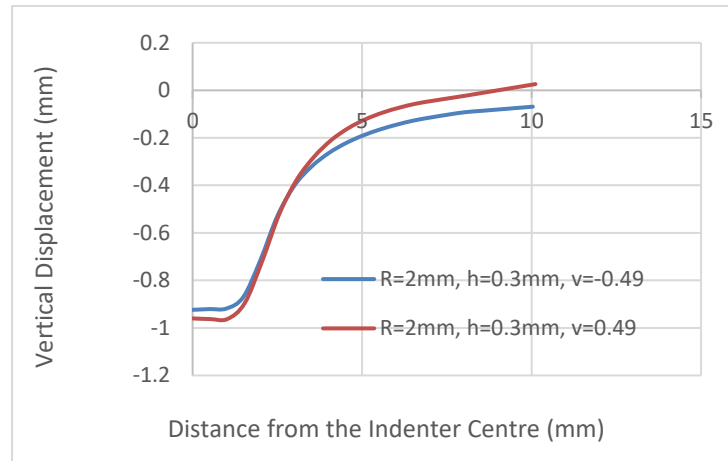
(c) Profile of the vertical displacement of the embedment layer.
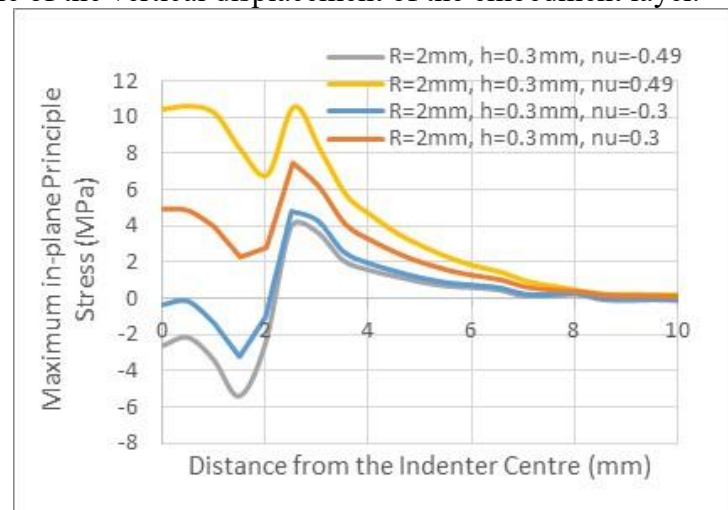
(d) Maximum in-plane principal stress along the radial direction.

Figure 4.12 Comparison of the deformation and the maximum in-plane principal stress of the embedment between materials with a matrix of a positive or negative Poisson's ratio.

4.5 Selected case study related to embedded systems and Auxetic structure

The works presented in this Chapter has focused on the deformation of soft materials with different embedded systems under indentation. The influence of auxeticity on the indentation stiffness ratio and the deformation of the embedded system under different conditions (indenter size, thickness and embedment depth of the embedded layer) was successfully established and key mechanisms of the Poisson's ratio effect are highlighted. This section further presents and discusses briefly some works on materials/systems related to embedded shell and foot mechanics. (1) In the first part, the deformation of silicone rubber sample with embedded piezoelectrical sensors and force sensitive resistor (as typical examples for embedded system) is studied experimentally and numerically. An Abaqus parametric program is developed which is able to simulate the mechanical and electrical behaviours of piezo sensors incorporating the mechanical-electrical properties. The numerical data is compared to published works and experimental data for compression and indentation tests on samples with the piezo sensor embedded in a silicone rubber matrix. (2) Another area addressed and discussed is the analysis and development of 2D meshes (auxetic and nonauxetic structure). The deformation of some typical auxetic and nonauxetic structures was modelled and tested. The potential influence of embedded 2D meshes on the indentation resistance is also discussed.

4.5.1 Parametric FE modelling of piezoelectrical sensors and force sensitive resistor embedded in silicone rubber.

Figure 4.13(a) shows a typical FE model of a piezo sensor beam used to assess the accuracy of the piezoelectrical response, i.e. the voltage generated under fixed unidirectional pressure. The material properties and setup followed the materials and conditions of an online sources (https://www.youtube.com/watch?v=pZfi4SSiypg). The Dielectric (Electrical Permittivity) was set as "$D_{11}=0$, $D_{22}=0$, $D_{33}=1E\text{-}008$"; the Piezoelectric is set as "$d_{31}=2E\text{-}010$", The Young's was set as modulus 'E=100GPa", The Poisson's ratio 'v=0.2. As shown in the Figure 4.13(a), the specimen is fixed at one end, and a uniform pressure is applied at the opposite end. The Element type used is piezoelectric solid element C3D8E. The value of the electric potential (EPOT) is determined by calculating the voltage difference between the opposite surface. A typical results of electrical voltage distribution with an applied pressure of 100MPa is shown in Figure 4.13(b). As shown in the figure, the negative end (in red) is zero, the high voltage

end is in Blue. The pattern of distribution and the value (see the legend) is comparable to published data (Figure 4.13(c). The predicted maximum voltage is 1.385E3V while the published data is 1.429E3V. These value is also in a good agreement with the analytical calculation based on the strain and the piezoelectrical coefficient (Figure 4.13 (d)). This shows that the FE model developed for the piezoelectrical response is sufficiently accurate. This validation makes it easier to simulate the mechanical and electrical response of a real sensor (PZT layer on top of a copper base) under complex condition such as the indentation of an embedded sensor.

Figure 4.13(e) shows an FE model with a piezosensor senor embedded in a silicone rubber matrix, details of the sample and the manufacturing process was presented in Chapter 3. The piezosensor has a PZT (i.e. Lead Zirconate Titanate) coating on a circular copper base. The Young's modulus for the copper used is6GPa, and the Poisson's ratio is 0.2. Table 6.1 shows a typical Python code to calculate the voltage changes. Equation constraint (as seen in Figure 4.13(e)) is used to add the voltages of all the nodes on the top and bottom side of the PZT layer and assign the voltage potential equal to a single node.

Table 6.1 Python code for defining the electrical potential (EPOT)

```
EPTO()

def EquationAvgEPOT():
    a1 = mdb.models['Model-1'].rootAssembly
    v1 = a1.instances['Part-PiezoCopper-1'].vertices
    verts1 = v1[3:4]
    a1.Set(vertices=verts1, name='Set-m_EPOT')
    #: The set 'Set-m_EPOT' has been created (1 vertex).
    a1 = mdb.models['Model-1'].rootAssembly
    f1 = a1.instances['Part-PiezoCopper-1'].faces
    faces1 = f1[7:8]+f1[11:12]
    xv1 = a1.instances['Part-PiezoCopper-1'].vertices
    xVerts1 = xv1[3:4]
    a1.Set(faces=faces1,xVertices=xVerts1, name='Set-s_EPOT')
    #: The set 'Set-s_EPOT' has been created (2 faces).
    mdb.models['Model-1'].Equation(name='Constraint-3', terms=((-1.0, 'Set-s_EPOT',
        9), (1.0, 'Set-m_EPOT', 9)))

    # History output of EPOT
    mdb.models['Model-1'].FieldOutputRequest(name='F-Output-2',
        createStepName='Step-1', variables=('EPOT', 'EPG', 'RCHG', 'CECHG', 'EFLX'),
        region=MODEL, exteriorOnly=OFF, sectionPoints=DEFAULT, rebar=EXCLUDE)
    regionDef=mdb.models['Model-1'].rootAssembly.sets['Set-m_EPOT']      #history Set- load RF2 U2
    mdb.models['Model-1'].HistoryOutputRequest(name='H-Output-EPOT',
        createStepName='Step-1', variables=('EPOT',), region=regionDef,
        sectionPoints=DEFAULT, rebar=EXCLUDE)

EquationAvgEPOT()
```
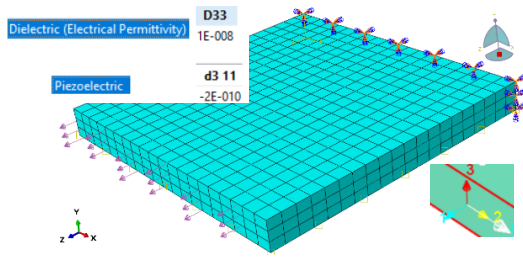
(a) FE model of piezo electrical plate to predict the voltage produced under uniaxial mechanical load.
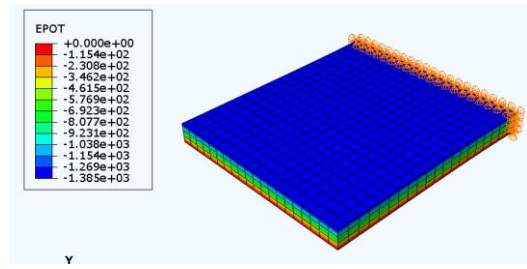
(b) Typical results of voltage, electric potential (EPOT).
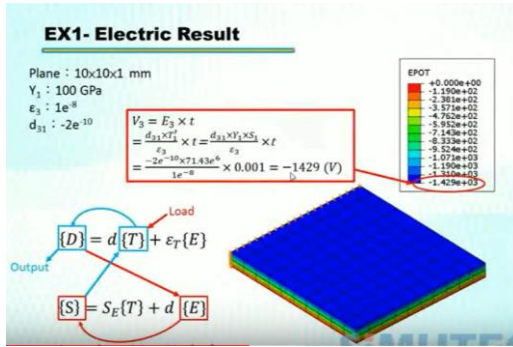
(c) Typical published data on modelling PZT as a source for comparison.
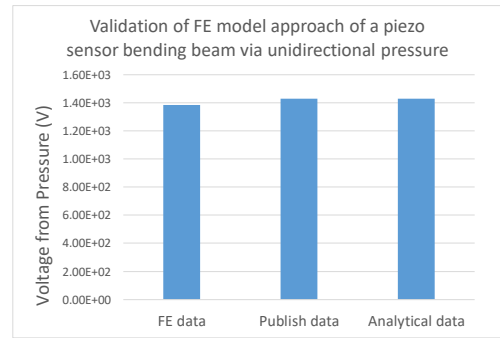
(d) Bar chart comparing the FE, published data and the analytical data.
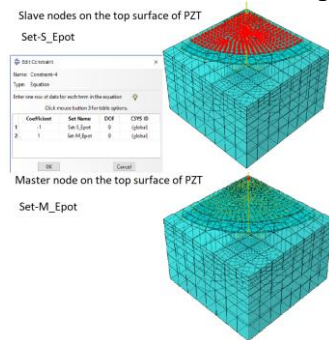
(e) Procedure of Equation Constraint for Degree 9 (EPOT)
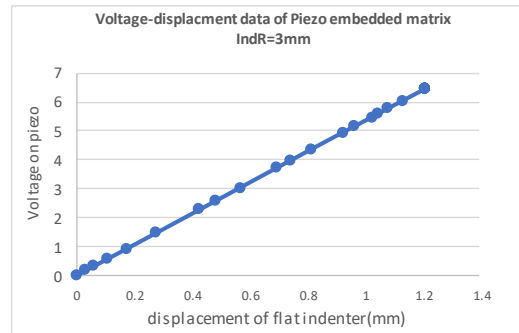
(f) Electrical potential (EPOT) due to indentation
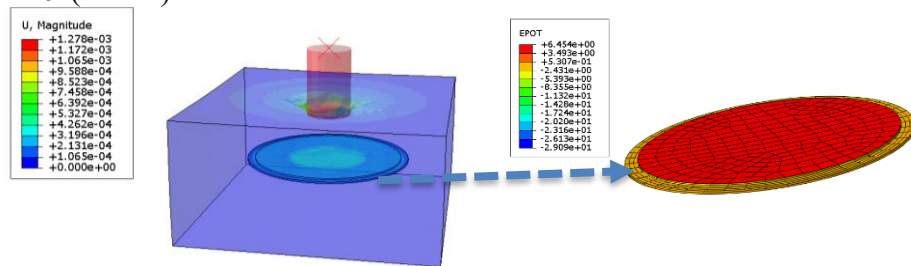
(g) Deformation of sensor embedded in a soft matrix and corresponding EPOT generated on PZT plate

Figure 4.13 FE model of bending and indentation tests of piezo electrical beam with full material properties (copper and PZT) and comparison with published data.

Table 1. shows part of the Python code defining the average voltage on one electrode; further details can be found in Abaqus example manual (7.1.2 Transient dynamic nonlinear response of a piezoelectric transducer). In this model, the top surface is

designated as the Master Surface (with a coefficient of '+1'), the bottom surface is designated as the Slave surface (with a coefficient of '-1'). For convenience, the bottom surface of the piezo sensor is set to be 0 electric potential. The Python program also has a function to output the voltage predefined in history output which can show the whole voltage generated from mechanical deformation. In other words, the equivalent voltage on the master node represents the whole surface voltage like connecting a conducting wire to all the nodes. The conditions for the mechanical modelling approach are similar to the procedure presented and validated in Chapter 4, which is not repeated here to preserve clarity. Figure 4.13(f) shows the voltage vs. indentation depth data, while the voltage of the embedded PZT sensor is shown in Figure 4.13(g)). These results illustrate that the python parametric program has made it feasible to extract the deformation and electricity generation (typical voltage-displacement as seen in Figure 4.13(f)). One potential use of this approach is for modelling program embedded in a real structure such as insole or midsole to predict the sensor sensitivity or electricity generation, which could be addressed in future developments.
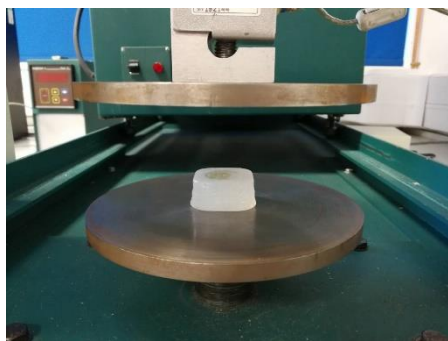
(a) Compression tests of piezo sensor embedded in silicone rubber (unloaded).

(b) Compression test (loaded).
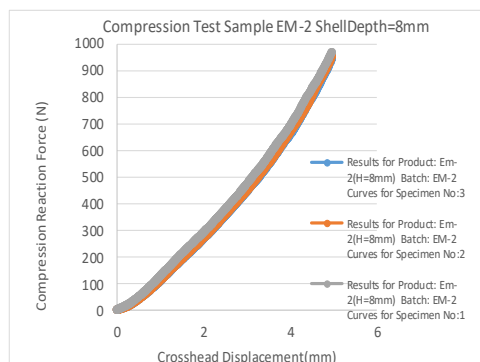
(c) Experimental data (3 tests).
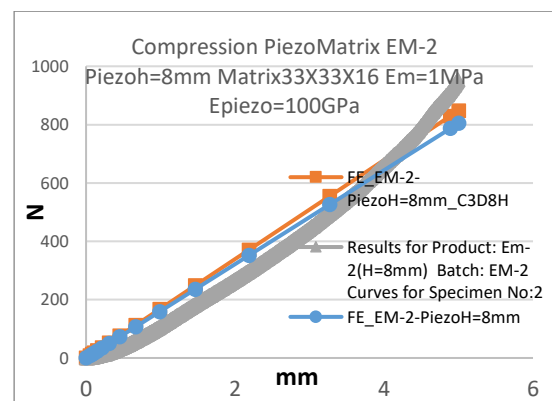
(d) FE vs. Exp. Data.

Figure 4.14 Setup of the tests and typical data showing the comparison between experimental numerical data.

Combined experimental and numerical work has also been conducted to simulate the deformation of embedded piezosensors using silicone rubber as a model matrix material. Typical results are shown in Figure 4.14 and 4.15, for compression and indentation tests respectively. Figure 4.14 shows the experimental setup of compression tests on a silicone rubber sample with an embedded circular piezo sensor. The sample is compressed from one side while the sensor is located at the centre of the sample as illustrated by the schematic diagram.   (a) is the unloaded condition, while Figure 4.14(b) shows the sample under compression between two steel plates. Figure 4.14(c) shows the data from three tests under similar conditions. It can be seen that the data are highly repeatable. Figure 4.14(d) shows comparison between the FE predicted force-displacement data and the experimental data. The two set of data showed a reasonable agreement.
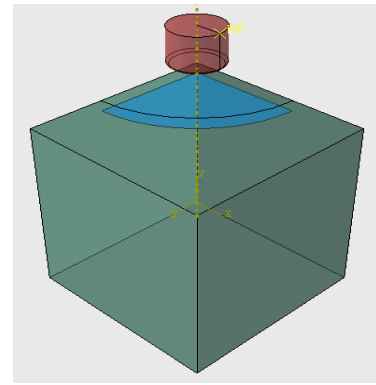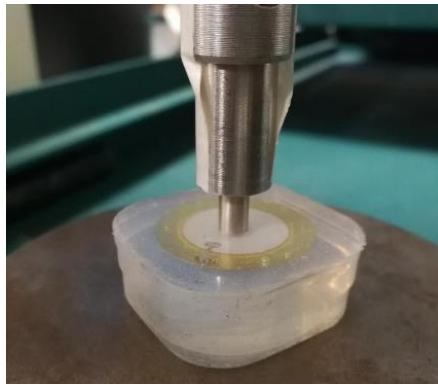
(a)Indentation test of embedded piezo sensor with a cylindrical flat-ended indenter (R=2.5mm)

(b) FE model simulating the indentation tests with a piezo sensor embedded in silicone rubber.
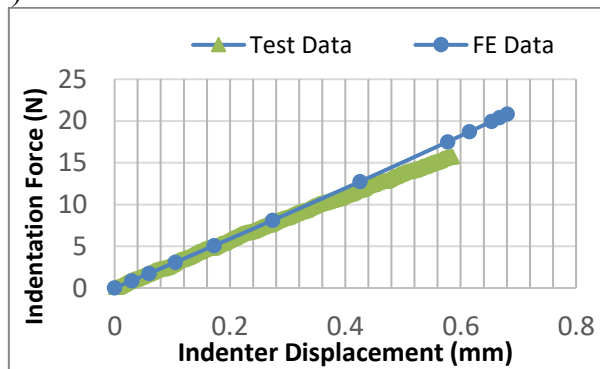
(c) Comparison between FE and testing data of piezo sensor embedded in a silicone rubber matrix

Figure 4.15 Typical test and FE modelling data of indentation tests of embedded piezo sensors with a flat ended indenter.

Figure 4.15 shows the comparison between the indentation tests and FE modelling. Figure 4.15(a) shows the setup of the tests, in which flat indenter is pushed onto the sample. An FE model (Figure 4.15(b)) is developed to simulate the tests following similar

modelling approach as detailed in Chapter 4. Figure 4.15(c) compared the force displacement data; the data showed a reasonable agreement. This shows that the modelling detailed in Chapter 4 on modelling embedded system with embedded region is a practical approach.
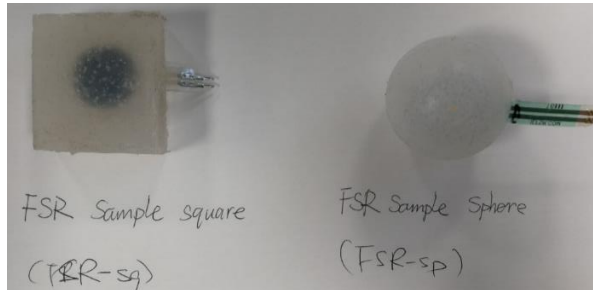
(a) Typical samples with Pressure Sensitive Resistor (PSR) embedded in silicone rubber.
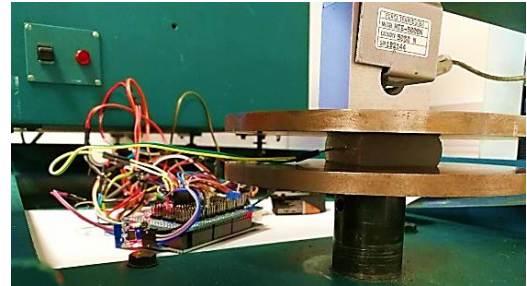
(b) Typical loading condition of compression test of FSR embedded in silicone rubber.
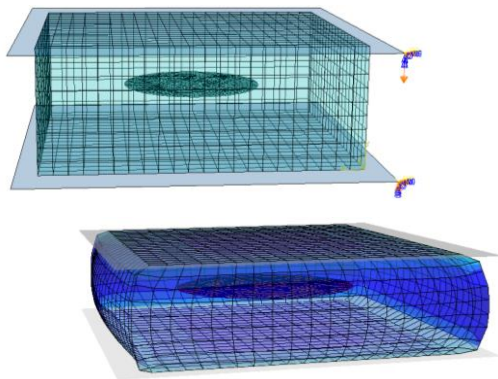
(c) Typical FE Model of compression of FSR embedded in silicone rubber (with mesh)
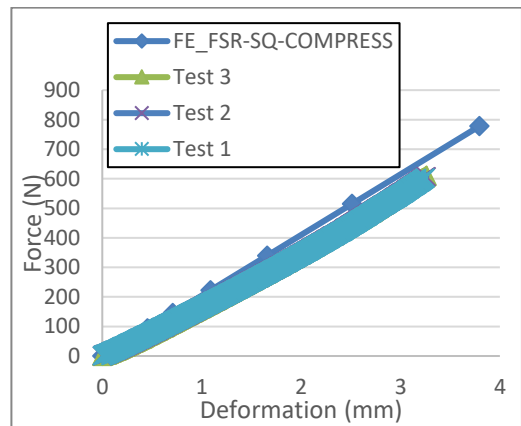
(d) Comparison of experimental and numerical Force-displacement data.

Figure 4.16 Compression test of FSR embedded in silicone rubber.

Similar tests and modelling of embedded force sensitive resistor were also performed as shown in Figure 4.16 (a&b). In the tests, a convenient data logging system is used to monitor the signals of the FSR (force sensitive resistor) and the force is recorded, which is used to assess the FE modelling data. In the FE model, the FSR is embedded in a similar procedure as the one detailed in Chapter 4. A Python program is written to calculate the sum of the force based on the deformation of the FSR. As shown in Figure 4.16(d), the FE model and the test data showed a reasonable agreement. At the linear range, the difference is within 3%. The linear relationship suggests that the embedded sensor can be used for monitoring the force/pressure. The comparison between the FE and experimental

data for compression and indentation tests show that the FE approach is practical and reasonably accurate to model embedded sensors. The matrix can produce protection of the sensor from mechanical or chemical/environmental damage.

4.5.2 Experimental and numerical studies of 2-D auxetic structure and embedded system

From the work presented in Chapter 4, the Poisson's ratio of the matrix has a direct influence on the indentation resistance of an embedded system. Another area requires study are the material behaviour when the embedment is a mesh rather than a continuous shell. In this section, some typical mesh structures with positive and negative Poisson's ratio is studied. Firstly, parametric FE model was developed to simulate the deformation of some typical meshes (as shown in Figures 6.5, 6.6 and 6.7, these structures are based previous works by Gasper and Ren et al (2005)). These are typical low-density structures. All the structures have regular repetitive patterns, for which a Python based parametric program was developed to generate models with different sizes and patterns. The final python program is able to automatically produce FE model of different sample sizes (length of the unit beam, number of cells), dimension of the beam (e.g. thickness, profile), material properties and loading conditions (e.g. applied displacements). This allows a systematic assessment of different structures. Samples were also made of silicone rubber through casting for some selected structures, which are tested to evaluate the numerically predicted Poisson's ratio. Numerical prediction, experimental data and some data from analytical work are briefly presented in the following section.
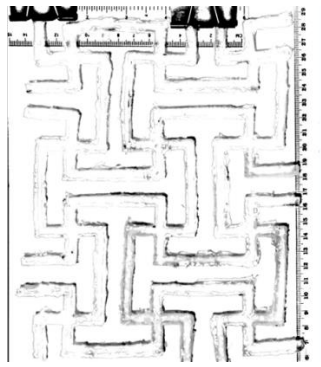
(a) Silicone rubber sample with an auxetic structure (sample-1, Unloaded state).
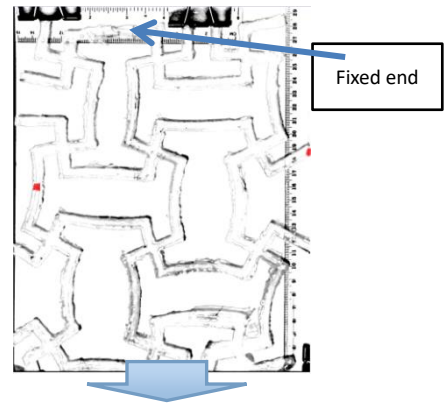
(b) Deformation of an auxetic structure (sample-1, Deformed state).
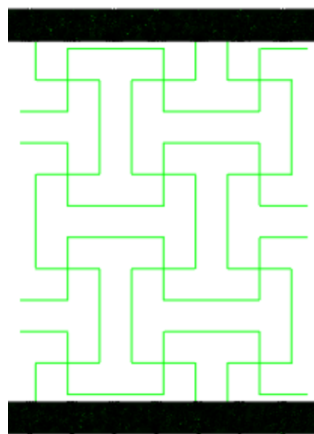
(c) FE model sample-1(Unloaded state).
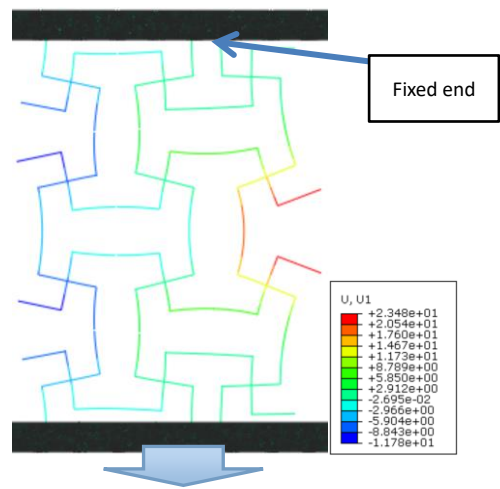
(d) FE model sample-1 (Deformed state).
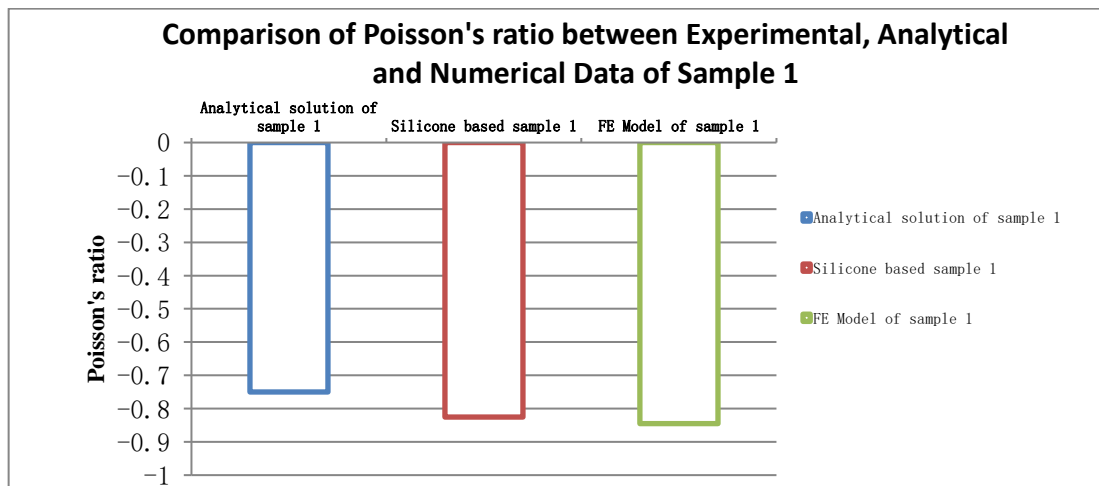
(e) Comparison of the Poisson's ratio between experimental, analytical and FE modelling data.

Figure 4.17 Experimental and FE modelling data of an auxetic structure (Sample-1).

Figure 4.17 (a) shows a silicone rubber sample resembling an auxetic structure (designated as sample-1). The sample is made by rubber casting of a platinum cure

84

silicone rubber resin with SILASTIC T4 base and SILASTIC curing agent (Thomson Bros Ltd., Newcastle). In the process, the curing agent and translucent base is mixed at a mass ratio of 1:10 and degassed in vacuum chamber before being poured in a simple mould. The cross-sectional shape of the beam is square (7mm*7mm). The deformed model of the Auxetic mesh under tension load is shown in Figure 4.17(b). In the test, the mesh was stretched from one end while the other end was fixed. The deformation process was captured on video and the dimensions were calibrated using a ruler. The total displacement applied is 42mm. The Poisson's ratio is calculated using the displacement and strain data in the lateral direction and the axial direction. The Poisson's ratio is calculated following equation 6.1.

$$v = - \frac{\varepsilon_t}{\varepsilon_l} \qquad (6.1)$$

where: v is the resulting Poisson's ratio, ε_t is transverse strain (negative for axial tension (stretching), positive for axial compression), ε_l is axial strain (positive for axial tension, negative for axial compression).

Figure 4.17 (c) shows the FE model of the Auxetic sample-1 (Figure 4.17(a)). The model mimics the exact dimension and shape of the sample and boundary conditions of a tensile test. The model is meshed with beam elements (B31) with a square cross section. One plate is fixed (labelled as the fixed plate), and the other is being pulled to a predefined displacement. The plate is much stiffer than the material for the Auxetic mesh (deformable part in $E_{plate}=10000000E_{mesh}$). The reason for using a deformable plate rather than a "rigid body" lies in the fact that in ABAQUS, a rigid part can't be merged with a "deformable" mesh. Figure 3.6(d) shows the deformed shape of the sample-1. It is clearly shown that the deformation model of the sample is comparable to the experimental image. In the FE model, the lateral elongation of the Auxetic mesh can be determined by continuous recording of the displacement of a pair of nodes in the axial and the lateral direction, so the Poisson's ratio can be calculated using equation (6.1). Figure 4.17(e) plots the Poisson's ratios of sample-1 calculated from experimental tests, FE modelling and published theoretical data (Gaspar *et al*, 2005). The Poisson's ratio based on FE modelling is slightly higher (5%) than the experiment data on the silicone sample. Both are slightly (9%) higher than the theoretical analytical solution (-0.73), which is based on the deformation of a perfect unit cell. These agreement shows that the FE model is reasonably accurate.
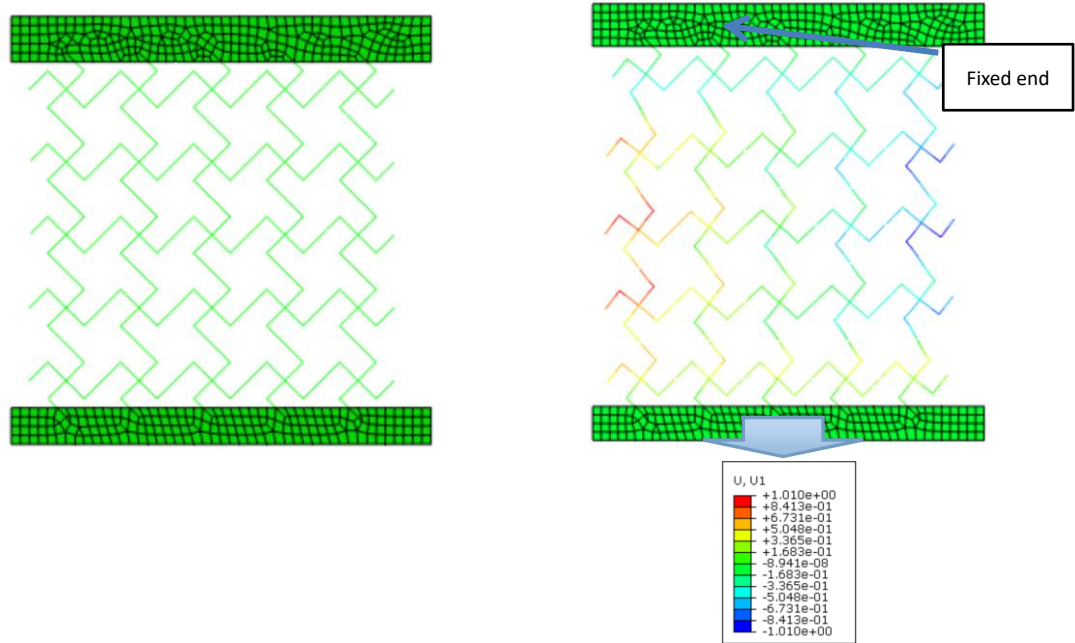
(a) FE model sample-2 (unloaded state).   (b) FE model sample-2 (deformed state).
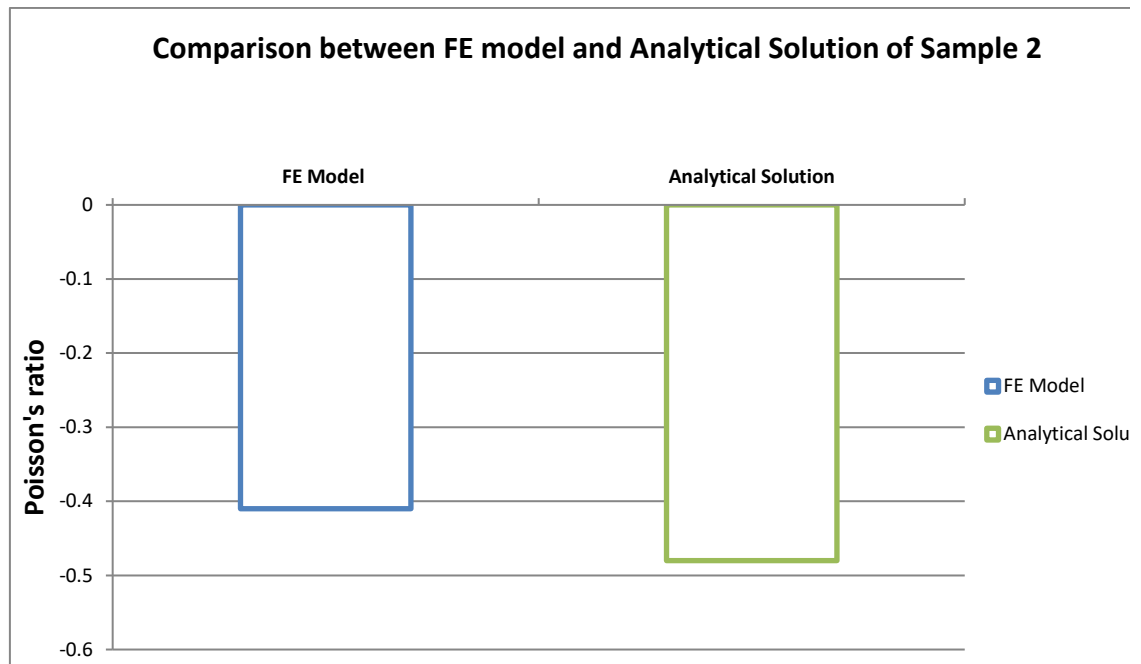
(c) Comparison of Poisson's ratio between numerical and analytical data of sample-2.

Figure 4.18 FE simulation of Auxetic Sample-2 and predicted Poisson's ratio from numerical data and analytical approach.

Figure 4.18 (a) and (b) shows the FE model and deformed shape of another auxetic structure (Sample-2). The total number of elements is 1041. The material properties of the beam applied is E=2.41MPa, v=0.495. Figure 4.18(c) compares the Poisson's ratio from FE model and analytical solution (based on a single unit cell). The data shows that the Poisson's ratio from the FE model is slightly higher than the value based on the

analytical analysis. The difference is within 10%.
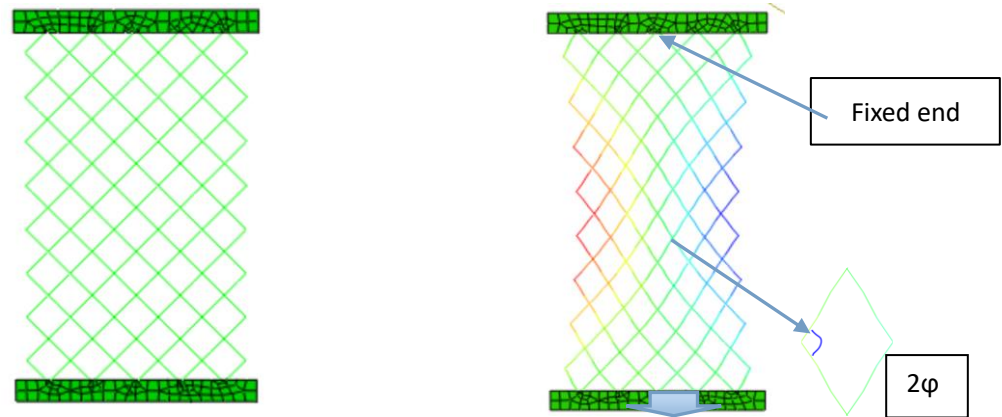
(a) FE model of non-auxetic structure (sample-3, Unloaded state)

(b) Deformed shape of non-auxetic structure (Sample-3).
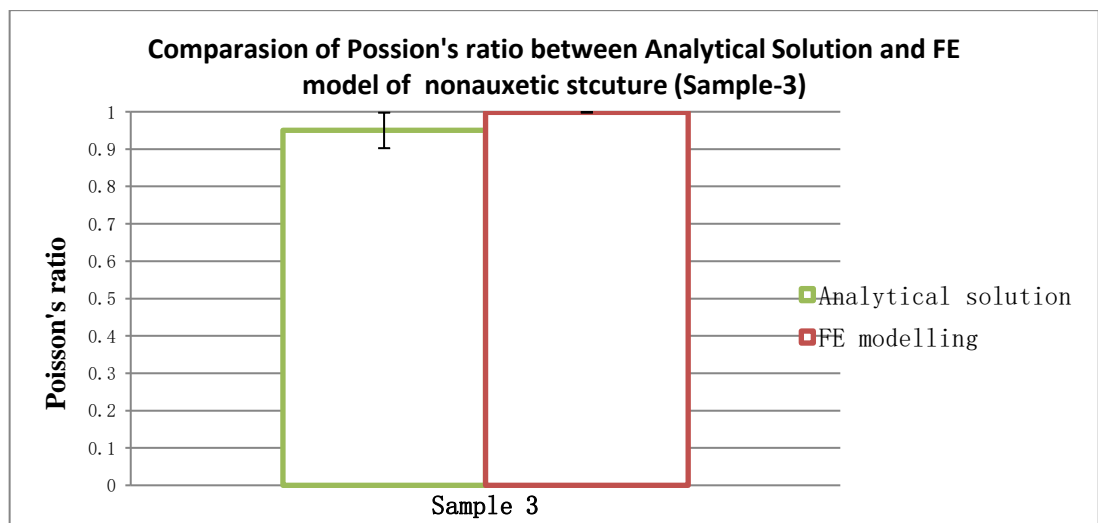
(c) Poisson's ratio comparison between FE model and analytical solution.
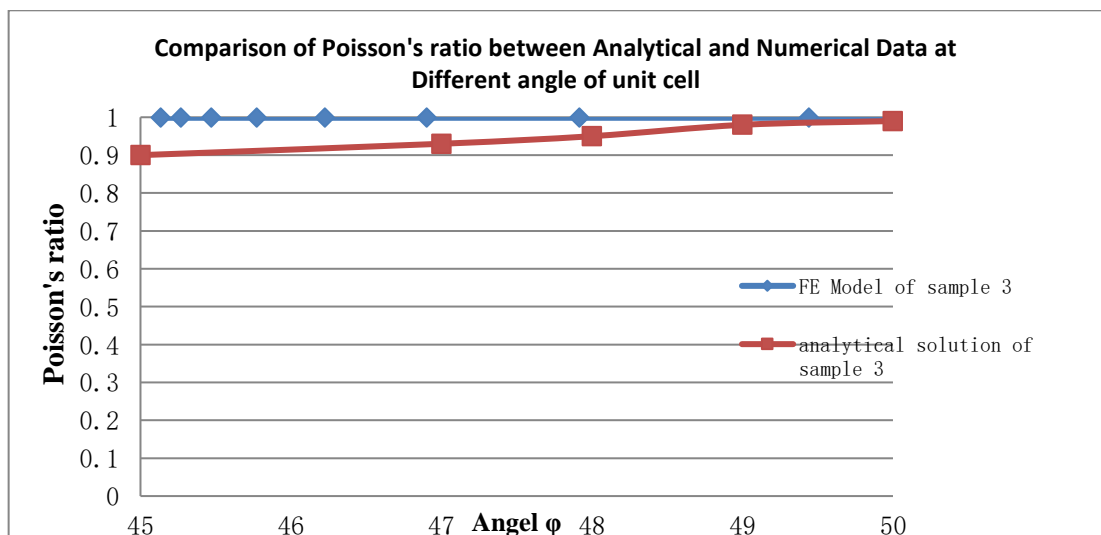
(d) Poisson's ratio changing with the angle of structure.

Figure 4.19 FE models of a non-Auxetic structure (Sample-3) and predicted Poisson's ratio from numerical data and analytical equation.

Figure 4.19 (a) and (b) show FE model and deformed shape for another common 2D structure (Sample-3). The Poisson's ratio based on the FE model is 0.9908, which is very close to the Poisson's ratio from analytical solution (within 5%) as shown in Figure 3.7(c). The Poisson's ratio from FE modelling shows no significant change with increasing axial strain, in this case represented by the angle of the unit cell in the axial loading direction. The Poisson's ratio from the analytical analysis exhibits a clear increasing trend with increased axial stretch. As shown in Figure 4.19 (d), the Poisson's ratio is increased by about 10% when the angle of canter unit of sample increased from 45°to 50°(16.67% stretched in longitudinal direction in FE model). The value of Poisson's ratio based on the analytical solution eventually becomes identical to the FE data (difference less than 1%). The data shown in Figures 6.5, 6.6 and 6.7 clearly suggests that the FE model is reasonably accurate in predicting the deformation of 2D structure within the displacement range applied. The Poisson's ratio from the FE model shows a general agreement with experimental data and in all the cases is in a reasonable agreement with the Poisson's ratio from analytical analysis.
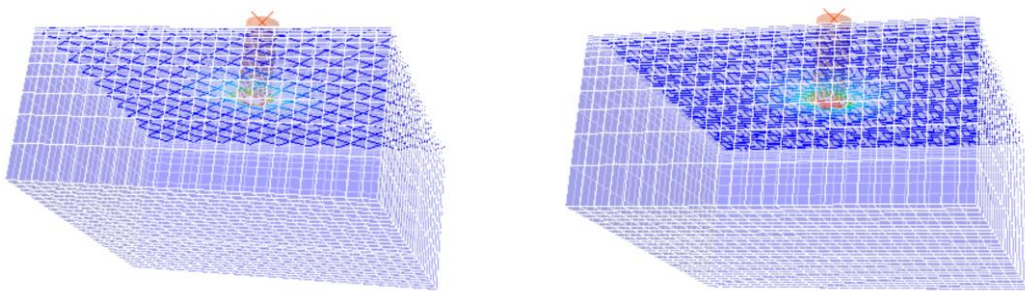
(a) Deformed FE model with an embedded non-Auxetic mesh.

(b) Deformed FE model with an embedded Auxetic (Negative Poisson's ratio) mesh.
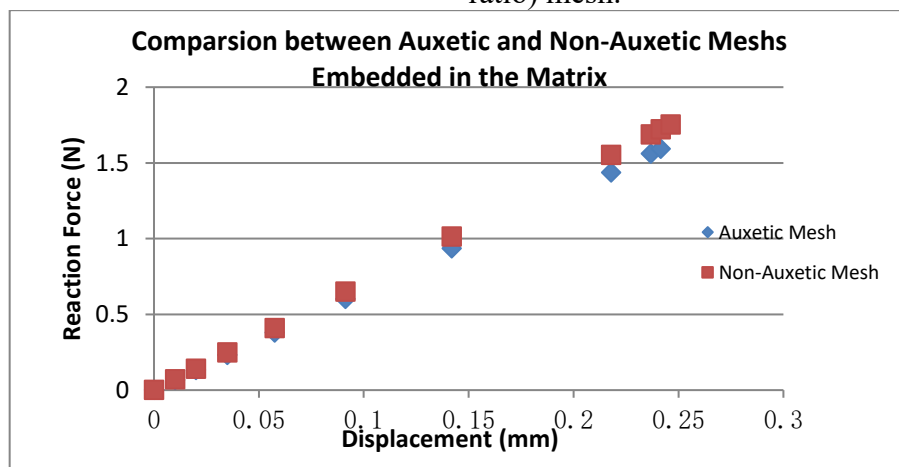
(c) Force displacement data with embedded 2D Auxetic mesh.

Figure 4.20 FE model of embedded 2D mesh (non-auxetic vs. auxetic) and typical force indentation depth data ($E_{mesh} = 10E_{matrix}$, Poisson's ratio of matrix = 0.3).

Figures 6.8 (a) and (b) show the FE indentation model of an embedded mesh of a regular structure (positive Poisson's ratio, Sample-3) and Auxetic mesh (Sample-1). In this case, the Young's modulus of materials in Auxetic mesh and normal mesh are ten times of the matrix (E=3MPa, v=0.3). Both of them are placed 0.1mm from the top surface of the sample. As shown in Figure 4.20(c), the deformation of sample with an embedded Auxetic mesh is slightly lower than normal mesh as the indentation depth increases. The FE model and the Python program would allow future works in developing new structures with abnormal Poisson's ratios, which can be potentially used in sport insoles.

4.6 Summary

In this work, the deformation of a soft material with an embedded stiffer layer under a cylindrical flat indenter was investigated through FE modelling. A practical approach in modelling an embedded system is evaluated and presented. The FE results are correlated with an analytical solution for homogenous materials and results from a mathematical approach for embedded systems in a half space. The indentation stiffness/resistance of soft material systems with an embedded thin layer under a flat-ended indenter for matrix of both positive and negative Poisson's ratio values were systematically studied. The influence of auxeticity on the indentation stiffness ratio and the deformation of the embedded system under different conditions (indenter size, thickness and embedment depth of the embedded layer) was established and key mechanisms of the Poisson's ratio effect are highlighted. The results show that the auxeticity of the matrix has a direct influence on the indentation stiffness of the system with an embedded layer. When the embedment is close to or on the surface of a matrix, with a high positive Poisson's ratio (e.g. 0.5), the shell has limited effect on the indentation resistance. The enhancement of indentation resistance due to embedment increases, as the matrix Poisson's ratio is decreased to zero and to negative values. The indentation stiffness could be increased by over 30% with a thin inextensible shell on top of a negative Poisson's ratio matrix. The deformation of the embedded layer is significantly influenced by the auxeticity of the matrix. With a non-auxetic matrix, the embedded layer underneath the indenter is being pulled, while for auxetic matrix, the embedded layer is being pushed due to the combined influence of the deformation of the auxetic matrix. The modelling approach for cases in which piezoelectrical sensors, force sensitive resistor and auxetic mesh was used as the embedment showed that the modelling approach is effective in predict the mechanical and electrical response of the embedded sensors under different loadings.

CHAPTER FIVE PARAMETRIC

FINITE ELEMENT FOOT

MODELLING AND EFFECT OF

LOADING CONDITIONS AND

MATERIALS

5.1 Introduction

This chapter presents a newly developed Python based Abaqus plug-in investigating the deformation of the human foot in different landing conditions and use of the model in evaluating the effect of structure and properties of the shoe sole on the foot response including soles with embedded structures and Auxetic properties. This could potentially improve the efficiency of foot biomechanical modelling for research and product development. In the first section, an FE foot model is developed to simulate the deformation of the human foot under a standing position to simulate a Navicular Drop Test. The models used a full bone structure and effective embedded structure method to increase the modelling efficiency. The detailed deformation of the Navicular bone and factors affecting the Navicular bone displacement and measurement is discussed. The second part is focused on comparing the stresses and energy in the foot during forefoot strike (FS) and rearfoot strike (RS). A hexahedral dominated meshing scheme was applied on the surface of the foot bones and skin. An explicit solver (Abaqus/Explicit) was used to simulate the transient landing process. The deformation and internal energy of the foot and stresses in the metatarsals are comparatively investigated. In the third part, the effect of some key parameters of a shoe sole such as stiffness, thickness, an embedded shell and negative Poisson's ratio is evaluated using the FE models developed.

5.2 Main materials, design and modelling factors considered in the Abaqus Foot Modelling Plug-in

Figure 5.1 shows the key factors to be considered when developing the user interface for foot mechanics studies. As detailed in the literature review, the human foot has a fixed number of components even though the dimension and shape vary from different subjects. This offers a case where the Python based Abaqus plug-in can be used to enhance the efficiency of FE modelling with a user interface. Normally the model can be developed based on medical images (CT and/or MRI). The materials for both the bone and tissue are also important. In published works both linear elastic or hyper elastic/foam can be used depending on the loading conditions and accuracy and efficiency requirements. For evaluating the effect of the properties, dimension or new structure (e.g. partitioned soles, plug-in or embedded structures), an interface can effectively make the process much easier without relying on a very experienced FE operator. It can also be remotely loaded onto Abaqus. One main focus of this work has been on the ability of the plug-in to change the position and the orientation of landing in particular forefoot and rearfoot strikes. The FE also incorporated an improved mesh (compared to previous FE models in the group) with increased use of hexagonal element at the surface by combining the operation in the FE package Altair and Abaqus.
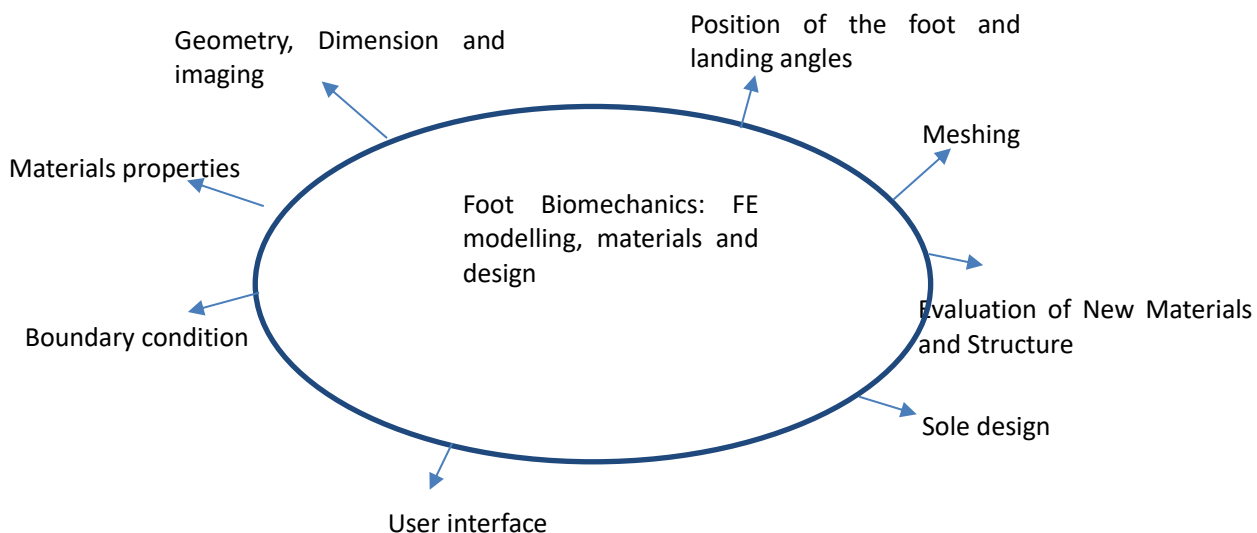
Figure 5.1 Key issues in modelling foot and foot-sole/ground interactions.

(a) Plug-in showing the main function to control the position and interactions
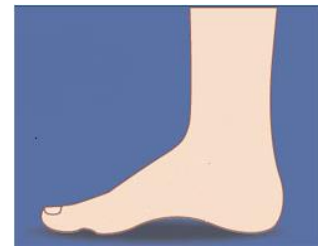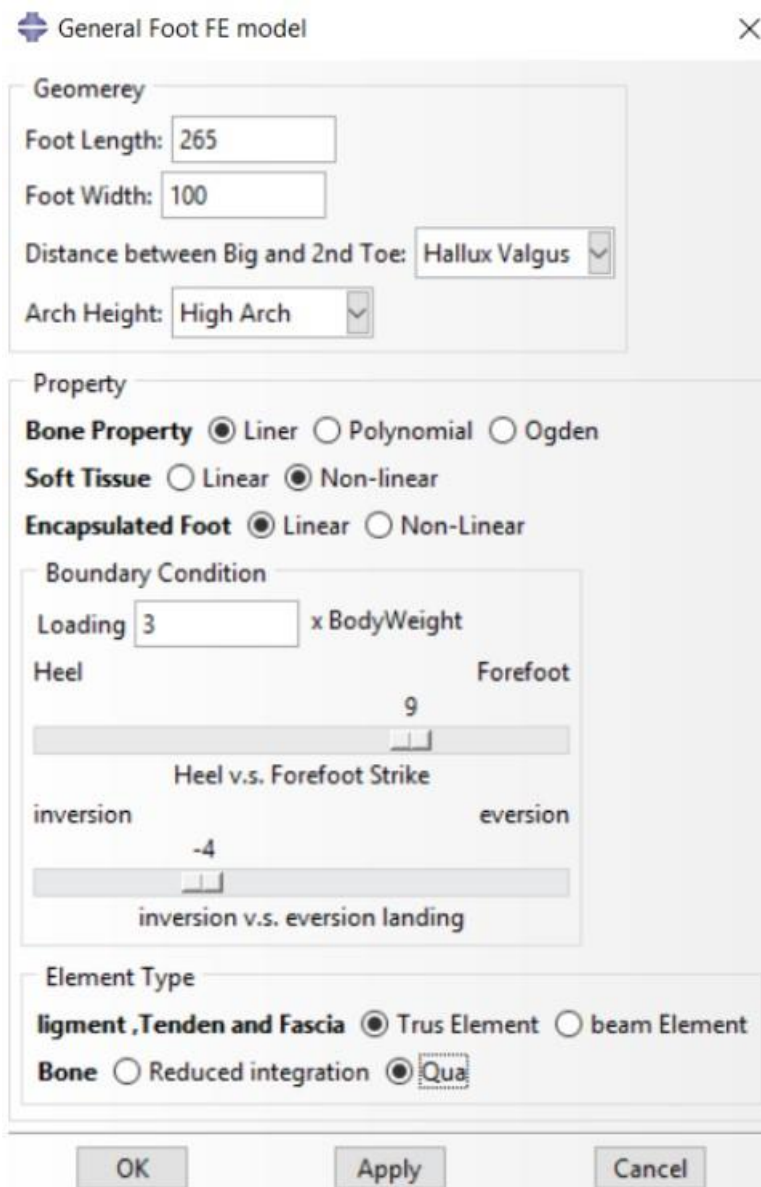
(b) Normal standing.
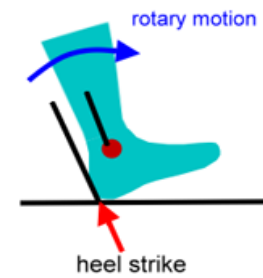
(c) Heel strike

(d) Forefoot strike

Figure 5.2 Plug-in of the foot mdoelling and illustration of the foot angle and position.

Figure 5.2 shows a typical interface, which has functional button/link for position control as well dimensional and material properties. In the materials, the user can select different material models directly for the sole or soft tissues. One key feature is a program to control the position of the foot as illustrated in Figure (b-d) including standing (b); forefoot strike (c) and rearfoot strike. The key results will be presented in sections 5.3-5. Another key development is the size control based on the foot and partition of the anatomical contacting areas. As shown in Figure 5.3, the program automatically partitions the sole into different regions and the force over each region is then calculated. This is an important feature for biomechanical studies (Smith et al, 2000; Henning et al, 2010).   To

study contact force in different areas of the foot, the contacts need to be partitioned. According to common topology in biomedical foot pedography, the contact area can be partitioned into Toe1, Toe2, Metatarsal1, Metatrsal2, Metatarsal3, Midfoot1, Midfoot2, and heel in order to study plantar pressure distribution in different areas. Contact force between foot plantar and ground can be reported from a history output request in Abaqus Python. The program was written to partition the contact area according to the topology method in biomedical pedography. The foot width index (foot width / foot length) was programmed parametrically to ensure the partition method is fit for the specific foot model. As shown in Figure 5.3, different aspect ratios of partitioned footprints are displayed when the inputs have different foot Width Indexes. Then the contact force on each area can be precisely plotted through post-processing.

```python
FL = float(getInput('Foot Length'))    #foot Length

FW = 0.33* FL #float(getInput('Foot Length'))    #foot width

FW2 = 0.58*FW

FW3 = 0.256*FW                          #68/2650

FW4 = 0.143*FW                          #38/265

v1 = (75, 0)
v2 = (39.64, 14.64)
v3 = (25, 50)
v4 = (27, 100)
v5 = (29, 150)
v6 = (0, 190)
v7 = (12.27, 267.5)
v8 = (47.64, 300.0)
v9 = (122.27, 267.5)
v10 = (150, 190)
v11 = (136.03, 130)
v12 = (132.72, 100.0)
v13 = (124,50)
v14 = (110.35,14.64)

X = 0.7                 #Width Index

v1 = ( v1[0]*X*FL/300, v1[1]*FL/300)
v2 = ( v2[0]*X*FL/300, v2[1]*FL/300)
v3 = (v3[0]*X*FL/300, v3[1]*FL/300)
v4 = (v4[0]*X*FL/300, v4[1]*FL/300)
v5 = (v5[0]*X*FL/300, v5[1]*FL/300)
v6 = (v6[0]*X*FL/300, v6[1]*FL/300)
v7 = (v7[0]*X*FL/300, v7[1]*FL/300)
v8 = (v8[0]*X*FL/300, v8[1]*FL/300)
v9 = (v9[0]*X*FL/300, v9[1]*FL/300)
v10 = (v10[0]*X*FL/300, v10[1]*FL/300)
v11 = (v11[0]*X*FL/300, v11[1]*FL/300)
v12 = (v12[0]*X*FL/300, v12[1]*FL/300)
v13 = (v13[0]*X*FL/300, v13[1]*FL/300)
v14 = (v14[0]*X*FL/300, v14[1]*FL/300)

vtotal = 14
Spline = []

for i in range (1,vtotal+1):

    Spline = Spline +[eval('v'+str(i))]

Spline = Spline + [v1]
print Spline

s.Spline(points=Spline)
```
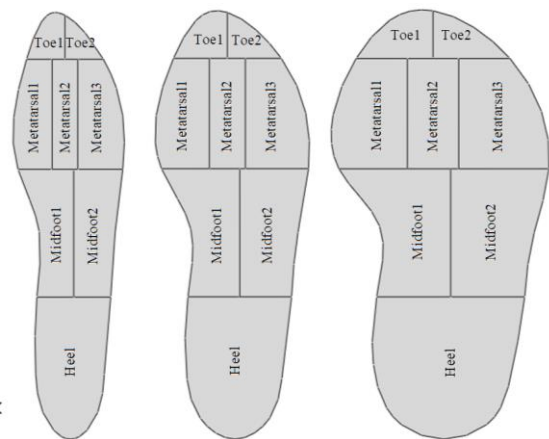
(a) Typical Pyhton code.

(b) Figure showing the partition anatomic zones foot change with the foot size and aspect ratio. [i] Toe1, [ii]Toe2, [iii] Metatarsal1, [iv] Metatarsal2, [v] Metatarsal3, [vi]Midfoot1, [vii] Midfoot2, and [x]Heel.
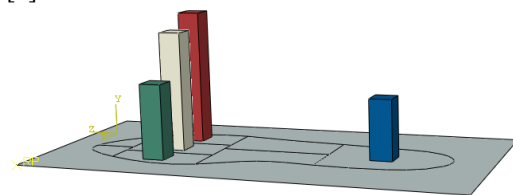
(c) Illustrtaion of the force in different areas, which is an important parameter in foot mechanics.

Figure 5.3 Feature of the plug-in to partition the contact area and calculate the force in different regions.

The details of the meshing development (Figure 5.4), the foot and bone deformation in standing, forefoot and rearfoot strike, and the effect of the dimension, properties of the

sole material and new structure (auxetic behaviour and embedded layers) are presented in sections 5.2-7. A discussion on the key results vs. published data, limitation of the work and future development is presented in section 5.8.
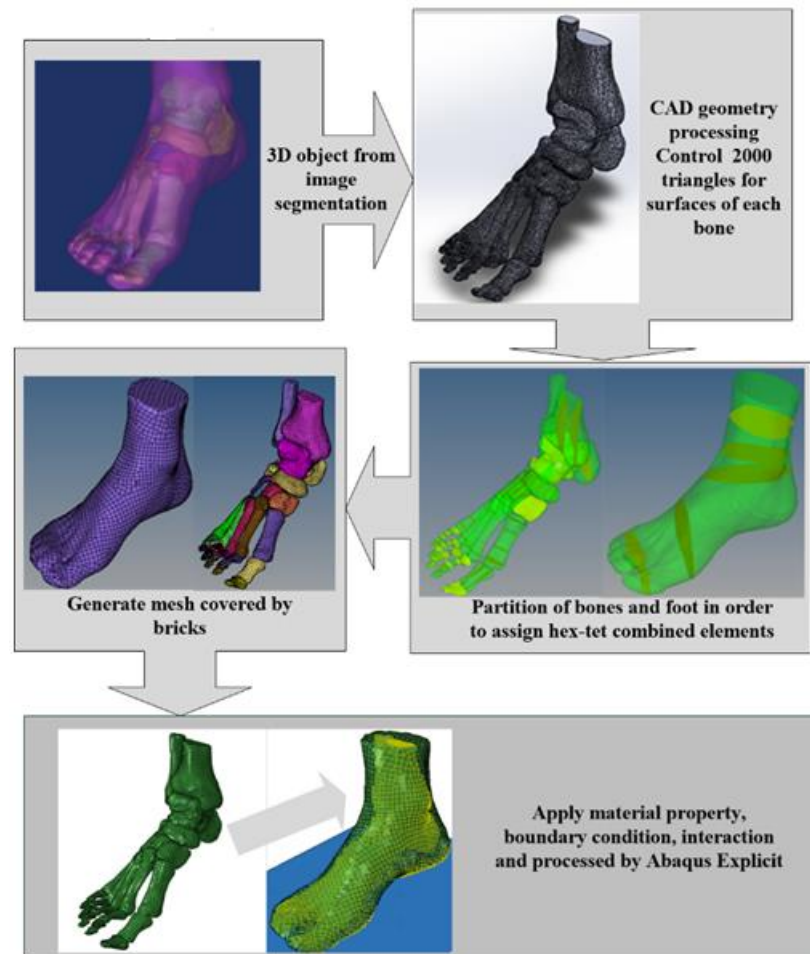
Figure 5.4 Foot models and meshing method to optimise the use of hex-tet combined meshes.

A range of material properties and models are used for different foot structures and parts. An analytical rigid plate was used to represent the ground to simulate the foot–ground interaction during landing. This is close to the biomechanical testing condition, it is also representative of a more damaging situation to the metatarsals. The bones are defined as a linear elastic isotropic material (Young's Modulus = 7300MPa, Poisson's ratio = 0.3) (Nakamura et al, 1980). As in previous works (Gu et al, 2011) and other literatures (Yu et al, 2013), the stiffness of the Cartilage, Plantar Fascia and Ligament is set at 1, 350 and 250MPa, respectively; the Poisson's ratio is set as 0.4. The phalanges are assumed to have the same material properties as the bones (Abaqus 6.14). The density for the bone is 1500kg/m^3, the density of the tissue is 940 kg/m^3. A Rayleigh material damping coefficient (alpha) 6.7 was defined to represent the viscous behaviour of the soft

tissue in ABAQUS (Abaqus 6.14). The remaining soft tissues which encapsulated the bony structures was described by a hyperelastic model with a second-order polynomial strain energy potential obtained from *in vivo* ultrasonic measurements (Lemmon et al, 1997).

$$U = \sum_{i+j=1}^{2} C_{ij}(\overline{I_1} - 3)^i (\overline{I_2} - 3)^i + \sum_{i=1}^{2} \frac{1}{D_i} (J_{el} - 1)^{2i}$$

where U is the strain energy per unit reference volume; C_{ij} and D_i are material parameters. J is the volume ratio; I_1 and I_2 are the first and second deviatoric strain invariants. The coefficients of the hyperelastic material used for the encapsulated soft tissue is $C_{10} = 0.08556$, $C_{01} = -0.0841$, $C_{11} = -0.02319$, $C_{02} = 0.00851$, $D_1 = 3.65273$, $D_2 = 0$ (Gu et al, 2011; Lemmon et al, 1997). The data was obtained through an *in vivo* compression measurement with several cohorts and inverse parameter fitting, the model had been used in serval published biomechanical works (Gu et al, 2011; Cheung et al, 2005). When $D_2 = 0$, it represents full incompressibility. Theoretically incompressibility can cause volume locking. For linear elastic models, this can be practically dealt with by using a Poisson's ratio close to 0.5. For hyperelastic model, full volume locking with an incompressible material can be avoided by using elements with reduced integrations. High quality meshes are also important for dealing with modelling problem due to incompressible behaviours (Abaqus 6.14). In the standing models, the foot is perpendicular to the plate. In forefoot landing, the foot approach plate at an angle as hsown in Figure 5.2 (d) while rearfoot strike, the heel touches the plate forta at an angle as shon in Figure 5.2(c). Surface to surface contact was use with a friction coefficient of 0.6 between the foot and plate.

5.3 Simulation of the deformation of the foot and Navicular drop in standing

Figure 5.5 shows the FE model simulating standing on a rigid ground. Standing load on foot model over rigid plate is used to validate the foot model. Navicular drop test (NDT) was used to verify the deformation of foot model under standing load. In the test, three reflective markers were stuck on the navicular bone, heel, and first metatarsophalangeal joint (Figure 5.5 (a)). The subject transferred the body weight from the back foot entirely to the front foot while standing in a line. High speed camera recorded the foot from unloaded to full load at 500HZ. The displacement of the marker on the navicular bone was read. The true distance of the navicular drop was calculated from imaging calibration. Simulated NDT result was computed and then compared to the clinical measurement from the same subject and the published data. Figure 5.5 (b) shows the simulated deformation of the foot under body weight. When the vertical displacement of the arch point on the navicular bone reaches 7.8mm, the ground reaction force is equal to the body weight of the subject. As shown in Figures 2(a&b), the general foot deformation and the contour of the vertical deformation is slightly different, as the structure undergoes both vertical and lateral deformation. Figure 5.6 (a) (b&c) shows the vertical displacement of the bone structure and the navicular bone. The contour of the navicular bone has undergone a certain degree of rotation, but the main movement is downward. The average of the vertical displacement is 8.2mm. A Python code has been used to extract the displacement data of the navicular bone, then the average value is calculated.

(a) Undeformed	(b) Deformed
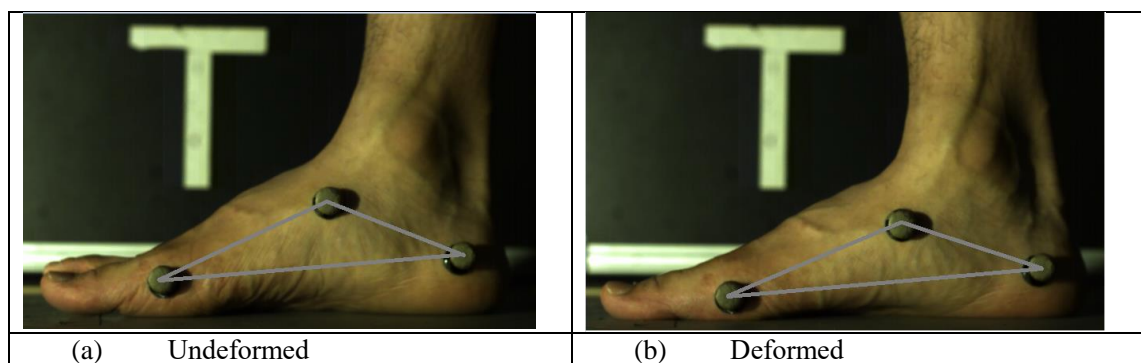
Figure 5.5 Illustration of the Navicular drop measurement of the foot.

As shown in Figure 5.6, the physical NDT on the same subject by high speed camera shows a reasonable agreement between the experimental and numerical result. This suggests that the modelling with the simplified approach of treating the bone structure as an embedded system in the foot model is accurate under static standing loading condition. This will make it easier to use the model in biomechanics-led shoe sole development for optimizing material selection and pressure distribution. Further comparison between FE data and published data (Nielsen et al, 2009; Picciano AM, 1993; Moul, 1998) of NDT

result as shown in Figure 5.6 also shows a good agreement.

(a) General deformation field of the foot.   (b) Vertical displacement (U2) only.   (c) Vertical displacement (U2) of the bony structure.   (d) Vertical displacement (U2) of the navicular bone.
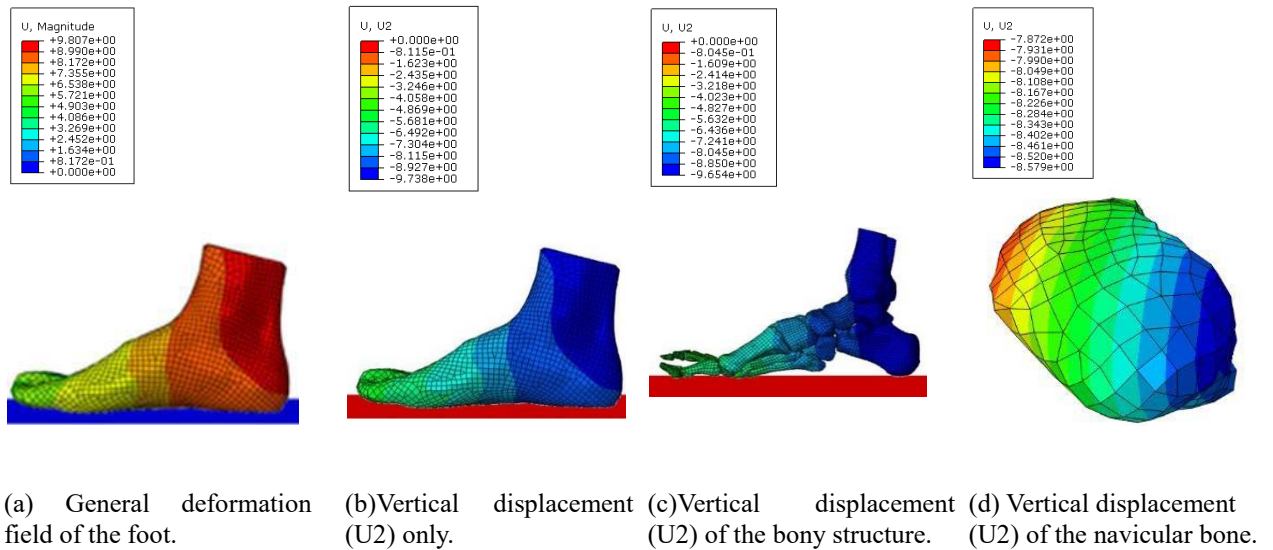
Figure 5.6 Deformation of the foot and Navicular Drop of foot at standing condition.

Research works have shown that the navicular drop (ND) can be influenced by many factors (such as age, gender, medical conditions, and external structure in contact with the foot). In the statistical model by Nielsen et al (2009), it is found that the ND is loosely correlated to the length of the foot, and the relationship is different between the data for female and male subjects. This is an interesting factor but difficult to research purely based on experimental works. The validated model offers a potential means to establish the effect of foot length and original angle on the ND of the subjects. Another issue to be studied is on the potential effects of the skin on the variation or distribution of the NDT based on the markers.
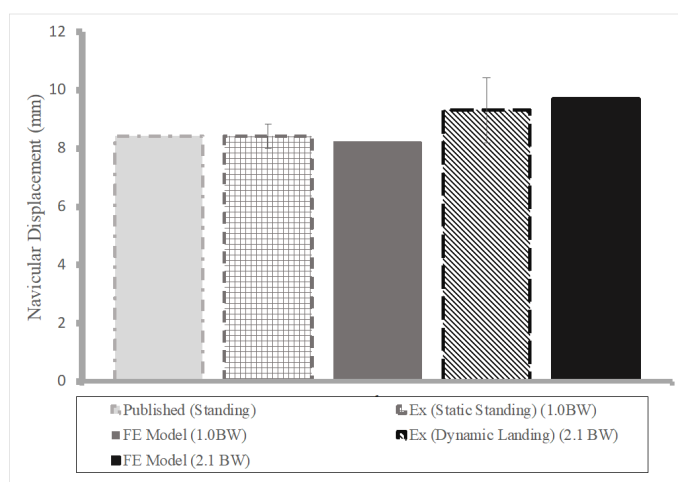
Figure 5.7 Comparison of NDT between published data, numerical and experiment of the same subject.

5.4 Simulation of the Plantar pressure

Plantar pressure measurement is another common way to analyse different gaits or running styles. Distribution of the pressure on the plantar indicates the pattern of gaits and provides a means to access the validity and accuracy of the FEM. Figure 5.7 shows the distribution of plantar pressure from FEA and platform pressure measurement (Emed pedography platform. Novel GmbH, Munich, Germany) under static standing load. As shown in the figure, two frames of standing were selected when the ground reaction force GRF is equal to 0.5 body weight (BW), and 1BW. Pressure distribution from the FE result showed a good agreement with the experimental result measured on Emed pedography platform. The value of peak pressure between FE and test data match at both the point of 0.5 BW and full BW loading. For the pressure measurement (Figure 5.7), it should be noted that the system used discrete electrical sensors, and the distribution/contour is formulated through the homogenisation of the reading of each pressure sensor. From the pressure distribution, it is clear that the global distribution of maxima and minima is similar and maximal stresses are also similar. This suggests that the model is valid in terms of the key aspects of the foot model such as geometry, position of the bones and materials, etc. The pressure values for the heel and forefoot region are also in general agreement with published data (Figure 5.8), which will be discussed in detail in the discussion.
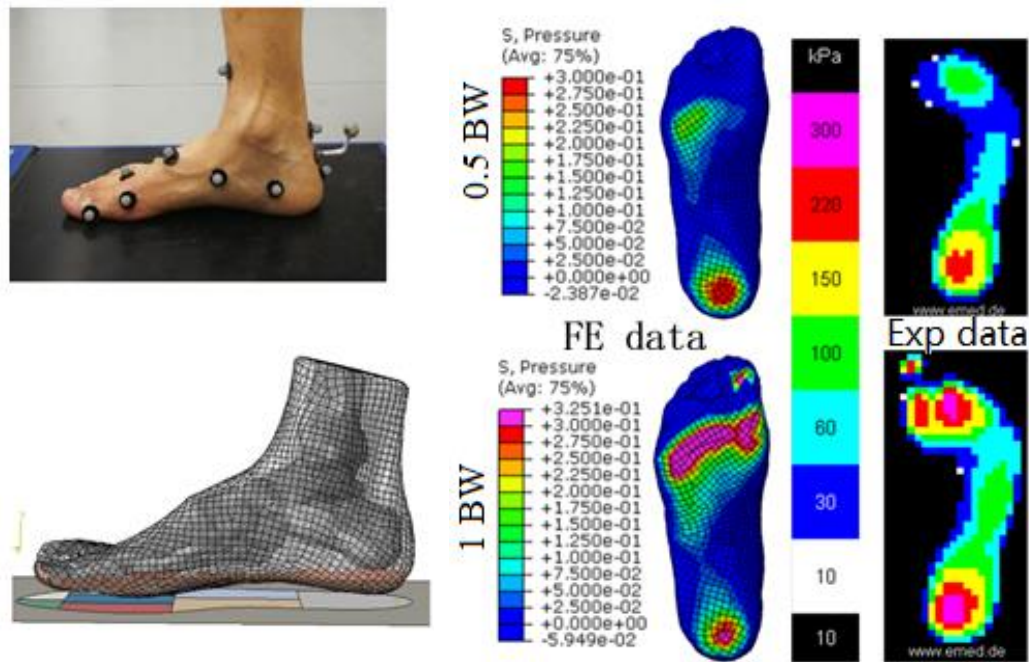
Figure 5.8 Foot validation method II. Plantar pressure distribution comparison between FE and experimental work under standing load.

The navicular bone is the pivoting point of the foot that provides a good means for validation (Moul 1998) for works focusing on metatarsals. In the static standing tests, the load is 1BW; for dynamic tests, the load is around 2.1BW. During the experiment, for the static standing test, the subject slowly stands on the platform, while for the dynamic test, the subject was asked to hold the parallel bars to lift himself up straight before landing from 100mm height (distance from foot plantar level over the ground) to the rigid ground by full foot contact (i.e. forefoot and rearfoot touching ground at the same time) where the Emed pressure measurement plate was placed. Ground reaction force from the Emed plate showed maximum reaction force around average 2.1 Body weight. The GRF for standing test is much more reliable, while there is clearly variation of the GRF between different dynamic landing tests as represented by the error bar. However, the average value showed a reasonable agreement between the FE modelling and the tests. The close agreement of displacement measured from both static standing and dynamic vertical landing shows that the model is geometrical sound. The displacement of the proximal end of 1st metatarsal has also been evaluated, the modelling results show a reasonable agreement with the tests, but the repeatability of the Proximal end of 1st metatarsal is not very reliable, the data was not shown to preserve clarity. These results will give more confidence in using the computational model to predict the deformation of internal bones such as the metatarsals, which cannot be measured. Further discussion is presented in the discussion section to compare the predicted results with other published data under comparable conditions or more challenging situations as well as the limitations of the approach.

Figure 5.9 Typical FE data for Forefoot strike. (a) Deformation in sagittal plane at initial touchdown (0.5BW), (b) stress distribution in axial plane at initial touching-down, (c) deformation in sagittal plane at full contact (2BW), (d) stress distribution in axial plane at full contact.

5.5 Forefoot and Rearfoot Landing and Landing comparison

Foot strike pattern is a major determinant influencing the lower extremity biomechanics during running. Forefoot strike and rearfoot strike are two typical landing styles of running (Lieberman, 2012; Shih et al 2013). In forefoot strike, the ball of foot impacts with the ground first, during which, the foot initially lands with a plantarflexion posture followed by a dorsiflexion movement. Compared to rearfoot strike, forefoot strike cuts down the impact and reduces the shock passing to the brain as the impact is absorbed by the compression of the foot arch, eccentric contraction of the triceps surae, calf muscles and Achilles tendon stretch (Lieberman, et al 2010). The pressure excursion during forefoot strike that moves backward was once considered an energy waste but was later proven to provide cushioning for runners (Divert et al 2005). Recent researches showed the vertical loading rate of a habitual barefoot runner can be significantly reduced by changing their landing pattern from rearfoot strike to non-rearfoot strike (Squadrone et al 2009; Crowell and Davies 2011). In the work by Lieberman (2010), no obvious impact transients were found in the typical force-time data of forefoot strike. Conversely, the force-time curve of classic rearfoot strike is always showing an impact transient before the vertical ground reaction approaches its peak. During the impact period of a rearfoot landing, the vertical Ground Reaction Force (GRF) can be 3 times higher than the forefoot landing of habitual barefoot runners (Lieberman et al 2010). In rearfoot strike running, impact absorption is limited to the rearfoot pad and shoe, leading to higher peak impact and generating the shock wave, This could lead to high stress and strain directly contributing to certain injuries (Daoud et al 2012). This is one of the reasons that running in minimalist footwear was considered as a means of reducing or eliminating running injuries by returning to a more natural gait.

The average displacement history at the top surface of the model (including tibia, fibula and soft tissue) was used to control the foot landing in the model, this is more realistic than moving the plate (Fontanella et al 2015; Qiu et al 2011; Gu et al 2010). The initial touchdown angle in forefoot and rearfoot strike between the foot plantar and the ground was defined as 5° by gait measurement with reflective markers. Convergence studies are influenced by the mesh quality, linear damping parameters and time steps used, etc. We have evaluated the effect of the damping parameters using a trial and error process to minimise the ground reaction force oscillations. In the meantime, as a unique problem of the foot structure, the continuity (localized instability) of the foot deformation is also analysed as the system consists of regions with significantly different material properties.

Sensitivity studies show that the combination of material properties and simulation parameter offers a relatively robust modelling performance (i.e. no significant/abrupt drifting with a small range of perturbation (±10%) in the parameters).

5.5.1 Stress distribution on the metatarsals during forefoot and rearfoot strike

During the initial touchdown (up to half BW) for forefoot and rearfoot strike, the averaged metatarsal stress is similar around 6MPa. The stress level in the 4th metatarsal in forefoot strike is higher (7.62MPa, Figure 5.10), while the stress in the 5th metatarsal in rearfoot strike has a much lower value (4.67MPa, Figure 5.12). At full contact (2BW), there is a more significant increase in the metatarsal stresses in the forefoot strike, than that for the rearfoot strike. The percentage stress increase from initial touchdown to full contact during rearfoot strike (21.39%) is lower than the rate of increase for forefoot landing (30.76%). Figure 5.10 shows the stress data in the metatarsals between 0.5 BW and 2 BW in forefoot landing. The average metatarsal stress increase is about 30.76% from the initial contact to full contact during forefoot strike. The data shows that the 1st metatarsal experienced the lowest stress at initial touchdown, but it increases more significantly with the highest stress increasing rate of 48.21% at full contact. The data for the 5th metatarsal represents the lowest stress increasing rate (18%) from the initial touchdown to full contact. Figure 5.12 shows the stress data for the rearfoot strike. It can be seen from the data that the 1st metatarsal had the highest stress under both half body weight and twice BW. The highest stress increasing rate was presented on the 1st metatarsal during rearfoot strike. In addition to the 1st metatarsal. The lateral side during rearfoot strike (the 4th and 5th metatarsals) also showed relatively high stress increase rate (10.4% and 11.8%). The stress increases among the five metatarsals show a more evenly spread along the coronal axis during rearfoot strike than that for forefoot strike.
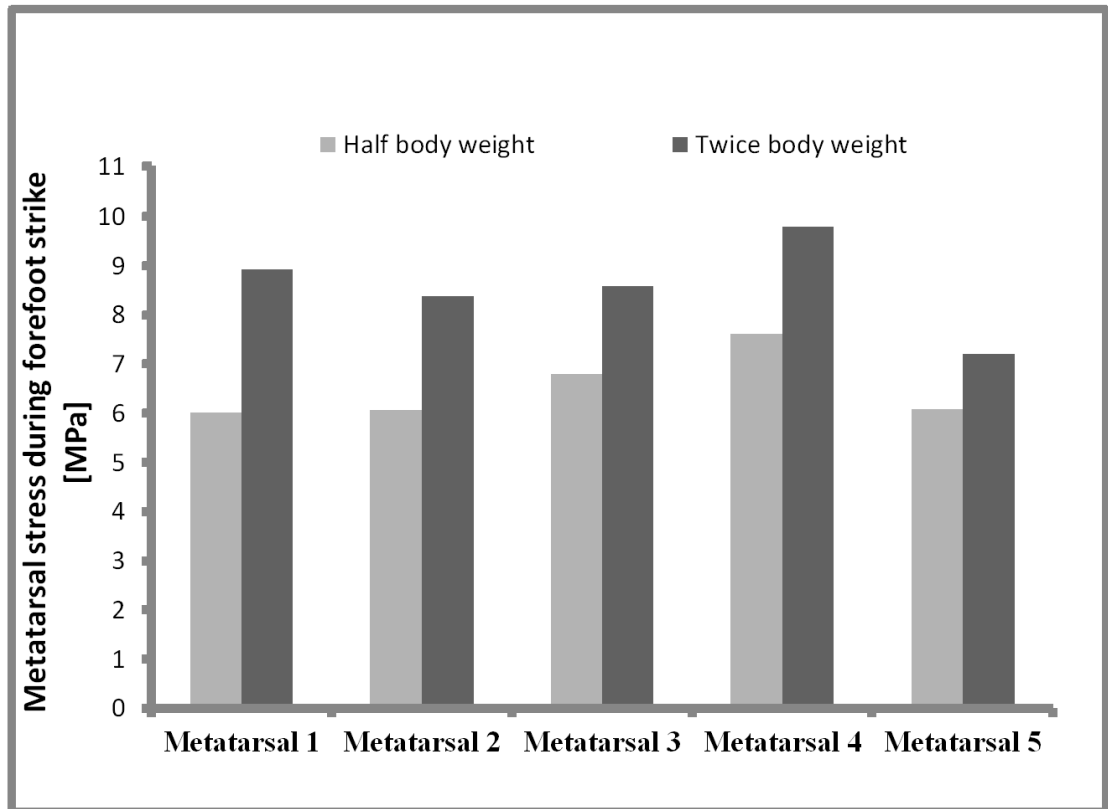
Figure 5.10 Stress on metatarsals at half and twice body weight (BW) during forefoot strike.
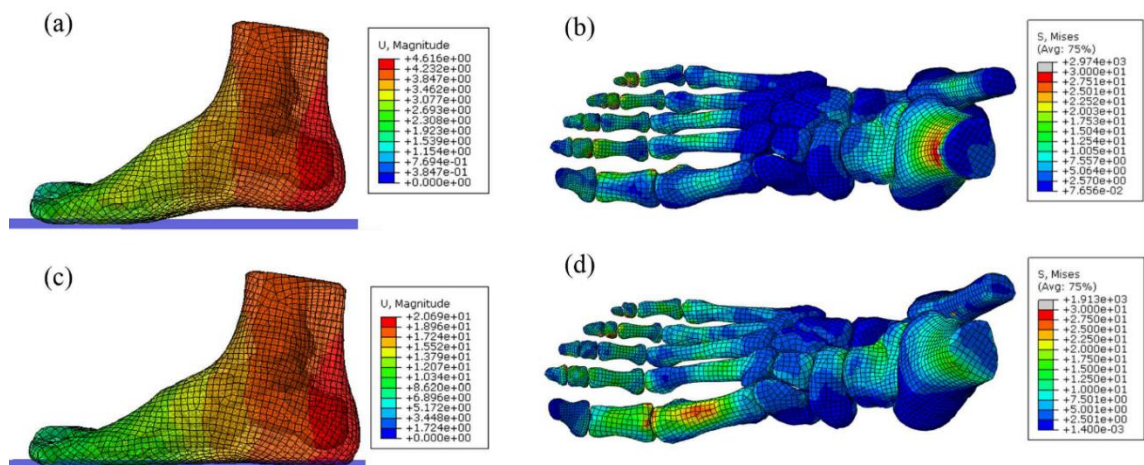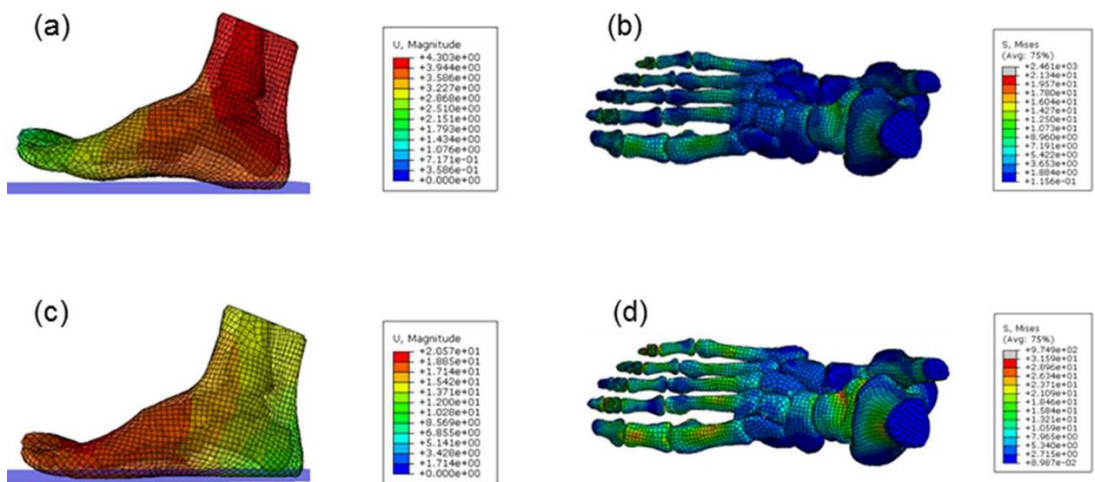

Figure 5.11 Typical FE data for rearfoot strike. (a) Deformation in sagittal plane at initial touchdown (0.5BW), (b) stress distribution in axial plane at initial touching-down, (c) deformation in sagittal plane at full contact (2BW), (d) stress distribution in axial plane at full contact.
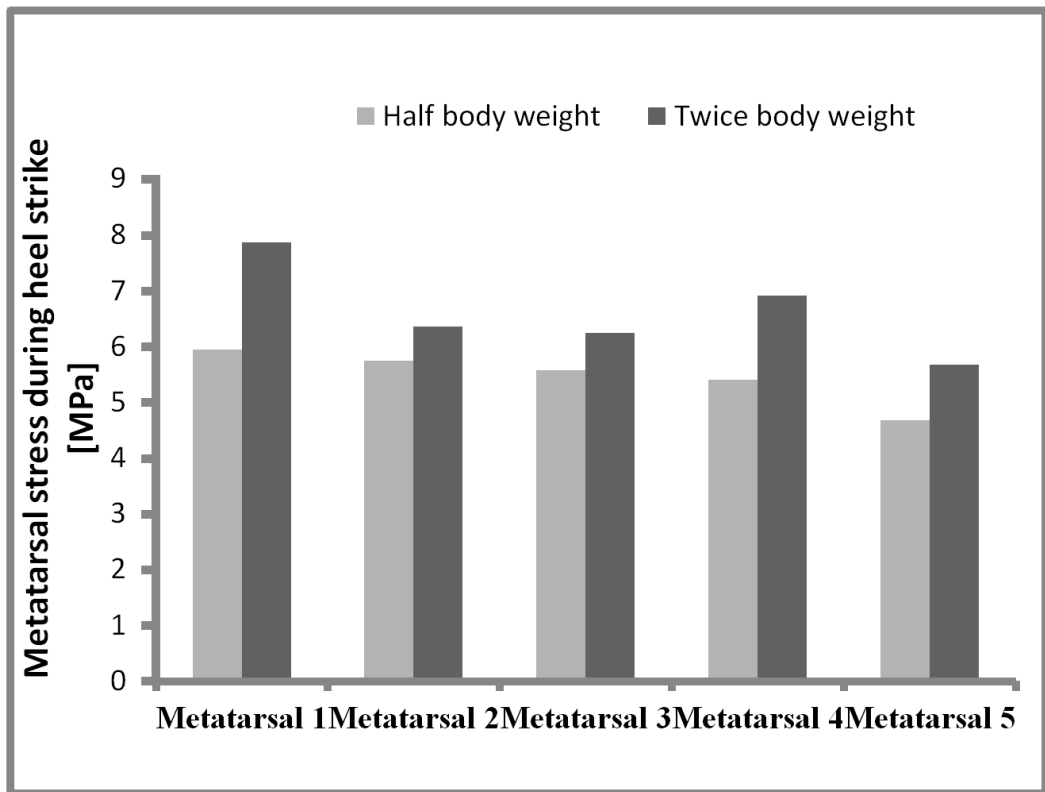
Figure 5.12 Stress on metatarsals at half and twice BW during rearfoot strike.
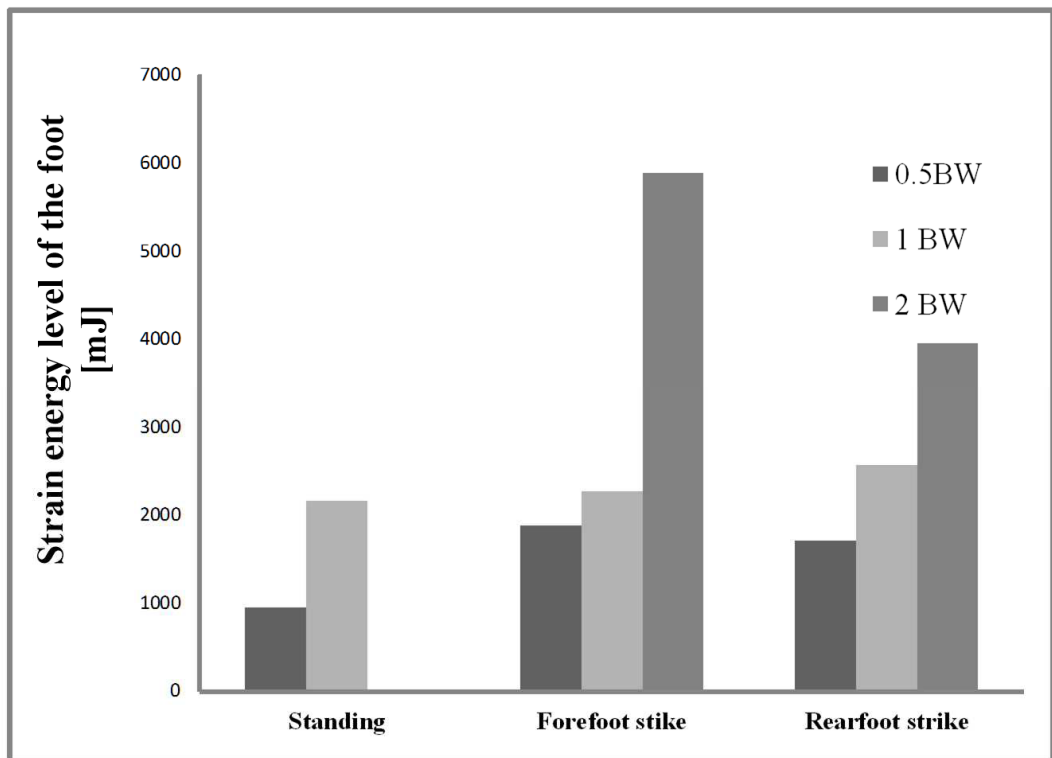
Figure 5.13 Comparison of the internal energy level of the foot during standing, forefoot and rearfoot strike. The strain energy of the foot represents the natural energy absorption.

Deformation of the foot at initial touchdown during forefoot and rearfoot landing is shown in Figure 5.9(a) and Figure 5.11(a), respectively, the vertical GRF was equal to half BW (350N) at this point. The foot deformation at full contact during forefoot and

rearfoot landing are shown in Figure 5.9(c) and Figure 5.11(c), respectively, and the GRF was twice BW (1400N) at this point. Figure 5.9(b) and Figure 5.9(d) show the stress distribution on the bones at the moment of initial touchdown and full contact, respectively during forefoot landing. Figure 5.11(b) and Figure 5.11(d) present the bony stress distribution at the moment of initial touchdown and full contact, respectively during rearfoot strike. Compared to full contact, stress distribution on metatarsals is more even at initial touchdown for both landing styles. The 3rd and 4th metatarsals bear higher stress at initial touchdown during forefoot landing (Figure 5.9(b)). During rearfoot landing, stress on the metatarsals showed more even distribution at initial touchdown (Figure 5.11(b)). For both landing styles, 1st metatarsal showed the highest stress increase rate from the initial touchdown to the full contact (Figure 5.9(d), Figure 5.11(d)).

As in the model, the plate is a rigid body, and the internal energy is also representative of the energy absorbed during the movement. Figure 5.13 shows that, at 0.5BW load, the internal energy level stored in the foot is similar, and then at 1 BW, the energy for rearfoot strike is slightly higher. While at 2 BW (which is close to the maximum (2.2-2.6 BW) (Lieberman, 2012), the energy in the foot during rear foot strike is much higher; this is due to the fact that for rearfoot, the main force is sustained by the main bony structure, the heel pad is the main deformable part. For forefoot strike, the soft tissue has a much higher deformation around the metatarsals, which increases the energy stored in the system. These highly strained tissues will cause high stress within the metatarsals as shown in the main results.

5.5.2 Forefoot landing at different touchdown angles

To further explore the high injury risk on the metatarsals during forefoot landing, we studied the stress on metatarsals during different touchdown angles i.e. 5°, 10° and 15°. Figure 5.14 shows the different touchdown angles of forefoot landing at sagittal planes. Ground Reaction Forces at 0.5, 1 and 2 times of bodyweight were selected to present the change of stress on metatarsals during landing process. When touchdown changed from 5 to 10 degrees, no significant stress increasing was found on the metatarsals and the distribution of stress was consistent, in which the stress level increases from 1st metatarsal to 4th metatarsal continuously while the 5th metatarsal has lower stress than the stress in the 4th's. The metatarsals on the lateral side is around twice that of the medial side at 5 and 10 degrees touchdown angle. However, when the touchdown angle increases to 15 degrees, the stress on the lateral side goes up dramatically especially if reaction force is

beyond 1 bodyweight which is 131% and 92% higher compared to the same stage at 5° and 10° touchdown angle respectively.

Figure 5.14 The average stress of metatarsal during forefoot strike at different landing angle i.e. 5°,10° and 15°.

More specifically, Figure 5.15. shows stress on each metatarsal during different forefoot touchdown angles at 0.5BW, 1BW and 2BW. Stress level is comparatively safe when the loading is within 1BW at touchdown angle of 5° and 10°. Except for a small area at the medial side of mid side of 5th metatarsal the stresses of all the other parts of metatarsals stress are below 10MPa which is unlikely to fracture. When loading reaches 2BW, the lateral side of metatarsals both have stress concentrations at 5 and 10 touchdown angles and the high stress areas are consist. These high stress areas in red are susceptible to micro facture. Besides, the first metatarsal would bear more stress and more even stress distribution would be seen when the touchdown angle is 10° compared to 5° in which the stress on 1st metatarsal is obviously smaller than the other 4 metatarsals at 1BW, in shown at Figure 5.15. This indicates that the 1st metatarsal has not fully utilised its structural function due to its wide anatomic shape. While touchdown is at 15 degrees, the stress spread relatively evenly on the metatarsals at 0.5 BW. When the load reaches 2BW, stress on the 2nd, 3rd. 4th and 5th metatarsals are all above 10 MPa, and the peak value reaches 136.92MPa.
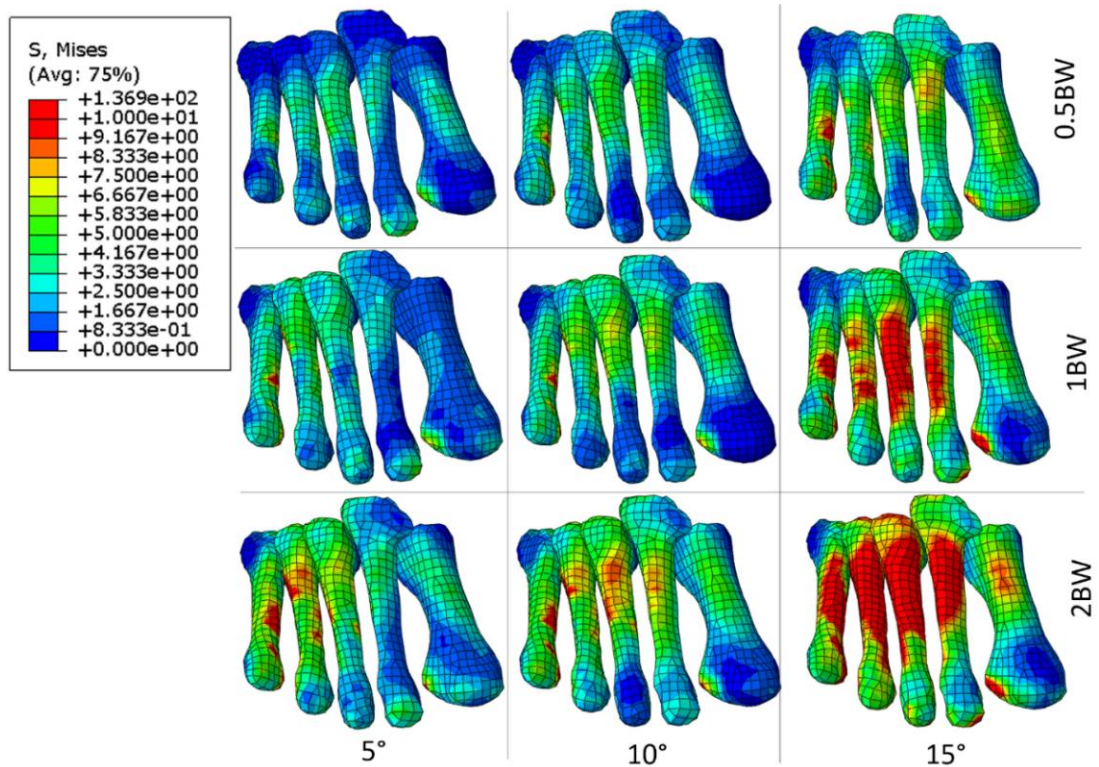
Figure 5.15 The stress distribution on each metatarsal during forefoot strike at different angles.

The high metatarsal stress at high forefoot touchdown angle also showed high internal energy stored among different forefoot landing angles as shown in Figure 5.16. Higher angle between metatarsal and ground in landing would increase the strain energy due to the deformation of the metatarsals along a longitudinal direction and high shear stress would be seen on the cross sectional area. These will also cause much higher deformation around the metatarsals, which increases the energy stored in the system.
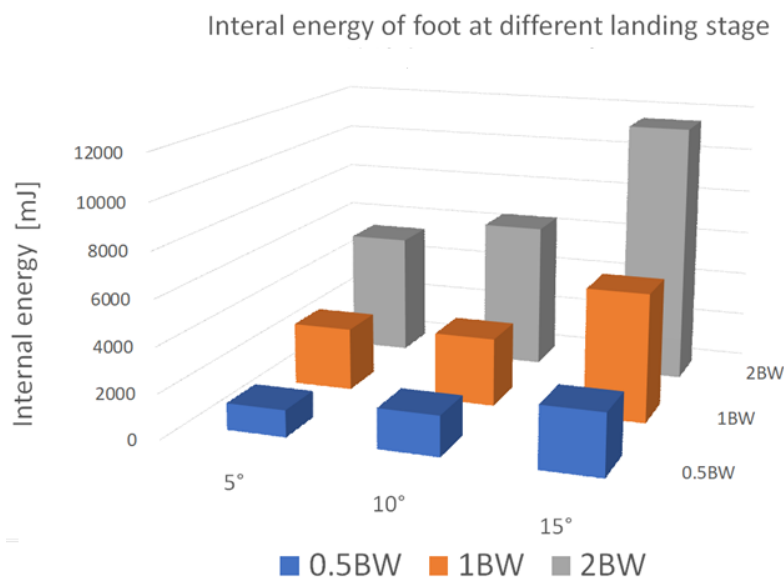
Figure 5.16 The internal energy of foot during different stages of forefoot strike at different touchdown angles.

Forefoot landing puts metatarsals at the first place of impact, in which the metatarsal bones would bear more load compared to the stress in a rearfoot strike or mid foot landing style. This has been proved to be the case by insole pressure loading measurement (Kernozek et al 2014). In addition, it was also reported that the GRF and plantar pressure under the metatarsals were greater in the forefoot and phalanx during non-rear foot strike (Kernozek et al 2014). Forefoot landing pattern may also increase the potential of metatarsal injury such as fracture. Recent case studies revealed that the use of minimalist footwear, which encourages rearfoot strike, caused higher occurrence of metatarsal stress fractures (Giuliani et al 2011).

5.6 Use of the modelling to assess the effect of shoe sole design and structures including auxetic material and embedded system

As for the application in sports, shoe soles are actually a material system with different layers (insole, midsole, and outsole). One main benefit of FE modelling in lies its ability to effectively assess potential effects of material properties and structure on the deformation and pressure under the foot. Compared to engineering problem such as indentation, machining, etc (Kong et al 2010), the modelling can be used to accurately quantify the effect of materials. The use of FE modelling also gives an estimation or assessment of the trend of influence from materials. These will provide important information for analysing the potential effects of materials in real complex situations considering both the engineering response and potential influence on the adaptability of the wearers, the latter of which may be sensitive to subtle difference in pressure and the deformation mode. Some typical results are shown in this section including the effects of auxeticity, sole stiffness and thickness and continuous embedded shells or discretely distributed circular shells.

Figures 5.17&18 show the influence of the auextic behaviour of soles on the lateral deformation and the pressure in standing. As shown in Figure 5.17(a), lateral displacement of auxetic and non-auxetic insoles gives a clear difference. As shown in the figure, the auxetic insole showed contraction under the foot at a small scale. This suggest that auxetic behaviour could change the interaction between the foot and the sole. Figure 5.18 showes typical plantar pressure distribution under a standing load, which gives an indication about the location and size of the contact area. The results show that use of an

auxetic material can modify the pressure level more than the normal insole, which can reduce or prevent some kinds of foot pains.
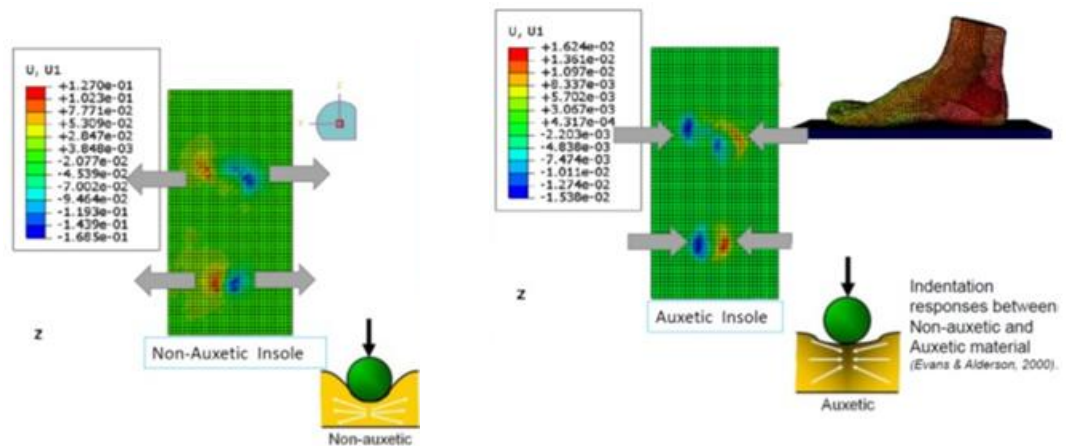
(a) Lateral displacement contour showing expansion of the material under the foot in standing.

(b) Lateral displacement contour showing tendency of contraction the material under the foot in standing.

Figure 5.17 Typical results showing the influence of Auxetic behaviour of shoe soles in standing.
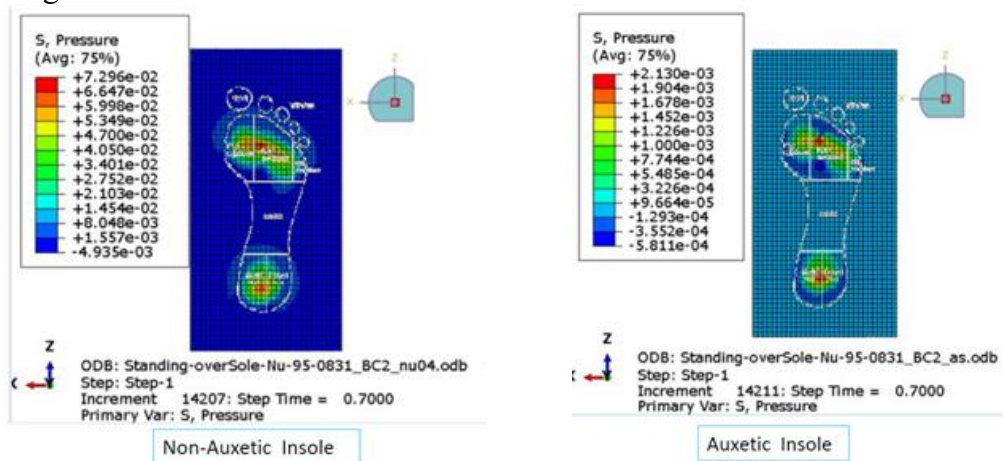
(a) Pressure under the foot over a normal (non-auxetic material).

(b) Pressure under the foot over an auxetic materials.

Figure 5.18 Difference in pressure distribution on the shoe sole material with positive or negative Poisson's ratio.

Figure 5.19 shows the effect of shore hardness/stiffness of shoe sole. The data shows that there is a difference in the value of the lateral displacement and pressure, but the overall pattern is very similar. Figure 5.20 and Figure 5.21 show the effect of thickness of shoe sole on the deformation and the pressure. As shown in Figures 5.20(c&d compared to e&f), the pressure pattern of non-auxetic and auxetic insole shows clear differences when the thickness of the shoe sole is 10mm and 5mm. As shown in Figure 5.21, the contact area on the foot is different. The one with an auxetic shoe sole material is smaller, this is resealable as auxetic material causes contraction and reduced areas. This

is also in agreement with indentation with a rigid indenter, as shown in the previous works in Chapter 4.
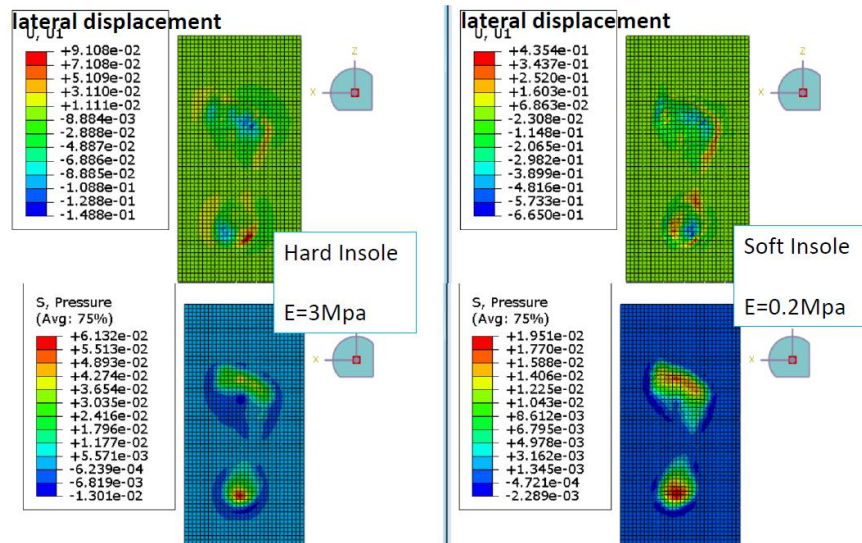
Figure 5.19 Influence of the shoe sole (shore) hardness/stiffness on lateral displacement and pressure.
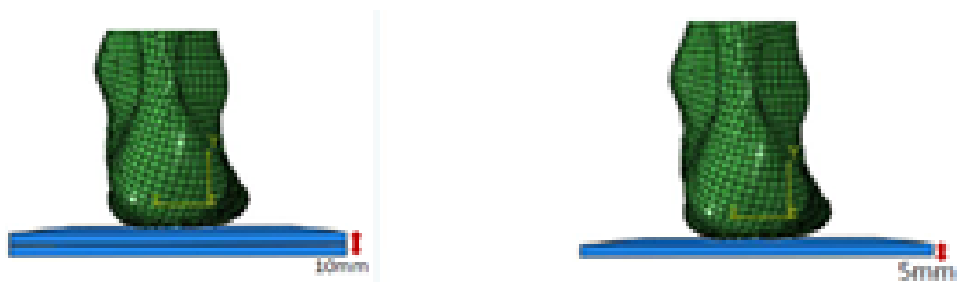
(a) Sole material thickness=10mm   **(b) Sole material thickness=5mm**
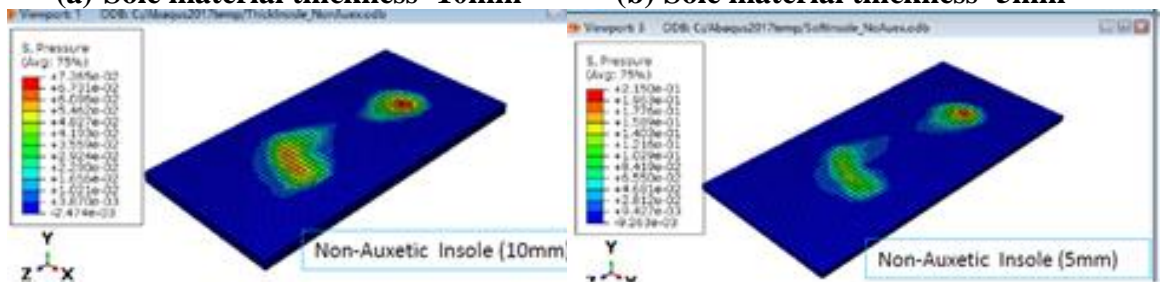
(c) Non-Auxetic material (10mm thick)   **(d) Non-Auxetic material (5mm thick)**
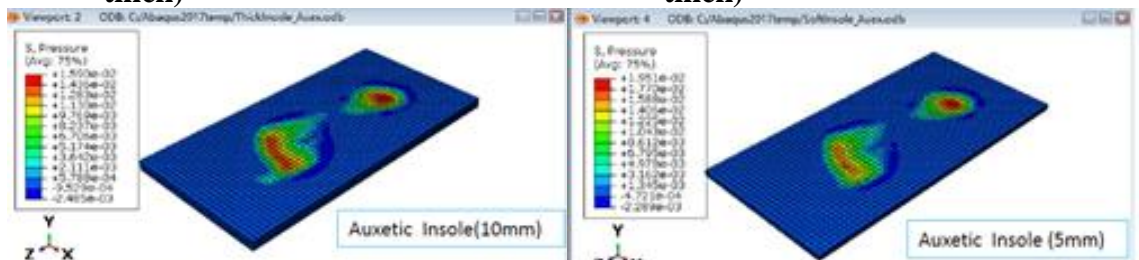
(e) Auxetic material (10mm thick)   **(f) Auxetic material (5mm thick)**

Figure 5.20 Influence of the shoe sole thickness on pressure distribution between non-auxetic and auxetic materials.

Figure 5.21 shows typical results illustrating the effect of embedded shells (thickness =0.1mm, E=30M) in shoe sole material with positive and negative Poisson's ratio. Figure 5.21 (a&b) compared the foot-shoe sole pressure, while Figures 5.21 (c&d) compared the pressure on the embedded shell. As shown in Figures 5.21 (a&b), the insertion of a thin sheet has changed the effect of the auxeticity. When there is no embedded shell, the contact areas become smaller due to the contraction of the matrix. When a shell is embedded, the contact area increased due to the combined effect of the shell and auxeticity of the matrix (Figure a vs. Figure c). This is probably associated with the different responses of the shell as shown in Figure 5.22, as the pressure on the shell is significantly different; this corresponds to the different shell deformation observed in the indentation tests shown in Chapter 4. The absolute value and their influence on the sense of the foot still needs further study, but the result highlights the effect of combination and the embedded shells on the interface, and potentially this could be used to design materials for shoe sole applications.
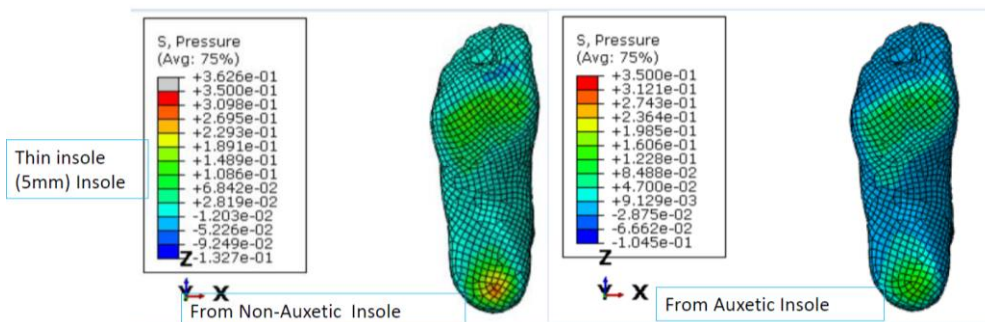
Figure 5.21 Pressure on foot soft tissue due to auxeticity and thickness of the shoe sole.

Embedded Shell PE=100(Mpa), ν=0.3] : Matrix [E=1 (MPa), ν=+0.4]
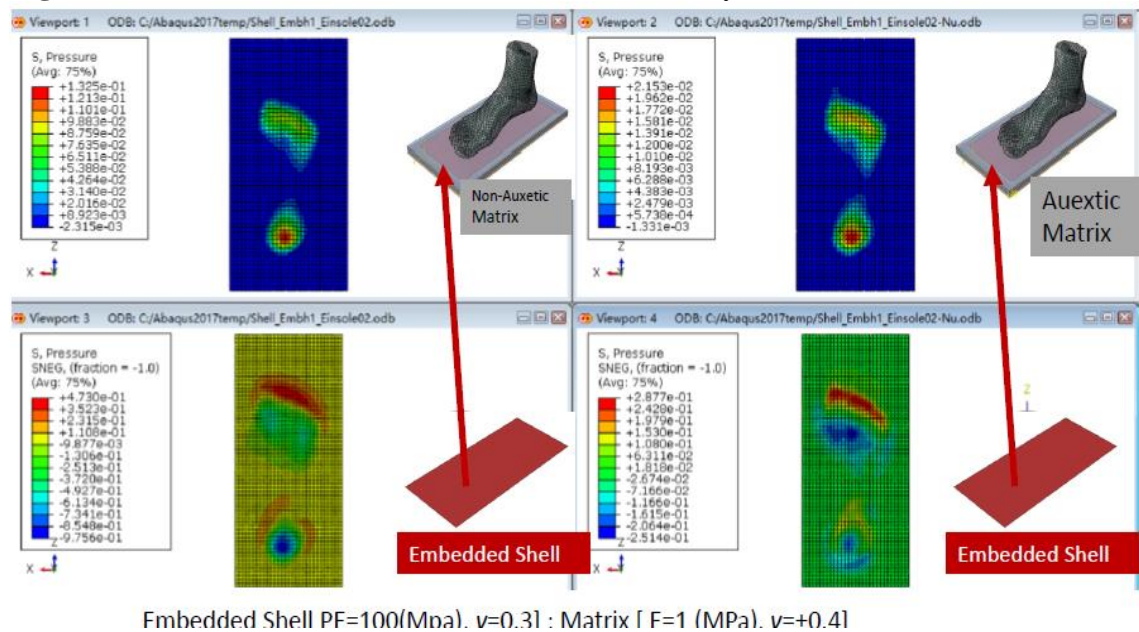
Figure 5.22 Effect of auxeticity on pressure distribution of matrix and embedded shell.

5.7 Discussion, Limitation and Future Work

5.7.1 FE modelling of human foot

As shown in Figures 5.6 and 5.7, the numerical results of the FE model are in a good agreement with the experimental data and published works (Gu et al 2011; Cheung et al, 2005; Cheung and Zhang, 2006). The plantar pressure distribution also showed a good agreement between the FE modelling and biomechanical tests. These are commonly used approaches to check the validity and accuracy of FEMs (Guiotto et al, 2014; Erdemir et al, 2005; Gu et al 2010). These will provide confidence in the prediction of the stresses in the metatarsals in forefoot and rearfoot strike, which is the main focus of the work. The GRF on the reference point of rigid plate is used to represent the ground reaction force during whole phase of strike. The trend of the GRF predicted is found to be comparable to other published works (Lieberman, 2012; 2010). The numerical data predicted for both forefoot and rearfoot strike are close to the GRF tests results on the same subject. The peak GRF observed at the end of landing phase for both forefoot and rearfoot strike reaches a similar level (~2.5BW). This is also in agreement with published data, which reported a maximum force of 2.2-2.5 BW (Lieberman et al, 2010; Squadrone and Gallozzi 2009; Crowell and Davies 2011). This load level is also observed by the human body modelling investigating the response of the human body to the collision with the ground during hopping, trotting, or running (Nikooyan and Zadppor 2012; Clark et al 2017; Nedergaard et al 2017). In the models, the mass, spring, and damper elements are used to represent the masses, stiffness properties, and damping properties of hard and soft tissues. The reaction force is a combination of the influence of the bodyweight, muscle action, and velocity. The reaction force predicted by the mass-spring-damper model is in a similar range to the load used in the FE models of this work.

The efficiency and stability of an FE explicit model can be verified by checking the ratio between the artificial strain energy and internal energy level (ALLAE/ALLIE), which is commonly used in dynamic situations (Auricchio 2010; Egan et al 2014). It is an indicator for the quality of the mesh size, contact, viscous damping and stabilisation, thus reflecting the accuracy of the solution. In the models developed in this work, the ALLAE/ALLIE ratio is always less than 2% during either forefoot landing or rearfoot strike. This suggests that the FE is effective and stable. In the model, the plate is a rigid body, the internal energy is also representative of the energy absorbed during the movement. As shown in Figure 5.13, at 0.5BW load, the strain energy level stored in the

foot is similar between different conditions, and then at 1 BW, the energy for rearfoot strike is slightly higher. While at 2 BW (which is close to the maximum (2.2-2.6 BW) (Liberman 2012), the energy in the foot during rearfoot strike is much higher; this is due to the fact that for rearfoot, the main force is sustained by the bony structure, and the heel pad is the main deformable part. For forefoot strike, the soft tissue has a much higher deformation around the metatarsals, which increases the energy stored in the system. These highly strained tissues will cause high stress within the metatarsals as shown in the main results.

5.7.2 Foot deformation under different conditions

This study comparatively evaluated the stress distribution in the metatarsals between forefoot landing and rearfoot strike. As hypothesized, the stress level and increasing rate of the metatarsals stresses during forefoot landing is higher than that in rearfoot strike especially the stress in the 1st metatarsal during forefoot landing is much higher. The results show that a forefoot strike pattern puts metatarsals at high stress level along with a higher rate of stress increase than that for rearfoot strike. The stress distribution and stress level are in agreement with some published data (Gu et al 2011; Cheung and Rainbow 2014). The case study by Cheung et al. (2014) observed a similar result that metatarsal stress increased during barefoot running, which results in severe running injuries, such as metatarsal and calcaneal stress fractures (Cheung and Rainbow 2014). Giuliani et al (2011) reported that metatarsal fracture occurred on novice barefoot runners, which can be explained by the higher loading rate during impact. The landing pattern transition to a forefoot landing style put the metatarsals as the first impact section of the foot (Giuliani et al, 2011). Comparative study of the landing styles revealed that the 1st metatarsal has a dominate role bearing relatively high stress and greatest stress increasing rate in both forefoot and rearfoot strikes, which is associated with its wider anatomy structure than the other four metatarsals. This is in agreement with the finding of Muehleman et al (2000), who mentioned that the first metatarsal bone as a major weight-bearing structure is of important biomechanical function within the foot (Muehleman et al, 2000). During forefoot strike, a higher stress increase rate was observed in the neutral area of the metatarsals at the 2 BW load point. However, the stress levels at initial contact between each metatarsal during forefoot strike are at a comparable level (around 6MPa). This indicates that the automatic pronation has happened under mechanical downwards

boundary conditions. In contrast, stress increasing is relatively uniform between the five metatarsals during a rearfoot strike.

The model used constraint of 'embedded region' to model the key internal foot components encapsulated by hyperelastic material for the soft tissues. The embedded element technique is used to specify that an element or group of elements is embedded in "host" elements (Abaqus Manual 6.14). This offers an effective way of modelling the foot focused on the stresses in the metatarsals with improved efficiency and resource saving. Comparing this with a full perfect contact model without using the embedded region, the number of elements is much lower. For the full modelling approach, the number of elements for the whole foot is typically around 1,200,000-1,300,000 (Gu et al, 2010; Fontanella, 2014), which is around 4-5 times the element number used in the current explicit model (273,123 elements).

The mechanical responses of the human foot in different landing conditions have been the subject of many research works (Qian et al 2013; Fontanella et al 2015; Qiu et al 2011; Fontanella et al 2014), in which different procedures have been used to suit the technical focus of the studies. Fontanella et al (2015) investigated the mechanical behaviour of the plantar soft tissue during gait cycle using Abaqus implicit modelling. The work considered detailed viscoelastic effects with a specific visco-hyperelastic constitutive model, the mean value of the loading rate during impact is 0.033BW/s, which is close to the loading conditions (0.1s for 2 BW) for this work. In another model by Fontanella et al (2014), the tibia and the fibula were considered to be fully fixed, and the boundary and loading condition is simplified by fixing the relative motion between the foot and the plate. Similarly, in the work on the effects of ankle arthrodesis on biomechanical performance of the entire foot (Cheung and Zhang 2008; Wang et al 2015), the superior surfaces of the tibia, fibula, and encapsulated soft tissue were fixed throughout the simulation. The ground reaction forces were applied through moving the rigid plate beneath the foot. The pressures at the heel region reported in the works are 0.3-0.33MPa, and 0.22-0.26MPa under the metatarsals. These pressure values are similar to the data predicted in this work. Yu et al (2013) conducted biomechanical simulation of high-heeled shoe donning and walking. The work used linear elastic properties for the bone and soft tissues. The average stress in the first metatarsals during the push off phase is around 6.5 MPa at a 1.2 BW, which is similar to the value in this work for forefoot landing. All the works mentioned above used Abaqus implicit, which has limitations in dealing with fast dynamics with small time steps in the landing phase and normally a

much higher number of elements are required. Qian (2013) used an Abaqus explicit solver with a two dimensional model to study the human foot complex in the sagittal plane during level walking. Their analysis showed that a dynamic FE simulation can improve the prediction accuracy of the peak plantar pressures at some parts of the foot complex by 10%–33% compared to a quasi-static FE simulation. However, the proposed model is confined only to the sagittal plane and has a simplified representation of foot structure, in which the plane stress section thickness was set to 60 mm representing the approximate foot width of the subject. The FE modelling in this work used a full 3D model, the results show that an explicit model has the advantage of dealing with complex modelling with a more flexible loading to suit different foot loading situations.

The comparison of the stress level between forefoot and rearfoot strike with a subject specific model will provide important information for understanding the loading of metatarsals in different movements. Different peak stress areas indicate the areas more prone to injury on the metatarsals with high stress and increasing rate. In particular in forefoot strike, a 9.67% higher stress increasing ratio in the metatarsals than that for rearfoot strike indicates a higher chance of stress fracture. This agrees with the observation that the forces and stresses experienced in the metatarsal region are increased when using a non-heel strike pattern during running (Kernozek et al, 2016). The bending strain of metatarsals reported by these authors would potentially be increased even higher in those runners selecting to use a non-heel strike running pattern (Gross and Bunch 1989). This may contribute to a higher incidence of metatarsal stress fractures in runners converting to minimalist footwear (Giuliani et al 2011; Salzler et al 2012).

5.7.3 Limitation of the foot model and future development

The work has shown that the use of foot modelling can provide a useful tool to compare the foot deformation and stresses in the metatarsals during forefoot and rearfoot strike, in particular for bare foot or with minimalist shoes. There are some limitations of the results, which should be noted and some of which is open to future studies. This work has been focused on a situation with a rigid ground, which is the same situation as the experiments and represents the most dangerous/relevant situation for metatarsal damage. The results can be extended to more complex situations such as with soils, turfs, etc. This can be either conducted with a layered soft materials system, or more realistically using

a discrete element model for modelling the soil. The latter will be able to distinguish the effect of soft ground on the stresses in different metatarsals. The tissue for foot modelling is a complex problem. An optimum scheme has to balance representing the realistic structure, the practicality and efficiency of the modelling. A particular area for the human foot modelling which should be noted is the use of regional properties or age/medical related properties (Ledoux, 2007); One previous work used *in vivo* indentation tests to characterise the soft tissue over different foot zones and used detailed properties in foot modelling (Gu et al 2011); such a process with detailed skin behaviours (Fontanella et al 2015) and heel pad properties (Fontanella et al 2014; Natali et al 2011; 2012; Fontanella et al 2012) should be adapted when the plantar pressure is the main focus of the modelling for situations such as diabetes feet. Another area that should be noted is the modelling of the bone. This study has focused on the whole deformation of the foot bony structure in standing, forefoot and rearfoot landing. The bone has been modelled with a uniform property. This is probably sufficient for studying the general stress levels in the metatarsals, further details are required to extend the modelling to more complex loading conditions or more challenging landing situations such as inversion and eversion landing. For detailed modelling of the metatarsals, more detailed works are required, ideally using sub-modelling to extract the boundary condition and force around the metatarsals, in which the individual muscle, even nerve can be considered. This should be addressed in future works.

5.7.4 Potential use of combined structure and biomechanical modelling for footwear development.

The application of auxetic material with negative Poisson's ratio are increasingly be explored, including in sport equipment and footwear. (Liu *et al*, 2009; Bentham *et al*, 2009; Sanami *et al*, 2014; Zhu *et al*, 2015; Aw *et al*, 2015; Narojczyk *et al*, 2016). Figure 5.23(a&b) shows two typical examples in which the auxetic patterns are used on the outsole (Cross et al, 2016). The structure can be developed and simulated through parametric studies. An FE model is shown in Figure 5.23(c), which is developed with Abaqus unit cell approach (Zhu et al 2015). In the model, a periodic boundary is applied. The geometrical patterns have hinged polygons that rotate with respect to each other, as shown in Figure 5.23(c). Through the parametric program, the model can generate automatically with predefined number of units, etc. A typical deformed model is shown in Figure 5.23(c). It clearly shows that the structure expanded when being pulled. With the program, the size of each unit, the number of the unit, can all be automatically changed.

(a) Sample outsole design with auxetic structure (Little, 2017).

(b) Sample outsole design with an Auxetic structure (Toronjo, 2016).
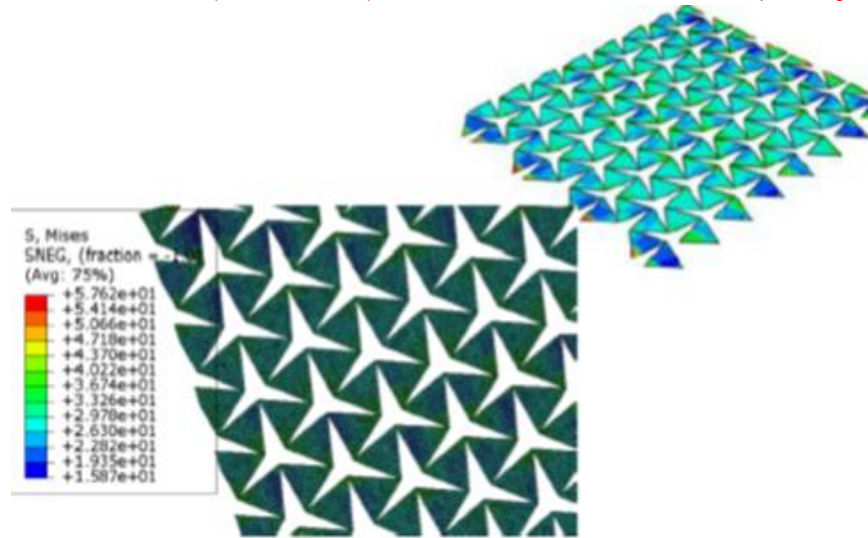
(c) Unit cell FE modelling approach for auxetic structure and deformed shape.

Figure 5.23 FE modelling of auxetic structures.

Foot mechanics under different loading conditions is an active research area, which could provide important information for footwear design, injury presentation and enhancing performances. Use of FE modelling will help continuously incorporating new materials and designs following their development. This work has been focused on setting up a framework on the use of FE modelling to analyse the effect of new material properties (such as embedded structures, auxetic behaviours) under different conditions including localised load (indentation), compression, foot under different loading angles, etc.). As detailed in Chapter 2 and Chapter 5, the foot and sole can be divided into many regions, so to improve the contact on each foot zones. An approach with combined use of different form of reinforcement (such as particles, thin sheet and mesh) in the material may help to give more freedom to the design. Parametric computational modelling is an effective tool to assess the effects of the material structure and product deformation under different conditions. Figure 5.24 illustrates a framework of such an approach combining material structure modelling and foot mechanism (which is also applicable to foot

prosthetics) based on the research developed in this work. As shown in Figure 5.24, the frame work can apply Random 2D inclusion model and embedded sheet or mesh within the shoe. The random inclusion model was developed based on a statistical procedure. The process involves firstly generating of Voronoi distribution point (Barrett et al, 2018), then the inclusions (of any shape) will take up the location of the points (with a python program) with a random orientation; then the system is embedded in a material of rubber or foam. This approach can be applied to many different shapes, including those used in modelling conductive rubber consisting conductive particles. The 2D structures with different Poisson's ratio can be designed and used as the embedded structure. Some temperature dependent properties can also be developed. This will offer much more freedom in design structure for different regions for shoe soles, which will be explored in future works.
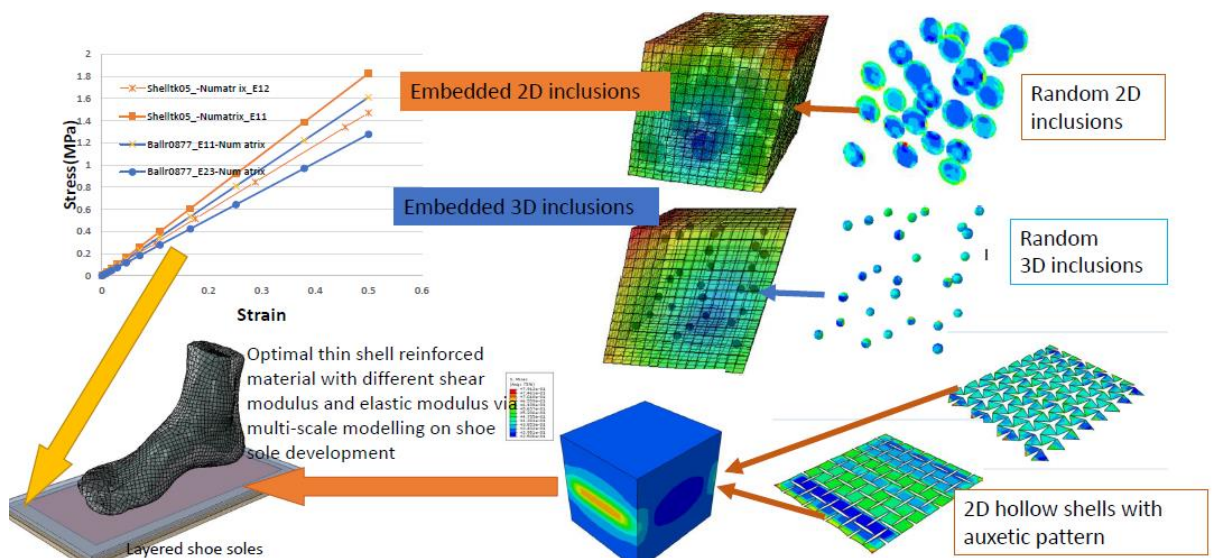
Figure 5.24 A framework of linking material structure design and foot mechanics.

5.7.5 FE modelling of foot prosthetics

Another area of research benefited from the key modelling approach (including building models from images) in this work is in the modelling of foot prosthetics. Figure 5.25 shows different design of foot prosthetics (sketches based on different prosthetics). In prosthetic foot-1, a wooden bock is embedded in silicone rubber. The design is cheap and simple. Prosthetic foot-2 is more a complex design, in which a fish bone type plastic structure is embedded in silicone rubber. Prosthetic foot-3 is a carbon fibre sample, in which thin carbon fibres plate are used to generate a structure with good strength, low weight and good recovery ability.
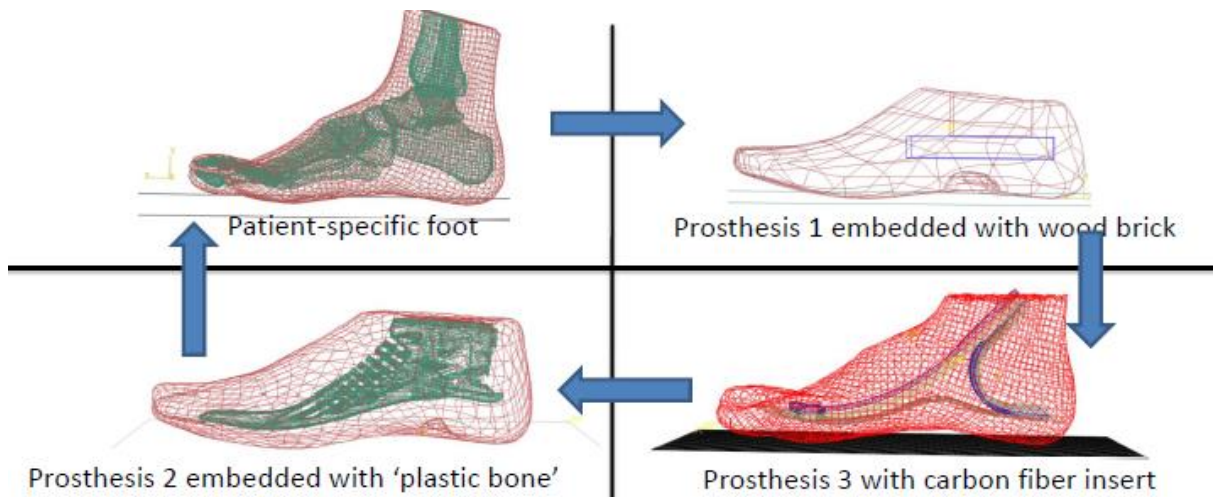
Figure 5.25 Typical designs of foot prosthesis.

Figure 5.26 shows the FE model of the carbon fibre based prosthetics under controlled compression tests. As shown in the Figure, the force displacement data shows a good agreement with the testing data. The FE model is also able to model the response of the prosthetics on different EVA foams of different shore hardness. Foot prosthetics is one of the most active research related foot mechanics with great social and economic benefits. This work has briefly reported the comparison between FE and experimental. A more detailed Python program incorporating composite layered design can be developed in the future to apply different materials layer in different resins. The validated prosthetic model can be combined with the Angle control functions of the Abaqus plugin to provide a quick way of assessing the deformation of foot prosthetics under different conditions.
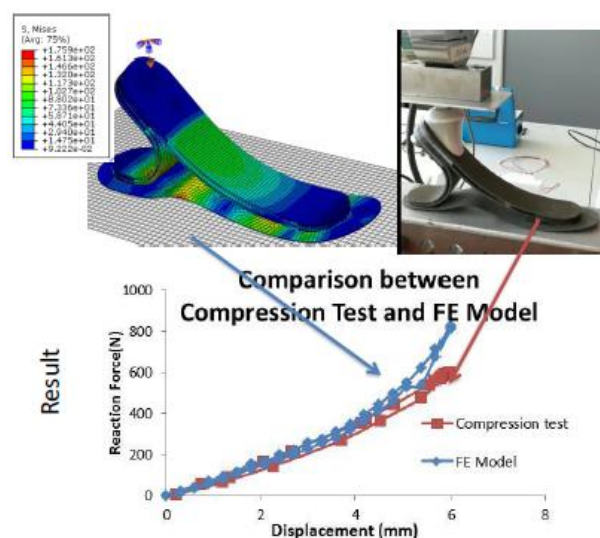
Figure 5.26 Preliminary results on testing and modelling of carbon fibre foot prosthetic.

5.8 Summary

This chapter shows the development of an Abaqus plug-in and its application in the study of foot mechanics and the effect of materials and structure. The plug-in is able to control the position of the foot and the materials properties. A new modelling approach has been evaluated in this work, in which the bone structure is treated as an embedded system within a homogenized foot host region. The model is verified by comparing the numerical data for simple standing against a subject specific navicular drop test. Future work can be used to verify this approach through sensitive tests with a parametric FE model and tests on a larger number of cohorts.

The results for the forefoot strike tests showed an overall higher average stress level in the metatarsals during forefoot landing than that for rearfoot strike. The metatarsal stress increased 30.76% for forefoot strike and 21.39% for rearfoot strike when the load is increased from 0.5 body weight (BW) to 2 BW. The maximum rate of stress increase in the five metatarsals is observed on the first metatarsal in both landing modes. During forefoot landing, the average stress on the first metatarsal is increased by 48.21% from 0.5BW to 2BW. The results indicate that changing strike pattern from rearfoot strike to forefoot may increase the potential of metatarsals injuries due to the high stress level and stress increase rate. Finally, the FE model is used to study the influence of some key materials properties and structures of the shoe sole (including stiffness, thickness, auxetic properties and embedded shell) on the deformation and the foot-sole pressure distribution and contact areas. The work showed that auxetic shoe sole will reduce the contact area due to contraction of the materials; this is similar to the reported behaviour of auxetic materials under indentation. The work showed that an embedded shell can alter the contact area and the pressure distribution in both non-auxetic and auxetic materials, which potentially could provide a means for material structure design for foot-shoe pressure measurement, which will be studied in future works.

The use of auxetic structures and modelling based structure design for footwear were discussed and the framework of such an approach was highlighted. Some typical foot prosthetic structure embedded in silicone rubber and composite structures is also presented and discussed.

CHAPTER SIX CONCLUSIONS

AND FUTURE WORK

7.1 Summary and Conclusions

In this work, parametric FE modelling has been developed and used to study the deformation of soft materials with different embedded systems under indentation and more complex conditions. The deformation of a soft material with an embedded stiffer layer under a cylindrical flat indenter was investigated through FE modelling. A practical approach in modelling embedded systems is evaluated and presented. The FE results are correlated with an analytical solution for homogenous materials and results from a mathematical approach for embedded systems in a half space.

The influence of auxeticity on the indentation stiffness ratio and the deformation of the embedded system under different conditions (indenter size, thickness and embedment depth of the embedded layer) was established and key mechanisms of the Poisson's ratio effect are highlighted. The results show that the auxeticity of the matrix has a direct influence on the indentation stiffness of the system with an embedded layer. The enhancement of indentation resistance due to embedment increases, as the matrix Poisson's ratio is decreased to zero and to negative values. The indentation stiffness could be increased by over 30% with a thin inextensible shell on top of a negative Poisson's ratio matrix. The deformation of the embedded layer is found to be significantly influenced by the auxeticity of the matrix. The modelling approach for cases in which piezoelectrical sensors, force sensitive resistor and auxetic mesh was used as the embedment showed that the modelling approach is effective in predict the mechanical and electrical response of the embedded sensors under different loadings.

A full scale parametric FE foot model is developed to simulate the deformation of the human foot under different conditions including soles with embedded shells and negative Poisson's ratio. The models used a full bone structure and effective embedded structure method to increase the modelling efficiency. A hexahedral dominated meshing scheme was applied on the surface of the foot bones and skin. An explicit solver (Abaqus/Explicit) was used to simulate the transient landing process. Navicular drop tests have been performed and the displacement of the Navicular bone is measured using 3D image analysing system. The experimental results show a good agreement with the numerical models and published data. The detailed deformation of the navicular bone and factors affecting the navicular bone displacement and measurement are discussed. The stress level and rate of stress increase in the metatarsals and the injury risk in the foot

during forefoot strike (FS) and rearfoot (RS) are evaluated and discussed. A detailed subject specific FE foot model is developed and validated. The deformation and internal energy of the foot and stresses in the metatarsals are comparatively investigated. The results for forefoot strike tests showed an overall higher average stress level in the metatarsals during the entire landing cycle than that for rearfoot strike. The increase rate of the metatarsal stress from the 0.5 body weight (BW) to 2 BW load point is 30.76% for forefoot strike and 21.39% for rearfoot strike. The maximum rate of stress increase among the five metatarsals is observed on the 1st metatarsal in both landing modes. The results indicate that high stress level during forefoot landing phase may increase the potential of metatarsal injuries.

The FE was used to evaluate the effect of embedded shell and auxetic materials on the foot-shoe sole interaction influencing both the contact area and the pressure. The work suggests that application of the auxetic matrix with embedded shell can reinforce the indentation resistance without changing the elastic modulus of the material which can optimise the wearing experience as well as providing enough support for wearers. The use of auxetic structures and modelling based structure design for footwear were discussed and the framework of such an approach was highlighted. Some typical foot prosthetic structure embedded in silicone rubber and composite structures is also presented and discussed.

7.2 Recommendations for further works

This work has established a framework for the use of a Python based Abaqus plug-in for the study of the indentation resistance on material with embedded thin layers or finite sized embedment and foot deformation in different loading angles and in contact with different material systems. The work can be extended into the following areas: (1) The effect of indenter shape on the indentation resistance, potentially including plastic deformation and fracture. Indentation is a loading condition which may cause problems for the mechanical integrity and the functional performances. The work can be extended to the other indenter shapes using the Abaqus plug-in including spherical indenter, conical indenter and shore hardness indenters. For sphere indenter, the force-displacement data is a curve, so a program for curve can be used to extract the key curve parameters. For conical indenter, the deformation can easily enter the plastic range (e.g. for the copper bases of the piezo sensors), so this can be modelled by incorporating plastic parameters (yield stress and work hardening) and fracture parameters for both the ceramic and copper base. Currently, preliminary work has shown that the piezo-coating cracks and undergoes debonding under several indentations. The silicone rubber will prevent direct contact of the ceramic with sharp foreign subjects. (2) The Plug-in for the foot model can be used to study the foot deformation in more complex conditions. The methods used to control and partition the sole can be extend to full shoe models of different designs, such as trainers, slippers or high heels. The function of angle can be designed according to the type of shoes and walking/loading conditions. (3) Foot prosthetics is one of the most active research areas with great social and economic benefits. The validated prosthetic model can be combined with the Angle control functions of the Abaqus plug-in to provide a quick way of assessing the deformation of prosthetics under different conditions. This work has briefly reported the comparison between FE and experimental. A more detailed Python program incorporating a composite layered design can be developed to apply different material layers in different resins.

References

Abaqus Theory Manual/User's Manual/Benchmarks Manual., 2014, Version 6.14-1. Hibbitt, Karlsson & Sorensen.Inc.

Almgren R F, 1985, An isotropic three-dimensional structure with Poisson's ratio =−1, *Journal of Elasticity*, 15, .427-430.

Argatov I.I., Guinovart-Díaz R., Sabina F.J., 2012, On local indentation and impact compliance of isotropic auxetic materials from the continuum mechanics viewpoint, *International Journal of Engineering Science,* 54, 42–57.

Atkin, R. J., and Fox, N., 1980. *An Introduction to the Theory of Elasticity*. Prentice Hall Press.

Auricchio F., Conti M., De Beule M., De Santis G., and Verhegghe B., 2011, Carotid artery stenting simulation: from patient-specific images to finite element analysis, *Medical Engineering & Physics*, 33, 281-289.

Aw J., Zhao H., Norbury A., Li L., Rothwell G. and Ren J., 2015, Effects of Poisson's ratio on the deformation of thin membrane structures under indentation, *Physica Status Solid B-Solid State Physics*, 252(7), 1526-1532.

Bamberg, S.J.M., Benbasat, A.Y., Scarborough, D.M., Krebs, D.E. and Paradiso. J., 2008, Gait analysis using a shoe-integrated wireless sensor system. *Information Technology in Biomedicine, IEEE Transactions*, 12(4), 413 – 423.

Barrett T.J., Savage D.J., Ardeljan M., Knezevic M., 2018, An automated procedure for geometry creation and finite element mesh generation: Application to explicit grain structure models and machining distortion, *Computational Materials Science*, 141, 269–281.

Boppana A., Sefcik R., Myers J.G., Lewandowski B., 2015, A flexible method for method for producing F.E.M. analysis of bone using open-source software, NASA Glenn Space Academy Meeting.

Braun, B. J., Veith, N. T., Hell, R., Döbele, S., Roland, M., Rollmann, M., Pohlemann, T., 2015, Validation and reliability testing of a new, fully integrated gait analysis insole. *Journal of Foot and Ankle Research*, 8(1), 1-7.

Briggs P.J., 2005, The structure and function of the foot in relation to injury, *Current Orthopaedics,* 19, 85-93.

Burns, J., Crosbie, J., Hunt, A., Ouvrier, R., 2005, The effect of pes cavus on foot pain and plantar pressure, *Clinical Biomechanics*. 20, 877-882.

Cannata G., M. Maggiali, 2016, An Embedded Tactile and Force Sensor for Robotic Manipulation and Grasping, *Robotics Research: The 16th International Symposium ISRR*, Springer, Berlin.

Cheung J. T. M., Zhang M., 2008, Parametric design of pressure-relieving foot orthosis using statistics-based finite element method, *Medical Engineering & Physics*, 30, 269–277.

Cheung J. T.-M. and Zhang M., 2006, Finite element modelling of the human foot and footwear, *ABAQUS Users' Conference*, 145-159.

Cheung J. T.-M., Zhang M., Leung A. K.-L., and Fan Y.-B., 2005, Three-dimensional finite element analysis of the foot during standing—a material sensitivity study, *Journal of Biomechanics*, 38, 1045-1054.

Cheung R. T. and Rainbow M. J., 2014, Landing pattern and vertical loading rates during

first attempt of barefoot running in habitual shod runners, *Human Movement Science*, 34, 120-127.

Cheung, J. T-M., Wong Y.J., and Zhang, M., 2009, Current methods in computer-aided engineering for footwear design. *Footwear Science*, 1(1), 31-46.

Clark K.P., Ryan L.J., Wey P.G., 2017, A general relationship links gait mechanics and running ground reaction forces, *Journal of Experimental Biology*, 220, 247-258.

Cojocaru, D., and Karlsson, A. M., 2010, On the Effective Elastic Properties of Macroscopically Isotropic Media Containing Randomly Dispersed Spherical Particles, *Journal of Engineering Materials and Technology*, 132(2), 021011-021021.

Crea, S., Donati, M., Rossi S.M.M.D, Oddo C. M., and Vitiello N., 2014, A wireless flexible sensorized insole for gait analysis, *Sensors*, 1, 1073-1093.

Crowell H. P. and I. S. Davis, 2011, Gait retraining to reduce lower extremity loading in runners, *Clinical Biomechanics*, 26, 78-83.

Daoud A.I., Geissler G.J., Wang F., Saretsky J., Daoud Y.A., and Lieberman D.E., 2012, Foot strike and injury rates in endurance runners: a retrospective study, *Medicine & Science in Sports & Exercise*, 44, 325-34.

Divert C., Mornieux G., Baur H., Mayer F., and Belli A., 2005, Mechanical comparison of barefoot and shod running, *International Journal of Sports Medicine*, 26, 593-598.

Edwards W.B., Taylor D., Rudolphi T.J., Gillette J.C., and Derrick T.R., 2010, Effects of running speed on a probabilistic stress fracture model, *Clinical Biomechanics*, 25, 372-377.

Egan B., McCarthy M., Frizzell R., Gray P., and McCarthy C., 2014, Modelling bearing failure in countersunk composite joints under quasi-static loading using 3D explicit finite element analysis, *Composite Structures*, 108, 963-977.

Ekrol I., Court-Brown C.M., 2004, Fractures of the base of the 5th metatarsal. *The Foot*. 14, 96–98.

Erdemir A., Saucerman J.J., Lemmon D., Loppnow B., Turso B., Ulbrecht J.S., 2005, Local plantar pressure relief in therapeutic footwear: design guidelines from finite element models, *Journal of Biomechanics*, 38, 1798-1806.

Eshghi A.T., Lee S., Sadoughi M.K., Hu C., Kim Y.C., Seo J.H., 2017, Design optimization under uncertainty and speed variability for a piezoelectric energy harvester powering a tire pressure monitoring sensor. *Smart Materials and Structures*, 26(10), 105037-105048.

Eskandari M., Shodja H.M., Ahmadi S.F., 2013, Lateral translation of an inextensible circular membrane embedded in a transversely isotropic half-space, *European Journal of Mechanics A/Solids*, 39, 134-143.

Fabrikant V.I., 2011, Application of generalized images method to contact problems for a transversely isotropic elastic layer on a smooth half-space, *Arch. Appl. Mech.* 81/7, 957-974.

Fontanella C.G., Carniel E.L., Forestiero A., Natali A.N., 2014, Investigation of the mechanical behaviour of foot skin, *Skin Research & Technology*, 20, 445-452.

Fontanella C.G., Forestiero A., Carniel E.L., Natali A.N., 2015, Investigation of the mechanical behaviour of the plantar soft tissue during gait cycle: experimental and numerical investigation, *Proceedings of the Institution of Mechanical Engineers, Part H: Journal of Engineering in Medicine*, 229(10), 713-720.

Fontanella C.G., Matteoli S., Carniel E.L., Wilhjel J.E., Virga A., Corvi A., Natali A.N., 2012, Investigation on the load-displacement curves of a human healthy heel pad: in vivo compression data compared to numerical results, *Medical Engineering and Physics,* 34, 1253-1259.

Francesco C., Monaria D., Desloovere K., Aertbeliën E., Schless S., Bruyninckx H., 2016, The reliability and validity of a clinical 3D freehand ultrasound system, *Computer*

Methods and Programs in Biomedicine, 136, 179-187.

Gasper N., X. Ren, Smith C.W., J.N. Grima and K.E. Evans, 2005, *Acta Materialia*, 53(8), 2439-2445.

Giuliani J., Masini B., Alitz C., and Owens L. B. D., 2011, Barefoot-simulating footwear associated with metatarsal stress injury in 2 runners, *Orthopedics*, 34, 320-323.

Grima J. N., Cauchi R., Gatt R. and Attard D., 2013, Honeycomb composites with auxetic out-of-plane characteristics, *Composite Strut.*, 106, 150–159.

Gross T.S. and Bunch R., 1989, A mechanical model of metatarsal stress fracture during distance running, *The American Journal of Sports Medicine*, 17, 669-674.

Gu Y. D., Ren X. J., Li J. S., Lake M. J., Zhang Q. Y., Zeng Y. J., 2010, Computer simulation of stress distribution in the metatarsals at different inversion landing angles using the finite element method, *International Orthopaedics*, 34, 5, 669–676.

Gu Y., Ren X.J., Ruan G., Zeng Y., and Li J., 2011, Foot contact surface effect to the metatarsals loading character during inversion landing, *International Journal for Numerical Methods in Biomedical Engineering*, 27, 476-484.

Gu, Y.D., Ren X.J.,. Li J.S, Lake M.J., Zhang Q.Y., and Zeng Y.J., 2010, Computer simulation of stress distribution in the metatarsals at different inversion landing angles using the finite element method. *International Orthopaedics*, 34(5), 669-676.

Guiotto A., Sawacha Z., Guarneri G., Avogaro A., and Cobelli C., 2014, 3D finite element model of the diabetic neuropathic foot: a gait analysis driven approach, *Journal of Biomechanics*, 47, 3064-3071.

Harmeyer K., Holland M. A., Krutz G., 2007, Embedded Sensors in Rubber and Other Polymer Components, *Experimental Analysis of Nano and Engineering Materials and Structures*, 627-628, Springer Netherlands, Amsterdam.

Henning E.M., and Sanderson D.J., 2010, In-Shoe Pressure Distributions for Cycling with Two Types of Footwear at Different Mechanical Loads. *Journal of Applied Biomechanics,* 11(1), 20-30.

Howell A.M., Kobayashi T., Hayes H.A., Foreman K. B., and Bamberg S.J.M., 2013, Kinetic Gait Analysis Using a Low-Cost Insole, *IEEE transactions on Bio-medical Engineering*, 3284 – 3290.

Jaffe B., Cook W. R. and Jaffe H., Piezoelectric Ceramics, Academic Press, New York, 2012.

Jung, I., Shin, Y.H., Kim, S., Choi, J.Y. and Kang, C.Y., 2017, Flexible piezoelectric polymer-based energy harvesting system for roadway applications, *Applied Energy*, 197, 222-229.

Kalantari M., Khojasteh A., Mohammadnezhad H., Rahimian M. and Pak R.Y.S., 2015, An inextensible membrane at the interface of a transversely isotropic bi-material full-space, *International Journal of Engineering Science*, 91, 34–48.

Kernozek T. W., Vannatta C. N., Gheidi N., Kraus S., and Aminaka N., 2016, Plantar loading changes with alterations in foot strike patterns during a single session in habitual rear foot strike female runners, *Physical Therapy in Sport*, 18, 32-37.

Kernozek T., Meardon S., and Vannatta C., 2014, In-shoe loading in rearfoot and non-rearfoot strikers during running using minimalist footwear, *International Journal of Sports Medicine*, 35, 1112-1117.

Kim, S.H., Cho J.R., Choi J. H., Ryu S.H., and Jeong W.B., 2012, Coupled foot-shoe-ground interaction model to assess landing impact transfer characteristics to ground condition. *Interaction and Multiscale Mechanics* 5(1), 75-90.

Kitaoka H.B., Luo Z.P., An K.N., 1997, Effect of plantar fasciotomy on stability of arch of foot, *Clinical Orthopaedics*, 344, 307–312.

Kong X, Yang Q, Li B, Rothwell G, English R, Ren XJ. 2008, Numerical study of strengths of spot-welded joints of steel, *Materials and Design*, 29, 554-1561.

Kong, K. and Tomizuka, M., 2009, A gait monitoring system based on air pressure sensors embedded in a shoe, *IEEE/ASME Transactions on Mechatronics*, 14(3), 358-370.;

Lakes, R.S., 1987, Foam Structures with a Negative Poisson's Ratio, *Science*, 235, 1038-1040.

Ledoux W.R., Blevins J.J., 2007, The compressive material properties of the plantar soft tissue, *Journal of Biomechanics*, 40, 2975-2981.

Li B, 2009, Development of an inverse FE modelling method for material parameters identification based on indentation tests, PhD Thesis, Liverpool John Moores University.

Li, B., Ren, X. J., Gu, Y. D., English, R., and Rothwell, G., 2009. Characterisation of nonlinear material parameters of foams based on indentation tests, *Material and Design*, **30**, 2708-2714.

Lieberman D. E., 2012, What we can learn about running from barefoot running: an evolutionary medical perspective, *Exercise and Sport Sciences Reviews*, 40, 63-72.

Lieberman D. E., Venkadesan M., Werbel W. A., Daoud A. I., D'Andrea S., Davis I. S., 2010, Foot strike patterns and collision forces in habitually barefoot versus shod runners, *Nature*, 463, 531-535.

Little, C.G., Nike Inc, 2017. Shoe outsole. *U.S. Patent Application* 29/545,969.

Logan A.J., Dabke H., Finlay D., Makwana N., 2007, Fifth metatarsal base fractures: A simple classification', *The Journal of Foot and Ankle Surgery*, 13, 30-34.

Mei Q., Feng N., Ren X.J., Lake M., Gu Y., 2015, Foot loading patterns with different unstable soles structures, *J. Mech. Med. Biol.,* 15, 1550014-1550028.

Monari D., Cenni F., Aertbeliën E., Desloovere K., 2014, Py3DFreeHandUS: a library for voxel-array reconstruction using Ultrasonography and attitude sensors, *Proc. of the 7th Eur. Conf. on Python in Science*, 43.

Moore J.K., 2015, GaitAnalysisToolKit Documentation, Release 0.2.0dev

Morley, R. E., Richter E. J., Klaesner J.W., Maluf K. S., and Mueller M. J., 2001, In-shoe multisensory data acquisition system, *IEEE Trans. Biomed. Eng,* 48(7), 815–820.

Moul J. L., 1998, Differences in selected predictors of anterior cruciate ligament tears between male and female NCAA Division I collegiate basketball players, *Journal of Athletic Training*, 33,118.

Muehleman C., Lidtke R ., Berzins A., Becker J., Shott S., and Sumner D., 2000, Contributions of bone density and geometry to the strength of the human second metatarsal, *Bone*, 27, 709-714.

Mueller M. J., Host J. V., Norton B. J., 1993, Navicular drop as a composite measure of excessive pronation, *Journal of the American Podiatric Medical Association*, 83(4), 198-202.

Natali A.N., Fontanella C.G., Carniel E.L., 2012, Constitutive formulation and numerical analysis of the heel pad region, *Computer Methods in Biomechanics and Biomedical Engineering*, 15, 401-409.

Natali A.N., Fontanella C.G., Carniel E.L, Young J.M., 2011, Biomechanical behaviour of heel pad tissue: Experimental testing, constitutive formulation, and numerical modelling. *Proceedings of the Institution of Mechanical Engineers, Part H: Journal of Engineering in Medicine,* 225, 449-459.

Nedergaard N., Robinson M., Drust B., Lisboa P., Vanrenterghem J., 2017, Predicting ground reaction forces from trunk kinematics: A mass-spring-damper model approach, *International Society of Biomechanics Conference Proceedings*, 1 (1), 432-435.

Nesládek M., Španiel M., 2017, An Abaqus plugin for fatigue predictions, *Advances in Engineering Software*, 103 (2017) 1–11)

Nikooyan A., Zadpoor A., 2012, Effects of Muscle Fatigue on the Ground Reaction Force and Soft-Tissue Vibrations During Running: A Model Study, *Published in: IEEE Transactions on Biomedical Engineering*, 59 (3), 1-12.

Nilsson, J.O., Skog, I., Händel, P. and Hari, K.V.S., 2012, Foot-mounted INS for everybody-an open-source embedded implementation, *IEEE Conference "In Position Location and Navigation Symposium (PLANS)*, 140-145.

Norbury A, 2016, Development of Parametric models for modelling spot welding process, PhD Thesis, Liverpool John Moores University.

Ogden, R.W., 1972, Large deformation isotropic elasticity-on the correlation of theory and experiment for incompressible rubber-like solids. *Proceedings of the Royal Society of London. A. Mathematical and Physical Sciences*, 326, 565-584.

Ou-Yang, D and Yoon P., 2015, Tendinopathies around the foot and ankle. *Sports Injuries: Prevention, Diagnosis, Treatment and Rehabilitation*, 1805-1818.

Pappas, I. P., Keller T., and Mangold S., *2002*, A reliable, gyroscope based gait phase detection sensor embedded in a shoe insole, *IEEE Int. Conf. Sens., Orlando, FL.*

Pataky T. C. 2011, One-Dimensional Statistical Parametric Mapping in Python, *Computer Methods in Biomechanics and Biomedical Engineering*, 1-17.

Photiou D., Prastiti N., Sarris E., Constantinides G., 2016, On the conical indentation response of elastic auxetic materials: Effects of Poisson's ratio, contact friction and cone angle, *International Journal of Solids and Structures*, 81, 33–42.

Qian, Z., Ren, L., Ding, Y., Hutchinson, J.R. and Ren, L., 2013. A dynamic finite element analysis of human foot complex in the sagittal plane during level walking. *PloS one*, *8*(11), p.e79424.

Qiu T.X., Teo E.C., Yan Y.B., Lei W., 2011, Finite element modelling of a 3D coupled foot–boot model, *Medical Engineering & Physics*, 33(10), 1228-1233.

Queen, R.M.; Haynes, B.B.; Hardaker, W.M.; Garrett, W.E., 2007, Forefoot loading during 3 athletic tasks, *Am. J. Sports Med.*, 35, 630–636.

Rahman M., Newaz G., 1997, Elastostatic surface displacements of a half-space reinforced by a thin film due to an axial ring load, Int. J. Eng. Sci. 35, 603-611.

Rohen J., Yokochi C., 1988, *Color Atlas of Anatomy—A Photographic Study of the Human Body, (*Second ed.) Igaku-Shoin, New York, NY.

Salzler M. J., Bluman E. M., Noonan S., Chiodo C. P., and de Asla R. J., 2012, Injuries observed in minimalist runners," Foot & Ankle International, 33, 262-266.

Sanamia M., Raviralaa N., Aldersona K. and Alderson A., 2014, Auxetic materials for sports applications, *Procedia Engineering*, 453 – 458.

Saxena K. K., Das R. and Calius E.P., 2016, Three Decades of Auxetics Research Materials with Negative Poisson's Ratio: A Review, *Adv. Eng. Mater.*, 18, 1847-1870.

Kolken H.M.A. and Zadpoor A.A., 2017, Auxetic mechanical metamaterials, *Royal Society of Chemistry (RSC) Advances*, 7, 5111-5129.

Scott G., Menz H. and Newcombe L., 2007, Age-related differences in foot structure and function, *Gait & Posture*, 26, 68–75.

Selvadurai, A.P.S., 2009, Boussinesq indentation of an isotropic elastic halfspace reinforced with an inextensible membrane. *International Journal of Engineering Science*, 47(11), 1339-1345.

Shariatmadari, M.R., English, R. and Rothwell, G., 2010, Finite Element Study into the effect of footwear temperature on the Forces transmitted to the foot during quasi-static compression loading. *IOP Conference Series: Materials Science and Engineering*, 10(1), 1-8.

Shih Y., Lin K.L., and Shiang T.Y., 2013, Is the foot striking pattern more important than barefoot or shod conditions in running?, *Gait & Posture*, 38, 490-494.

Shit S.C. and Shah P., 2013, A Review on Silicone Rubber, *National Academy Science Letters* 36/4, 355–365.

Shodja H.M., S.F. Ahmadi, M. Eskandari, 2014, Boussinesq indentation of a transversely isotropic half-space reinforced by a buried inextensible membrane, *Applied Mathematical*

Modelling, 38. 2163–2172.

Shorten M.R., 2000, Running shoe design: protection and performance. In Marathon Medicine, *Royal Society of Medicine*, London, 159–169.

Sissler, L, Jacques, A., Rao, G., Berton, E., and Gueguen, N., 2013, A 3-D finite element model of the foot-shoe structure during a walking cycle for shoe sole design. *Footwear Science*, 5(sup1), S36-S37.

Smith K.E., Commean P.K., Mueller M.J., Robertson D.D., Pilgram T., Johnson J., 2000, 'Assessment of the diabetic foot using spiral computed tomography imaging and plantar pressure measurements: a technical report'. *Journal of Rehabilitation Research and Development*, 37(1), 31-40.

Squadrone R. and C. Gallozzi, 2009, Biomechanical and physiological comparison of barefoot and two shod conditions in experienced barefoot runners, *Journal of Sports Medicine and Physical Fitness*, 49, 6-15.

Swift, H., 1952. Plastic instability under plane stress. *Journal of the Mechanics and Physics of Solids*, **1(1)**, 1-18.

Toronjo, A., Under Armour Inc, 2016. *Elastic textile*. U.S. Patent Application 29/480,722.

Verdejo R. and Mills N.J., 2004, Simulating the effects of long distance running on shoe midsole foam, *Polymer Test*, 23(4), 567-574.

Wang Y., Zeng L., Wong D.W., Zhang M., 2015, Effects of ankle arthrodesis on biomechanical performance of the entire foot, *Plos ONE*, 10(7), 1-22.

Winkler A. and Goetz F., 2005, Automated Modelling of Spur Gears and Worm Gears using ABAQUS/CAE), *ABAQUS Users' Conference*.

Winter D.A., 1979, *Biomechanics of Human Movement.* New York: Wiley.

Wojciechowski K W, 1987, Constant thermodynamic tension Monte Carlo studies of elastic properties of a two-dimensional system of hard cyclic hexamers, *Molecular Physics*, 61 1247-1258.

Jopek H. and Strek T., 2016, Thermal and structural dependence of auxetic properties of composite materials, Physica Status Solidi B (b), 252(7), 1551-1558.

Milton   G.W., 1992, Composite materials with Poisson's ratios close to — 1, *Journal of the Mechanics and Physics of Solids*, 40, 1105-1137.

Wong D. W.-C., Wang Y., Zhang M., and Leung A. K.-L., 2015, Functional restoration and risk of non-union of the first metatarsocuneiform arthrodesis for hallux valgus: a finite element approach, *Journal of Biomechanics*, 48,3142-3148.

Wright I.C., Neptunea R.R., van den Bogertb A.J., Nigg B.M., 2000, The influence of foot positioning on ankle sprains, *Journal of Biomechanics*, 33, 513-519.

Yu, J, Cheung J. T.-M., Fan, Y., Zhang, Y. Leung, A. K-L., and Zhang. M., 2008, Development of a finite element model of female foot for high-heeled shoe design. *Clinical Biomechanics*, 23, S31-S38.

Zhao H.Y., 2015, Experimental and Numerical Modelling of Gasket Materials and Property Correlation, PhD Thesis, Liverpool John Moores University.